Diplomarbeit in Physik

Tight-Binding Treatment of Complex Magnetic Structures in Low-Dimensional Systems

von

Timo Schena

vorgelegt der

Fakultät für Mathematik, Informatik und Naturwissenschaften
der Rheinisch-Westfälischen Technischen Hochschule Aachen

im
Dezember 2010

angefertigt am

Institut für Festkörperforschung (IFF)
Forschungszentrum Jülich

Contents

1 Introduction

Since magnetic storage devices have become indispensable nowadays, the search for suitable systems is a thriving field of research both experimentally and theoretically. In the field of spintronics, which has enjoyed a great success story so far, especially the discovery of the giant magnetoresistance-effect (GMR-effect) by P. Grünberg and A. Fert [1, 2], awarded the Nobel Prize in physics in the year 2007, led to a significant increase of the storage density in hard disks and marked a technological breakthrough. Currently, there are promising attempts to construct non-volatile random access memory based on various magnetic phenomena such as for example the tunnelling magnetoresistance or the GMR-effect.

In the magnetic storage devices of this type the physics of low-dimensional systems plays a crucial role. In general, low-dimensional systems reveal a wide spectrum of interesting magnetic properties. Gaining a better understanding of these magnetic properties on a microscopic level helps finding appropriate materials for magnetic storage devices and paves the way to multiple applications in the future generation of spintronic devices. Low-dimensional magnets display a vast phase space of magnetic solutions and magnetic ground states. Besides the well-known ferromagnetic and antiferromagnetic collinear spin configurations, many of the representatives of this class reveal a so-called non-collinear spin-arrangement, such as spin-spirals and skyrmions. While for many of the observed non-collinear spin states the Heisenberg exchange interactions play a crucial role, there is another channel for their occurrence, which is gaining more and more importance in the field of nano-magnetism. It can be attributed to the spin-orbit coupling (SOC), amplified at surfaces and in low-coordinated magnets, which has to be added on top of the Heisenberg exchange, leading to the necessity of a more complex treatment when the spin-orbit-driven non-collinear spin structure has to be considered.

Although the energy scale of the spin-orbit interaction is rather small compared to other types of interactions, such as exchange, its property of breaking the symmetries in the system makes SOC very important. One of the most profound effects due to SOC is the magneto-crystalline anisotropy energy (MCA), which is the energy required to change the magnetization direction in the crystal. The MCA plays an essential role for storing data on magnetic storage devices, and therefore normally such devices are made of materials with large MCA values to guarantee a stable magnetization. An important class of complex magnetic structures like homochiral spin-spirals or skyrmions can only be explained considering another important effect of SOC − the Dzyaloshinskii-Moriya interaction (DMI). Introduced by I. E. Dzyaloshinskii and T. Moriya in the framework of weak ferromagnetic systems [3, 4], the DMI is essential in non-inversion-symmetric systems such as surfaces and layered systems. The model Hamiltonian describing the

DMI in the framework of the extended Heisenberg model [5] is of the following form:

$$\mathcal{H}_{\mathrm{DM}} = -\sum_{ij} \boldsymbol{D}_{ij} \cdot (\boldsymbol{S}_i \times \boldsymbol{S}_j)\,, \tag{1.1}$$

where $\boldsymbol{D}_{ij}$ is the Dzyaloshinskii-Moriya vector and $\boldsymbol{S}_i$ and $\boldsymbol{S}_j$ are the spin moments at the lattice positions i and j. While $\mathcal{H}_{\mathrm{DM}}$ favours canted spin structures like spin spirals, the MCA favours a collinear alignment of the spins. The resulting spin structure results from a subtle competition between MCA, DMI and Heisenberg exchange. Under certain conditions, such as symmetry breaking and enhanced spin-orbit interaction, the role of the DMI in this competition becomes prominent which results in a formation of a spin-spiral with a unique sense of rotation. Recently such DMI-driven non-collinear magnetic structures have been observed experimentally and predicted theoretically in e.g. a double-layer Fe on W(110) [6, 7, 8, 9], Mn/W(110) [10, 11] and Cr/W(110) [12].

The above-listed examples show that it is essential to perform extensive calculations in order to gain a deeper understanding of the complex physics of magnetism in these systems. Additionally, the predictive power of such calculations should not be underestimated, since in principle they could lead to discoveries of novel materials with desired properties which could be utilized for future spintronics applications. Nowadays, a large number of such calculations is performed within the *ab-initio* approach utilizing the density functional theory [13, 14], which proved to be very successful for the description of electronic structure properties of various materials. However, these calculations are normally expensive computationally and require large amounts of computing time in order to achieve the accuracy needed for appropriate description of magnetic properties in these complex systems. In addition, the results of the first-principles calculations are normally not so easy to interpret. Moreover, owing to the complexity and computational challenges, systematic studies of the nature of the DMI, its sign and behaviour in different layered systems, for which the effect of this interaction is particularly strong, are still missing from *ab-initio*. Thus, it would be desirable to have a simple model, which contains the essential physics necessary for a description of complex magnetic structures, powerful enough to enable the possibility for a diverse analysis of the results in terms of various parameters of considered systems, such as spin-orbit coupling strength, spin polarization, electron occupation, degree of hybridization between the electronic orbitals, various symmetries etc.

The parametrized tight-binding method, implemented, tested and described in this thesis, is designed for this purpose. The material-specific parameters entering this method provide an easy way to tune the aforementioned essential quantities. This method allows to perform a lot of comparatively fast calculations in combination with a freedom to vary important properties of the magnetic system and is, therefore, well-suited for performing "numerical experiments". The tight-binding parameters enter into the following simple model tight-binding Hamiltonian consisting of four parts:

$$\mathcal{H} = \mathcal{H}_0 + \mathcal{H}_{\mathrm{mag}} + \mathcal{H}_{\mathrm{LCN}} + \mathcal{H}_{\mathrm{SOC}}\,. \tag{1.2}$$

$\mathcal{H}_0$ contains the on-site energies and the hopping elements, with parametrization based on the Naval-Research-Laboratory tight-binding method (NRL-TB method) [15, 16, 17,

18], which ensures parameter sets of a high degree of transferability. This means that a parameter set suited to a particular structure can be used also for a qualitatively satisfactory description of a different structure. For the description of magnetism a Stoner model [19, 20] is incorporated via $\mathcal{H}_{\mathrm{mag}}$, which can be straightforwardly modified for non-collinear magnetic systems. Tuning the Stoner parameters allows to change magnetic moments and the spin-polarization. The implementation of the Stoner model allows for a self-consistent calculation of the magnetic moments and charges. In this self-consistent cycle $\mathcal{H}_{\mathrm{LCN}}$ assures local charge neutrality. The implementation of the generalized Bloch theorem [21, 22, 23] ensures that spin spiral calculations for each spin-spiral vector $\boldsymbol{q}$ can be performed using a small "collinear" unit cell. Even when the effect of SOC is considered via the Hamiltonian $\mathcal{H}_{\mathrm{SOC}}$, the advantage of the generalized Bloch theorem can be utilized by treating SOC in 1st-order perturbation theory [24, 9]. This tight-binding model has been successfully used for calculations of magnetic properties in Fe-systems [25, 26] and Pt-systems [27], which motivated us to apply the tight-binding method for extensive investigations of the non-collinear magnetism and effects of SOC in systems consisiting of Fe and Pt atoms of varying dimensionality.

The thesis starts with a detailed description of the theory behind the tight-binding method in chapter 2. Each part of the Hamiltonian 1.2 is explained in detail (see sections 2.2-2.7). The implementation of non-collinear magnetism is discussed in section 2.8. In particular we focus on the treatment of spin spirals via the generalized Bloch theorem and the treatment of SOC within 1st-order perturbation theory. In addition, we discuss the implementation of the magnetic force theorem (see section 2.9), the extended Heisenberg model, micromagnetic model and its relevant parameters (see section 2.10). In chapter 3 the magnetism in pure Fe systems like bcc-Fe, free-standing Fe monolayers and free-standing Fe chains is examined and the results of the calculations are compared to *ab-initio* results. We start by evaluating the quality of the tight-binding parametrization for bcc Fe (see sections 3.2, 3.3), and proceed with calculating the MCA of Fe monolayers of different crystallographic orientations and the MCA of Fe monoatomic chains in section 3.4. In addition, the magnon dispersions of bcc-Fe and Fe chains are calculated and compared to *ab-initio* results. In chapter 4 the necessary Stoner parameters for Pt are determined with the help of *ab-initio* calculations. Finally, we investigate the magnetism in composite Fe/Pt systems in chapter 5. In section 5.2 the MCA of the $L1_0$-FePt structure is calculated as a function of the c/a-ratio. Particular attention is paid to test the validity of calculating the DMI in the framework of the 1st-order perturbation theoretical treatment of SOC (see section 5.3.1). At the end, we present a study of the DMI in Fe/Pt layered systems as a function of different Stoner parameters, number of Pt layers and band filling (see section 5.3.2).

2 Theory

2.1 Motivation

The Holy Grail of condensed matter physics is the solution of the eigenvalue problem of the following Hamiltonian:

$$\mathcal{H} = T_e + T_c + V_{e-c} + V_{e-e} + V_{c-c}\,, \tag{2.1}$$

with $T_e = -\sum_i \frac{1}{2}\nabla_i^2$ the kinetic energy of the electrons, $T_c = -\sum_\alpha \frac{1}{2M_\alpha}\nabla_\alpha^2$ the kinetic energy of the nuclei, $V_{e-c} = -\sum_\alpha \sum_i \frac{Z_\alpha}{|\boldsymbol{r_i}-\boldsymbol{R_\alpha}|}$ the Coulomb interaction between the electrons and the nuclei, $V_{e-e} = \frac{1}{2}\sum_i \sum_{j\neq i} \frac{1}{|\boldsymbol{r_i}-\boldsymbol{r_j}|}$ the Coulomb interaction between the electrons and $V_{c-c} = \frac{1}{2}\sum_\alpha \sum_{\beta\neq\alpha} \frac{Z_\alpha \cdot Z_\beta}{|\boldsymbol{R_\alpha}-\boldsymbol{R_\beta}|}$ the Coulomb interaction between the nuclei.

It is impossible to solve this problem for many-electron systems without appropriate approximations. First, it is common to use the Born-Oppenheimer approximation, if the electron-phonon coupling does not critically affect the electronic structure. Then the electronic problem is described by the Hamiltonian

$$\mathcal{H}_e = T_e + V_{e-c} + V_{e-e} + V_{c-c}\,, \tag{2.2}$$

where the positions $\boldsymbol{R_\alpha}$ of the nuclei enter only as parameters, which are usually chosen at the equilibrium positions of the lattice. But also this problem is too difficult to solve without approximations due to the electron-electron interaction. Fortunately, there are plenty of more or less successful ways to reduce the N-particle problem to an effective one-(quasi)-particle problem. One of the most prominent ones is the density functional theory (DFT) of Hohenberg, Kohn and Sham [13, 14], which is implemented in the majority of *ab-initio* electronic structure methods. One problem of this highly accurate method is the required computational time, which remains a challenge even on state-of-the-art supercomputers.

To reduce this computational time one can use a parametrized tight-binding method, with the parameters obtained by *ab-initio* calculations. The tight-binding method described and implemented in this thesis is able to reproduce the qualitative behaviour of physical systems, including their magnetic properties.

A convenient feature of these method is that, by virtue of the Slater-Koster theory, the Slater-Koster parameters depend only on the type of elements in a material, but not on its geometry. For example there is a possibility to use the tight-binding parameters of bcc-Fe to describe a Fe monolayer. Incorporating a model for the description of magnetism (like a Stoner-like-model , section 2.6) a reasonable description of spin-spiral states in this Fe monolayer can be achieved. At least theoretically the method could

be as accurate as the best *ab-initio* methods, if very accurate parameters for a precise description of the electronic structure are used. In the next sections the theory of the tight-binding method is described in detail.

2.2 Basics

The solution of the one-electron Schrödinger equation in a special finite set of basis functions is searched:

$$\mathcal{H}\left|\Psi\right\rangle = (T+V)\left|\Psi\right\rangle = E\left|\Psi\right\rangle \,, \tag{2.3}$$

where T is the one-electron kinetic energy and V is the effective one-electron potential within a mean-field approximation. As basis functions atomic-orbital-like functions $|\boldsymbol{n}, i, \mu\rangle$ are used, where $\boldsymbol{n}$ denotes the Bravais vector $\boldsymbol{R}_n$, i is the i-th basis atom with its position $\boldsymbol{\tau}_i$ in the unit cell and μ stands for the type of orbital. In this work we use s-, p- and d-orbitals as basis functions, with their well-known angular dependence described by the spherical harmonics $Y_{lm}(\Theta, \phi)$.

Using Ritz's variational principle, one has to solve the following matrix-eigenvalue equation:

$$\underline{\boldsymbol{H}} \cdot \boldsymbol{c} = E\underline{\boldsymbol{S}} \cdot \boldsymbol{c}\,, \tag{2.4}$$

where $\boldsymbol{c}$ is an eigenvector containing the coefficients for the linear expansion of $|\Psi\rangle$:

$$\left|\Psi\right\rangle = \sum_{\boldsymbol{n},i,\mu} c_{\boldsymbol{n}i\mu} \cdot \left|\boldsymbol{n}, i, \mu\right\rangle \,, \tag{2.5}$$

and $\underline{\boldsymbol{H}}$ and $\underline{\boldsymbol{S}}$ are the Hamiltonian and overlap matrix in representation of the atomic orbitals:

$$H^{\boldsymbol{m}j\nu}_{\boldsymbol{n}i\mu} = \left\langle \boldsymbol{n}, i, \mu\right| \mathcal{H} \left|\boldsymbol{m}, j, \nu\right\rangle \,, \tag{2.6}$$

$$\text{and} \qquad S^{\boldsymbol{m}j\nu}_{\boldsymbol{n}i\mu} = \left\langle \boldsymbol{n}, i, \mu|\boldsymbol{m}, j, \nu\right\rangle . \tag{2.7}$$

In this work periodic structures are considered, therefore Bloch's theorem can be used. Thus, we can introduce a new basis of Bloch-waves of the following form:

$$\left|\Phi_{\boldsymbol{k},i,\mu}\right\rangle = \frac{1}{\sqrt{N}} \sum_n \mathrm{e}^{\mathrm{i}\boldsymbol{k}\cdot(\boldsymbol{R}_n+\boldsymbol{\tau}_i)} \cdot \left|\boldsymbol{n}, i, \mu\right\rangle \,, \tag{2.8}$$

where N ist the number of unit-cells in the chosen super-cell for the periodic boundary conditions. In the representation of the Bloch-waves the Hamiltonian appears as follows:

$$H^{j\nu}_{i\mu}(\boldsymbol{k}) = \left\langle \Phi_{\boldsymbol{k},i,\mu}\right| \mathcal{H} \left|\Phi_{\boldsymbol{k},j,\nu}\right\rangle = \sum_n \mathrm{e}^{\mathrm{i}\boldsymbol{k}\cdot(\boldsymbol{R}_n+\boldsymbol{\tau}_j-\boldsymbol{\tau}_i)} \cdot H^{\boldsymbol{n}j\nu}_{\boldsymbol{0}i\mu} \,. \tag{2.9}$$

A completely analogous equation defines the matrix elements $S^{j\nu}_{i\mu}(\boldsymbol{k})$ of the overlap matrix:

$$S^{j\nu}_{i\mu}(\boldsymbol{k}) = \langle \Phi_{\boldsymbol{k},i,\mu}|\Phi_{\boldsymbol{k},j,\nu}\rangle = \sum_n \mathrm{e}^{\mathrm{i}\boldsymbol{k}\cdot(\boldsymbol{R}_n+\boldsymbol{\tau}_j-\boldsymbol{\tau}_i)} \cdot S^{\boldsymbol{n}j\nu}_{\boldsymbol{0}i\mu} \,. \tag{2.10}$$

The Bloch-waves are orthogonal for different $\boldsymbol{k}$-values in the Brillouin-zone:

$$\langle \Phi_{\boldsymbol{k},i,\mu} | \Phi_{\boldsymbol{k'},j,\nu} \rangle = 0 \quad , \quad \text{if} \quad \boldsymbol{k} \neq \boldsymbol{k'} \, . \tag{2.11}$$

Also the Hamiltonian in representation of the Bloch-waves is block-diagonal with respect to the $\boldsymbol{k}$-space, i.e.:

$$\langle \Phi_{\boldsymbol{k},i,\mu} | \, \mathcal{H} \, | \Phi_{\boldsymbol{k'},j,\nu} \rangle = 0 \quad , \quad \text{if} \quad \boldsymbol{k} \neq \boldsymbol{k'} \, . \tag{2.12}$$

In a parametrized tight-binding scheme the matrix elements $H_{\mathbf{0}i\mu}^{\boldsymbol{n}j\nu}$ and $S_{\mathbf{0}i\mu}^{\boldsymbol{n}j\nu}$ are described by a parametrization, which will be introduced in the next section.

To conclude, at the heart of the tight-binding theory lies the use of localized basis functions as basis representation, and in this work we use atomic orbitals for this purpose.

2.3 Parametrization of the matrix elements

In this section the parametrization for the matrix elements $H_{\mathbf{0}i\mu}^{\boldsymbol{n}j\nu}$ and $S_{\mathbf{0}i\mu}^{\boldsymbol{n}j\nu}$ is described. First, it is important to take a look at the different types of matrix elements which appear. For the sake of simplicity only the case of one basis atom is considered.

$$\begin{aligned} H_{\mathbf{0}\mu}^{\boldsymbol{n}\nu} &= \int d\boldsymbol{r} \, \phi_\mu^*(\boldsymbol{r}) \cdot (T+V) \cdot \phi_\nu(\boldsymbol{r} - \boldsymbol{R}_n) \\ &= \int d\boldsymbol{r} \, \phi_\mu^*(\boldsymbol{r}) \cdot (T + \sum_m v_{\mathrm{at}}(\boldsymbol{r} - \boldsymbol{R}_m)) \cdot \phi_\nu(\boldsymbol{r} - \boldsymbol{R}_n) \, , \end{aligned} \tag{2.13}$$

where $v_{\mathrm{at}}(\boldsymbol{r} - \boldsymbol{R}_m)$ is the atomic potential of the atom in the m-th unit-cell and $\phi_\mu(\boldsymbol{r}) = \langle \boldsymbol{r} | \boldsymbol{n}, \mu \rangle$. The following types of integrals can be distinguished.

1-center-integrals:

$$\int d\boldsymbol{r} \, \phi_\mu^*(\boldsymbol{r}) \cdot v_{\mathrm{at}}(\boldsymbol{r}) \cdot \phi_\nu(\boldsymbol{r}) \tag{2.14}$$

$\mu = \nu$: typical on-site atomic orbital energies, ε_μ
$\mu \neq \nu$: small contribution if overlap $\langle \phi_\mu | \phi_\nu \rangle \neq 0$

2-center-integrals:

$$\text{(i)} \qquad \int d\boldsymbol{r} \, \phi_\mu^*(\boldsymbol{r}) \cdot \sum_{n \neq 0} v_{\mathrm{at}}(\boldsymbol{r} - \boldsymbol{R}_n) \cdot \phi_\nu(\boldsymbol{r}) \tag{2.15}$$

$\mu = \nu$: contribution to the on-site energies due to existence of other atoms
$\mu \neq \nu$: "hopping-element" on-site from $\nu \rightarrow \mu$ due to existence of other atoms

$$\text{(ii)} \qquad \int d\boldsymbol{r} \, \phi_\mu^*(\boldsymbol{r}) \cdot v_{\mathrm{at}}(\boldsymbol{r}) \cdot \phi_\nu(\boldsymbol{r} - \boldsymbol{R}) \, , \qquad \boldsymbol{R} \neq \mathbf{0} \tag{2.16}$$

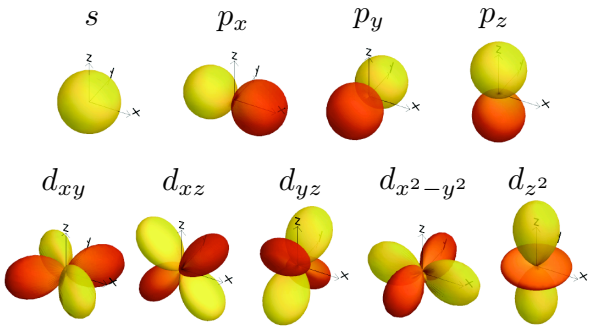

Figure 2.1: Atomic s,p,d orbitals | modified fig. from [26]

typical hopping elements, which describe the electronic transition from $\phi_\nu(\boldsymbol{r}-\boldsymbol{R})$ to $\phi_\mu(\boldsymbol{r})$; usually only the valence electrons are allowed to hop.

3-center-integrals:

$$\int d\boldsymbol{r}\, \phi_\mu^*(\boldsymbol{r}) \cdot v_{\text{at}}(\boldsymbol{r}-\boldsymbol{R}) \cdot \phi_\nu(\boldsymbol{r}-\boldsymbol{R'})\,, \qquad \boldsymbol{R} \neq \boldsymbol{0} \neq \boldsymbol{R'} \neq \boldsymbol{R} \tag{2.17}$$

These integrals are very small for atomic orbitals $\phi_\mu(\boldsymbol{r})$. Therefore they are usually neglected in theoretical tight-binding descriptions. Also in this work they will be neglected in the determination of the tight-binding parameters.

The matrix elements of the kinetic energy T with the atomic orbitals are of the same form as the 1-center-integrals and 2-center-integrals. Therefore the on-site energies and hopping elements contain also the kinetic energy contribution.

Summing up, one needs a parametrization for the on-site elements and hopping integrals. A common parametrization for the hopping elements is the so-called Slater-Koster parametrization [28]. The hopping elements of the type 2.16 are related by symmetry operations which can be exploited to parametrize the hopping elements with a minimal set of parameters, the Slater-Koster parameters, which are described in this section. Each hopping element depends on the distance and the direction of the bonding between the corresponding atoms. Therefore the parametrization of the hopping elements consists of a angular-dependent description via the Slater-Koster transformations and a distance-dependent parametrization by Mehl *et al.* [15, 16].

Slater-Koster parameters The angular dependence of the basis functions $\phi_\nu(\boldsymbol{r}-\boldsymbol{R})$ is described by s- p- and d-orbitals (see fig. 2.1). Essentially these orbitals are linear combinations of the (complex) spherical harmonics. Therefore, the hopping elements consist of the following matrix elements of $\mathcal{H}$ with the (complex) spherical harmonic functions $|l,m\rangle$:

$$\tilde{V}_{ll'm}^{(i\to j)} = \langle \boldsymbol{n}, i, l, m|\, \mathcal{H}\, |\boldsymbol{n'}, j, l', m\rangle \qquad (m = m')\,, \tag{2.18}$$

where l, l' label the angular-momentum quantum number of the orbitals and m the magnetic quantum number of the orbitals. The magnetic quantum numbers m and m' of the atomic orbitals have to be the same due to selection rules. Neglecting the 3-center-integrals, the hopping elements of the Hamiltonian can be described with only 10 types of Slater-Koster parameters, which are shown in fig. 2.2. The Slater-Koster parameters are linear-combinations of the matrix elements 2.18, e.g. the Slater-Koster parameter $V_{sp\sigma}$ is $\tilde{V}_{010}$ or $V_{pp\pi}$ is $\frac{1}{2}(\tilde{V}_{11-1} + \tilde{V}_{111})$ (for more information see [29]). From now on the Slater-Koster parameters are denoted as $V_{ll'm}$, where l,l' are the angular momentum quantum numbers in orbital notation (i.e. s,p,d) and m stands for a σ-, π- or δ-like symmetry of the bonding. As one can see in figure 2.2 these 10 parameters are sufficient to describe a system with one atom per unit-cell ($i = j$) and where only nearest-neighbour coupling along the z-axis as bonding direction is considered. Then the hopping elements of the Hamiltonian would take the following form in the $(s, p_x, p_y, p_z, d_{xy}, d_{xz}, d_{yz}, d_{x^2-y^2}, d_{z^2})$-representation:

$$\underline{\boldsymbol{H}}(R \cdot \boldsymbol{e}_z) = \begin{pmatrix} V_{ss\sigma} & 0 & 0 & V_{sp\sigma} & 0 & 0 & 0 & 0 & V_{sd\sigma} \\ 0 & V_{pp\pi} & 0 & 0 & 0 & 0 & V_{pd\pi} & 0 & 0 \\ 0 & 0 & V_{pp\pi} & 0 & 0 & V_{pd\pi} & 0 & 0 & 0 \\ -V_{sp\sigma} & 0 & 0 & V_{pp\sigma} & 0 & 0 & 0 & 0 & V_{pd\sigma} \\ 0 & 0 & 0 & 0 & V_{dd\delta} & 0 & 0 & 0 & 0 \\ 0 & 0 & -V_{pd\pi} & 0 & 0 & V_{dd\pi} & 0 & 0 & 0 \\ 0 & -V_{pd\pi} & 0 & 0 & 0 & 0 & V_{dd\pi} & 0 & 0 \\ 0 & 0 & 0 & 0 & 0 & 0 & 0 & V_{dd\delta} & 0 \\ V_{sd\sigma} & 0 & 0 & -V_{pd\sigma} & 0 & 0 & 0 & 0 & V_{dd\sigma} \end{pmatrix}, \quad (2.19)$$

where $[\underline{\boldsymbol{H}}]^{\nu}_{\mu}(R \cdot \boldsymbol{e}_z) = H^{\boldsymbol{mj}\nu}_{\boldsymbol{ni}\mu}$ with $\boldsymbol{R}_n - \boldsymbol{R}_m = R \cdot \boldsymbol{e}_z$ ($\boldsymbol{R}_n \neq \boldsymbol{R}_m$) the nearest-neighbour bonding direction and $i = j$.

In general one needs the hopping elements for arbitrary distances and arbitrary directions of the bondings. Of course the hopping elements and also the Slater-Koster parameters depend on the chemical type of the basis atoms.

Angular-dependent parametrization Due to the angular dependence of spherical harmonic functions, all hopping elements along an arbitrary bonding direction $\boldsymbol{R}$ can be expressed as linear combinations of 10 Slater-Koster parameters. One has to rotate the matrix $\underline{\boldsymbol{H}}(R \cdot \boldsymbol{e}_z)$ containing the hopping elements for a bonding direction along the z-axis into the matrix with the hopping elements along the $\boldsymbol{R}$-direction:

$$\underline{\boldsymbol{H}}(\boldsymbol{R}) = \underline{\boldsymbol{U}}^{\dagger} \cdot \underline{\boldsymbol{H}}(R \cdot \boldsymbol{e}_z) \cdot \underline{\boldsymbol{U}}\,, \quad (2.20)$$

where $\underline{\boldsymbol{U}}$ is the unitary matrix, which changes the representation of the s-, p- and d-orbitals with the z-axis as quantization axis into the representation with the $\boldsymbol{R}$-axis as quantization axis. The matrix $\underline{\boldsymbol{U}}$ depends on the directional cosines of the bonding vector $\boldsymbol{R}$ [29]. These transformations are also called Slater-Koster transformations.

The explicit form of all these transformations can be found in the table A.1 in appendix A. One simple example for a hopping element between two atoms with a s- and p_z-orbital is shown in figure 2.3.

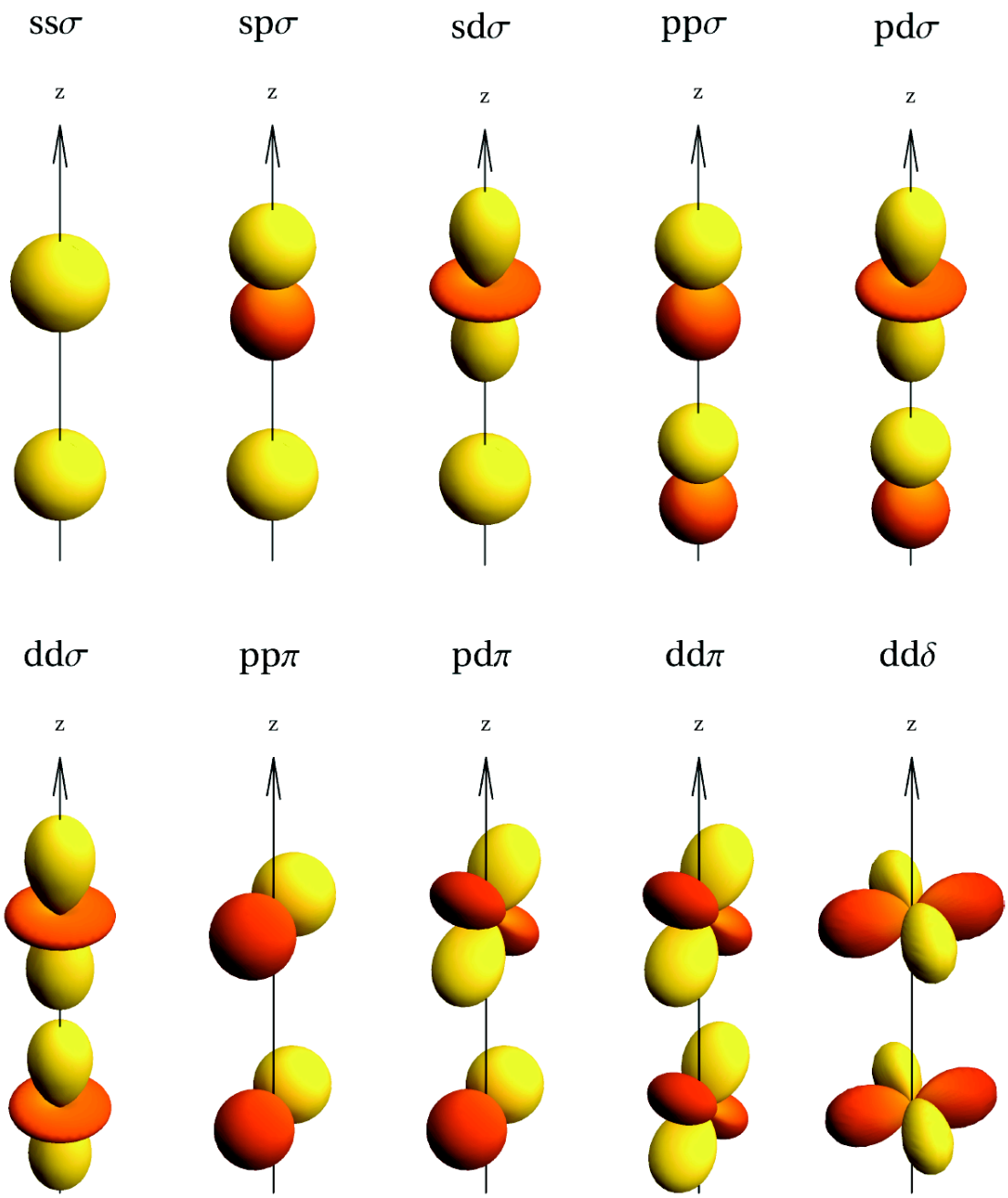

Figure 2.2: All 10 Slater-Koster parameters. σ, π and δ describe the symmetry with respect to the bonding axis and they correspond to magnetic quantum numbers m of the angular momentum. | fig. from [26]

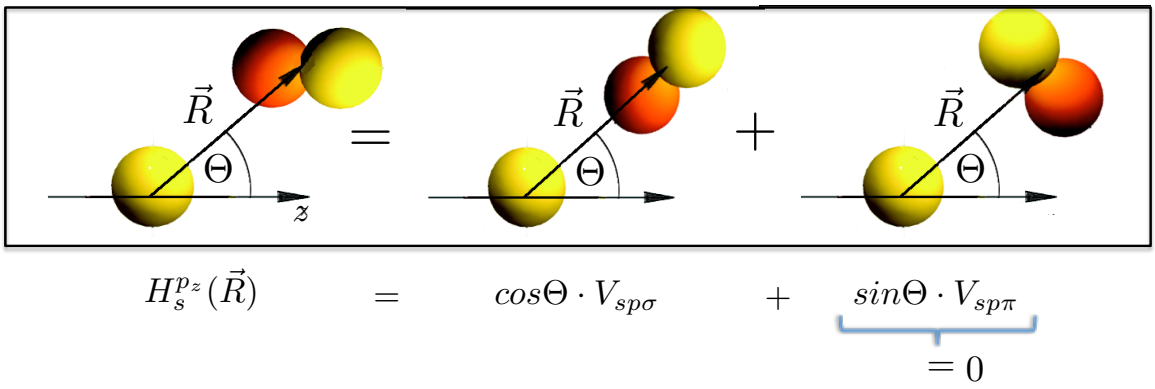

Figure 2.3: Slater-Koster transformation for s and p_z orbital. $H_s^{p_z}$ is a linear combination of the $V_{sp\sigma}$-case and the $V_{sp\pi}$-case, which is zero due to symmetry.

Making use of the Slater-Koster transformations hopping parameters along an arbitrary direction can be expressed by 10 Slater-Koster parameters. Of course the strength of the hopping depends very strongly on the distance between the orbitals. Hence, one needs also a distance-dependent parametrization for the Slater-Koster parameters.

Distance-dependent parametrization There are many distance parametrizations for the Slater-Koster parameters [30, 31, 32, 33]. In this work a distance parametrization by Mehl *et al.* is used [15]. In this parametrization the distance dependence of each Slater-Koster parameter $V_{ll'm}(R)$ is described by 4 other parameters $a_{ll'm}$, $b_{ll'm}$, $c_{ll'm}$ and $d_{ll'm}$:

$$V_{ll'm}^{(i\to j)} = \underbrace{(a_{ll'm}^{(i\to j)} + b_{ll'm}^{(i\to j)} \cdot R + c_{ll'm}^{(i\to j)} \cdot R^2)}_{\text{polynomial part}} \cdot \underbrace{e^{-(d_{ll'm}^{(i\to j)})^2 \cdot R}}_{\text{exp. part}} \cdot f_c(R)\,, \tag{2.21}$$

where

$$f_c(R) = \begin{cases} \frac{1}{1+\exp[(R-R_c+5L_c)/L_c]} & , R \le R_c \\ 0 & , R > R_c \end{cases} \tag{2.22}$$

is a Fermi-Dirac-like cutoff-function with R_c as the cutoff-radius and L_c as the broadening of the cutoff-function. The distances R are in atomic units and the Slater-Koster parameters are in units of Rydberg in the Mehl *et al.* parametrization.

In figure 2.4 one can see the distance-dependent behaviour of some of the Slater-Koster parameters for Fe-Fe hopping elements. The distance parametrization could lead to unphysical Slater-Koster parameters in the case of too small distances. An analogous parametrization is used for the overlap matrix elements.[1]

Besides the hopping elements also a parametrization for the on-site energies is needed, which is of the following form in the Mehl *et al.* parametrization:

$$\epsilon_{i\mu} = (\alpha_{i\mu} + \beta_{i\mu} \cdot \rho_i^{2/3} + \gamma_{i\mu} \cdot \rho_i^{4/3} + \chi_{i\mu} \cdot \rho_i^2) \tag{2.23}$$

[1] When adopting the parametrization scheme of Mehl *et al.* one should take care of the overlap matrix elements, because there are two slightly different parametrizations [17, 18].

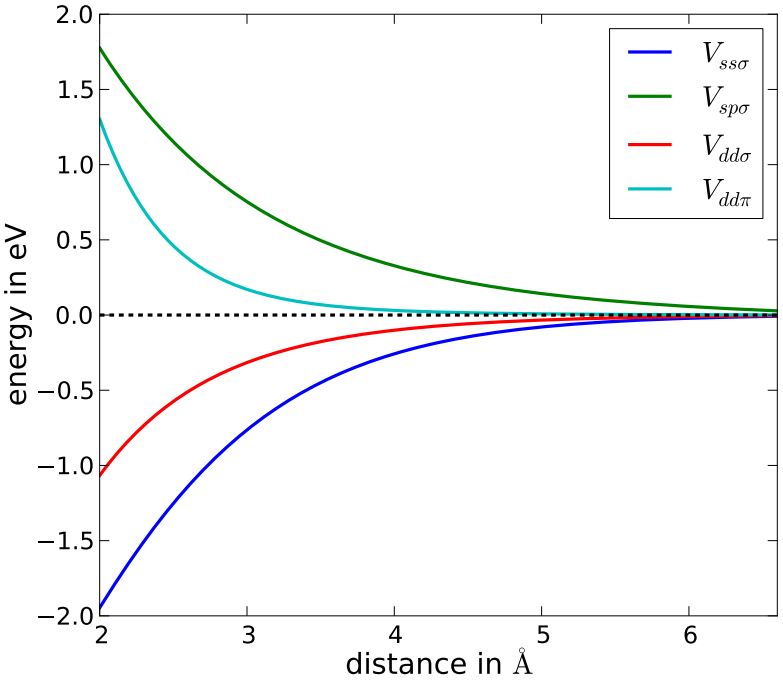

Figure 2.4: Distance-dependence of selected Fe-Fe hopping elements. While the distance parametrization provides reasonable Fe-Fe hopping elements for distances $\geq 2\,\text{Å}$, it is not able to reproduce the behaviour for smaller distances.

with

$$\rho_i = \sum_{j \neq i} e^{-\lambda_j^2 \cdot R_{ij}} \cdot f_c(R_{ij}) \tag{2.24}$$

as local atomic density at atom i with additional parameters λ_j , which depends on the chemical type of the atom j, and $R_{ij} = |\boldsymbol{R}_i - \boldsymbol{R}_j|$ the distance between atom i and j.

In total 80 parameters are needed to describe the hopping elements between chemically equivalent atoms and another 13 parameters for the on-site elements. In this work Fe/Pt-systems are investigated, therefore 93 parameters for the Fe-Fe-bondings and 93 parameters for the Pt-Pt-bondings are used. In principle also 112 parameters would be necessary to describe Fe-Pt-bondings (80 parameters for the Slater-Koster parameters + 4 additional for each $V_{ps\sigma}$, $V_{dp\sigma}$, $V_{dp\pi}$ and $V_{ds\sigma}$), but unfortunately there are no provided parameters for Fe/Pt-compounds by Mehl *et al.* Therefore, the following ansatz is used to describe the Slater-Koster parameters for the Fe-Pt-hopping:

$$V_{ll'm}^{\text{Fe-Pt}} = \frac{1}{2}(V_{ll'm}^{\text{Fe-Fe}} + V_{ll'm}^{\text{Pt-Pt}})\,. \tag{2.25}$$

Although these parameters are a rough approximations, it can be shown that one can obtain reasonable results for Fe-Pt cluster systems using equation [34].

The parameter sets of Mehl *et al.* are fitted to results of *ab-initio* bandstructures of the corresponding equilibrium bulk-geometry. Therefore, these parameters provide a proper

description of (non-magnetic) Fe-bulk and Pt-bulk systems, but are not as accurate for Fe/Pt-systems and especially systems, whose geometry is very different compared to the bulk geometry. This problem is known as transferability problem [35].

It should be mentioned that hopping parameters are not spin-dependent, therefore an additional model Hamiltonian is needed to describe magnetism (see section 2.6). Also only valence electrons have the possibility to hop, whereas the energy of the core electrons is contained in the on-site elements.

2.4 Electronic structure properties

The parametrization by Mehl *et al.* provides a description of the Hamiltonian $H_{i\mu}^{j\nu}(\boldsymbol{k})$ and the overlap matrix $S_{i\mu}^{j\nu}(\boldsymbol{k})$. After solving the eigenvalue-equation

$$\begin{aligned} \underline{\boldsymbol{H}}(\boldsymbol{k}) \cdot \boldsymbol{\Psi}_{i,\mu}(\boldsymbol{k}) &= \varepsilon_{i\mu}(\boldsymbol{k}) \underline{\boldsymbol{S}}(\boldsymbol{k}) \cdot \boldsymbol{\Psi}_{i,\mu}(\boldsymbol{k}) \\ \Leftrightarrow \sum_{j\nu} H_{i\mu}^{j\nu}(\boldsymbol{k}) \cdot (\Psi_{i,\mu})_{j\nu}(\boldsymbol{k}) &= \varepsilon_{i\mu}(\boldsymbol{k}) \sum_{j\nu} S_{i\mu}^{j\nu}(\boldsymbol{k}) \cdot (\Psi_{i,\mu})_{j\nu}(\boldsymbol{k}) \end{aligned} \tag{2.26}$$

one can calculate the Fermi energy, the charges and the density of states (DOS) using the eigenenergies $\varepsilon_{i\mu}(\boldsymbol{k})$ and the eigenvectors $\boldsymbol{\Psi}_{i,\mu}(\boldsymbol{k})$. Starting from now a band index n is introduced, which replaces the indices i, μ in equation 2.26. This prevents from misinterpreting $\varepsilon_{i\mu}(\boldsymbol{k})$ as the eigenenergy of the i-th atom and μ-th orbital.

2.4.1 Fermi energy

The Fermi energy ε_F is determined via the equation

$$N_{e^-} = \sum_{\boldsymbol{k},n} f(\varepsilon_{\boldsymbol{k},n}, \varepsilon_F)\,, \tag{2.27}$$

where

$$f(\varepsilon, \varepsilon_F) = \frac{1}{\exp[\beta \cdot (\varepsilon - \varepsilon_F)] + 1} \tag{2.28}$$

is the Fermi-Dirac distribution function for the electrons and N_{e^-} is the total number of valence electrons in the system. A thermal smearing $\beta^{-1} = k_B \cdot T \approx 1\,\text{meV}$ is introduced to make the calculation of the Fermi energy numerically more stable.

2.4.2 Density of states (DOS)

The DOS is defined as

$$D(\varepsilon) = \sum_{\boldsymbol{k},n} \delta(\varepsilon - \varepsilon_{\boldsymbol{k},n})\,. \tag{2.29}$$

In this work a Lorentzian-broadening function is used instead of the δ-function:

$$D(\varepsilon) = \sum_{\boldsymbol{k},n} \frac{1}{\pi} \cdot \frac{\Gamma}{\Gamma^2 + (\varepsilon - \varepsilon_{\boldsymbol{k},n})^2}\,, \tag{2.30}$$

where Γ is the width of the Lorentzian-function. One has to be very careful in choosing a reasonable Γ: While a very large value smears out fine structure of the DOS, a too small width leads to many sharp peaks in the DOS.

Besides the (total) DOS, it is also enlightening to take a look at the partial DOS, such as atom- and orbital-resolved DOS. The partial DOS of the j-th basis atom and ν-th orbital is calculated as follows:

$$D_{j\nu}(\varepsilon) = \sum_{\boldsymbol{k},n} \delta(\varepsilon - \varepsilon_{\boldsymbol{k},n}) \cdot (\boldsymbol{\Psi}^{\dagger}_{\boldsymbol{k},n})_{j\nu} \cdot (\underline{\boldsymbol{S}}(\boldsymbol{k}) \cdot \boldsymbol{\Psi}_{\boldsymbol{k},n})_{j\nu} \,. \tag{2.31}$$

If an orthogonal set of basis functions would be used, the eigenvectors would be orthonormal: $\boldsymbol{\Psi}^{\dagger}_n \cdot \boldsymbol{\Psi}_m = \delta_{nm}\, \forall n, m$. In the case of a non-orthogonal set of basis functions, it can be shown that

$$\boldsymbol{\Psi}^{\dagger}_n \cdot \underline{\boldsymbol{S}} \cdot \boldsymbol{\Psi}_m = \delta_{nm} \,, \qquad \forall n, m \,. \tag{2.32}$$

With eq. 2.32 follows:

$$D(\varepsilon) = \sum_{j,\nu} D_{j\nu}(\varepsilon) \,. \tag{2.33}$$

2.4.3 Band energy

The band energy is defined as follows:

$$E_{\text{band}} = \sum_{\boldsymbol{k},n} \varepsilon_{\boldsymbol{k},n} \cdot f(\varepsilon_{\boldsymbol{k},n}, \varepsilon_F) \,. \tag{2.34}$$

This is a contribution to the total energy expression (see section 2.5/2.6), where also double-counting terms enter.

2.4.4 Charges

In the following sections the self-consistency of the tight-binding scheme is explained in detail. One fundamental point of the self-consistent cycle is the determination of the atomic charges. The charge calculation for a non-magnetic system is shown here. The charge of the j-th atom in its μ-th orbital displays as follows:

$$n^{\text{Mull}}_{j\nu} = 2 \cdot \sum_{\boldsymbol{k},n} f(\varepsilon_{\boldsymbol{k},n}, \varepsilon_F) \cdot (\boldsymbol{\Psi}^{\dagger}_{\boldsymbol{k},n})_{j\nu} \cdot (\underline{\boldsymbol{S}}(\boldsymbol{k}) \cdot \boldsymbol{\Psi}_{\boldsymbol{k},n})_{j\nu} \,, \tag{2.35}$$

where the factor 2 arises due to the spin-degeneracy in a non-magnetic system. To be precise, the above charges are the so-called Mulliken charges. They fulfil the normalization condition

$$\sum_{j,\nu} n^{\text{Mull}}_{j\nu} = N_{e^-} \,, \tag{2.36}$$

whereas the so-called net charges

$$n^{\text{net}}_{j\nu} = 2 \cdot \sum_{\boldsymbol{k},n} f(\varepsilon_{\boldsymbol{k},n}, \varepsilon_F) \cdot (\boldsymbol{\Psi}^{\dagger}_{\boldsymbol{k},n})_{j\nu} \cdot (\boldsymbol{\Psi}_{\boldsymbol{k},n})_{j\nu} \,, \tag{2.37}$$

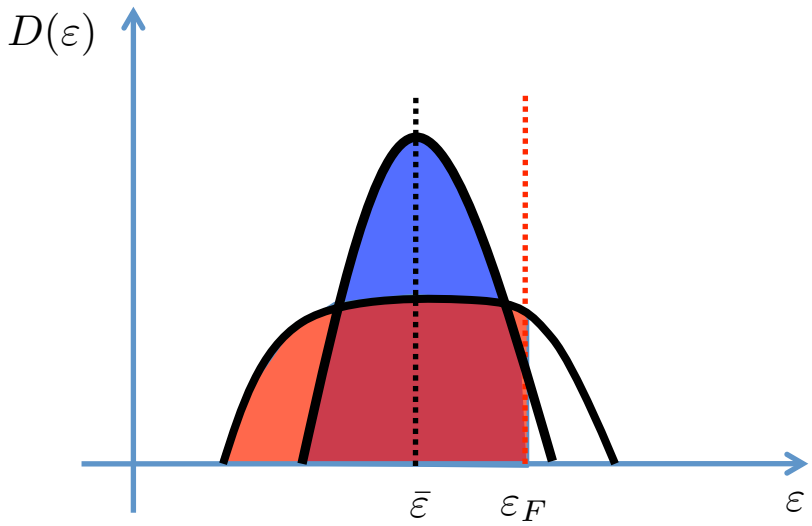

Figure 2.5: Charge transfer to the surface-atoms in a simple DOS model. Red and blue filling in the figure represents the filling of the electrons in the bulk DOS and surface DOS; the area under the two curves and the Fermi energy is the same, therefore there is more charge on the surface-atom

do not fulfil eq. 2.36. Net charges and Mulliken charges are identical for an orthogonal set of basis functions.

2.5 Local charge neutrality

In the parametrized tight-binding scheme described in section 2.3 the on-site energies are fixed. This could lead to problems in calculating the charges for systems of low symmetry such as slab systems or systems with non-equivalent basis atoms. One can obtain non-physical results due to large charge transfers and a constraint for the charge becomes necessary. The reason for the occurrence of these large charge transfers can be understood in a simple DOS model for a thick slab system. In the following the local (atom-specific) DOS of a surface-atom and of an atom in the bulk-like middle of the slab system are compared. For the sake of simplicity the on-site energy of the surface atom and bulk atom is fixed to the same value and the local DOS is symmetric with respect to its center value ε. The width of the local DOS depends on the hopping elements and the number of neighbours. Typically the width of the DOS for the surface atom is smaller than for the bulk-atom. In figure 2.5 the charge transfer to the surface atoms is clearly visible. To prevent very large charge transfers, the following ansatz for a constraint is used:

$$E_{\mathrm{LCN}} = \frac{U_{\mathrm{LCN}}}{2} \cdot \sum_i (n_i^{\mathrm{Mull}} - n_i^0)^2 \,, \tag{2.38}$$

where n_i^{Mull} is the Mulliken charge on the i-th atom, n_i^0 is the (desired) bulk-value of the Mulliken charge and U_{LCN} is the local charge neutrality constant. For simplicity the following derivation is done only for an orthogonal set of basis functions, therefore $n_i := n_i^{\text{Mull}} = n_i^{net}$. To determine the form of Hamiltonian, which corresponds to the above energy E_{LCN}, one should minimize the following Lagrange function:

$$F = E_{\text{tot}}^0 + \frac{U_{\text{LCN}}}{2} \cdot \sum_i (n_i - n_i^0)^2 + \sum_{\boldsymbol{k},n} \alpha_{\boldsymbol{k},n} \cdot \left[|\boldsymbol{\Psi}_{\boldsymbol{k},n}|^2 - 1 \right], \tag{2.39}$$

where

$$E_{\text{tot}}^0 = \sum_{\boldsymbol{k},n} f(\varepsilon_{\boldsymbol{k},n}, \varepsilon_F) \cdot \sum_{\mu,\nu} \sum_{i,j} (\boldsymbol{\Psi}_{\boldsymbol{k},n}^\dagger)_{i\mu} \cdot (\boldsymbol{\Psi}_{\boldsymbol{k},n})_{j\nu} \cdot [H_0]_{i\mu}^{j\nu} \tag{2.40}$$

is the total energy without the constraints and the remaining two terms are the constraints. The first constraint is the local charge neutrality term (see eq. 2.38) and the other one takes into account the normalization of the wave functions.

$$\begin{aligned} F &= \sum_{\boldsymbol{k},n} f(\varepsilon_{\boldsymbol{k},n}, \varepsilon_F) \sum_{i,j} \sum_{\mu,\nu} (\boldsymbol{\Psi}_{\boldsymbol{k},n}^\dagger)_{i\mu} \cdot (\boldsymbol{\Psi}_{\boldsymbol{k},n})_{j\nu} \cdot [H_0]_{i\mu}^{j\nu} + \\ &\quad \frac{U_{\text{LCN}}}{2} \cdot \sum_i \left[\sum_{\boldsymbol{k},n,\mu} |(\boldsymbol{\Psi}_{\boldsymbol{k},n})_{i\mu}|^2 \cdot f(\varepsilon_{\boldsymbol{k},n}, \varepsilon_F) - n_i^0 \right]^2 + \sum_{\boldsymbol{k},n} \alpha_{\boldsymbol{k},n} \cdot \left[\sum_{i,\mu} |(\boldsymbol{\Psi}_{\boldsymbol{k},n})_{i\mu}|^2 - 1 \right] \\ \Rightarrow &\quad \frac{1}{f(\varepsilon_{\boldsymbol{k},n}, \varepsilon_F)} \cdot \frac{\partial F}{\partial (\boldsymbol{\Psi}_{\boldsymbol{k},n}^\dagger)_{i\mu}} \\ = &\quad \sum_{j\nu} [H_0]_{i\mu}^{j\nu} \cdot (\boldsymbol{\Psi}_{\boldsymbol{k},n})_{j\nu} + U_{\text{LCN}} \cdot (n_i - n_i^0) \cdot (\boldsymbol{\Psi}_{\boldsymbol{k},n})_{i\mu} + \tilde{\alpha}_{\boldsymbol{k},n} \cdot (\boldsymbol{\Psi}_{\boldsymbol{k},n})_{i\mu} = 0 \end{aligned}$$

The Lagrange parameters $-\tilde{\alpha}_{\boldsymbol{k},n} = -\frac{\alpha_{\boldsymbol{k},n}}{f(\varepsilon_{\boldsymbol{k},n}, \varepsilon_F)}$ can be identified as bandenergies $\varepsilon_{\boldsymbol{k},n}$ of an eigenvalue problem for the Hamiltonian:

$$H_{i\mu}^{j\nu} = [H_0]_{i\mu}^{j\nu} + U_{\text{LCN}} \cdot (n_i - n_i^0) \cdot \delta_{ij} \delta_{\mu\nu} \,. \tag{2.41}$$

What is the physics behind the local charge neutrality constraint?

The constraint for the charge neutrality shifts the on-site energies depending on $(n_i - n_i^0)$. If $(n_i - n_i^0) < 0$ the on-site energy of the corresponding atom is decreased, so that the charge on this atom increases (see figure 2.5). The parameter U_{LCN} in the charge constraint has to be chosen large enough to assure $n_i \approx n_i^0$. Theoretically n_i is equal n_i^0 for $U_{\text{LCN}} \to \infty$, but of course this can not be used numerically. A good value for preventing large charge transfers is $U_{\text{LCN}} = 5\,\text{eV}$.

With the local charge neutrality term the Hamiltonian depends on the charges and the charges itself are calculated from the eigenvectors and eigenenergies of the Hamiltonian. This leads to the possibility to calculate the charges of the system in a self-consistent scheme. In figure 2.6 the self-consistent scheme is displayed. Besides the above linear mixing, which converges very slowly, but is very stable, there is also the possibility to use Broyden mixing [36] for faster convergence.

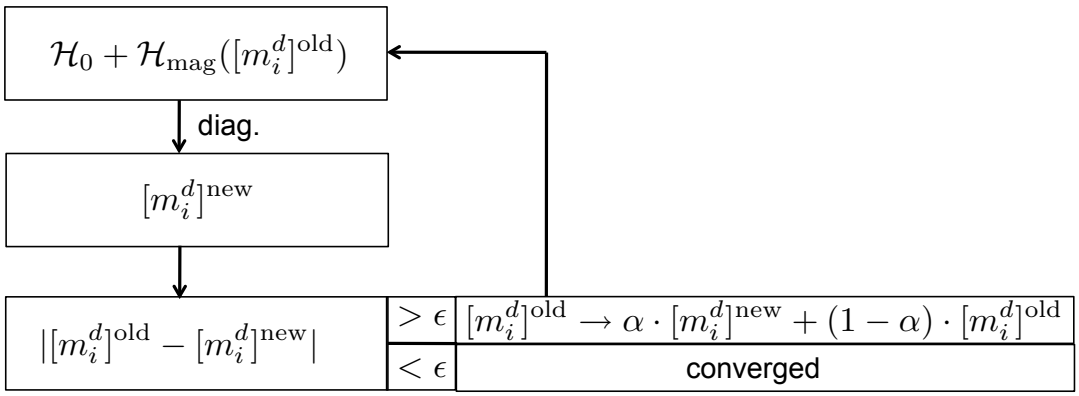

Figure 2.6: Self-consistent cycle via the local charge neutrality.

For a system with equivalent atoms the Hamiltonian is fixed to the parametrized Hamiltonian, which is described in section 2.3. Therefore the self-consistent charge calculation yields no advantages for homogeneous systems. But for systems with inequivalent atoms, the on-site energies are shifted due to the local charge neutrality constraint until the system reaches a stable equilibrium with respect to the charges.

In the self-consistent scheme with the local charge neutrality, the band energy 2.34 is not the whole part of the total energy and there is a double counting part, which has to be taken into account. This double counting term is not derived in the following, but in the section on the Stoner-model (see section 2.6) an additional double counting term is introduced, which derivation (eqs. 2.55-2.58) shows how one can derive eq. 2.43. The total energy has the following form:

$$E_{\mathrm{tot}} = E_{\mathrm{band}} - \frac{U_{\mathrm{LCN}}}{2} \cdot \sum_i (n_i^2 - (n_i^0)^2)\,. \tag{2.42}$$

For systems with identical basis atoms, $n_i^0 = n^0$, the double counting can be rewritten as

$$\frac{U_{\mathrm{LCN}}}{2} \cdot \sum_i (n_i - n_i^0)^2 \tag{2.43}$$

using charge conservation $\sum_i n_i = \sum_i n_0$.

All equations throughout this section are valid only for an orthogonal set of basis functions. For a non-orthogonal set of basis functions the charge n_i in the equations 2.41-2.43 has to be replaced by the Mulliken charge n_i^{Mull} and the additional charge constraint in the Hamiltonian has the following form:

$$\frac{U_{\mathrm{LCN}}}{2} \cdot \left((n_i^{\mathrm{Mull}} - n_i^0) + (n_j^{\mathrm{Mull}} - n_j^0)\right) \cdot S_{i\mu}^{j\nu}\,. \tag{2.44}$$

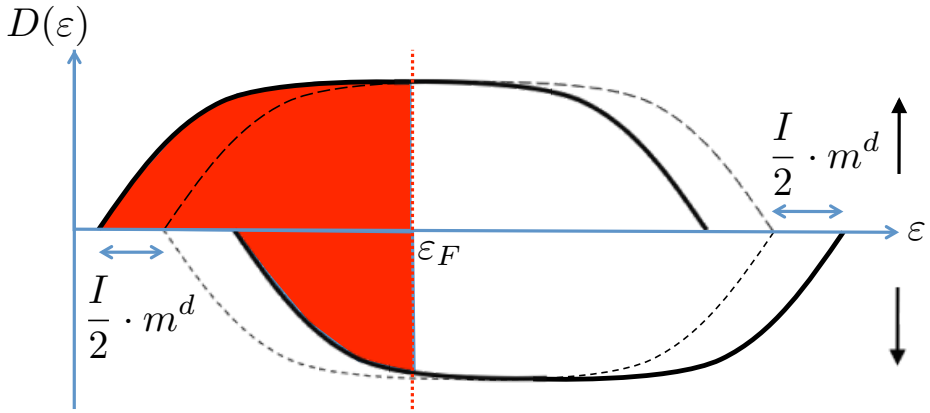

Figure 2.7: Stoner model in a simple DOS picture. The dashed lines display the DOS of the non-magnetic case. Due to an exchange splitting introduced by the Stoner model the DOS is shifted depending on its spin. The band filling, represented by the red colour, is different in the spin channels. Therefore the system develops a magnetic moment.

2.6 Stoner model

As mentioned in section 2.3 the parametrization for the hopping elements does not include magnetism, because the hopping elements are spin independent, i.e. $V_{ll'm}^{\uparrow\to\uparrow} = V_{ll'm}^{\downarrow\to\downarrow}$ and $V_{ll'm}^{\uparrow\to\downarrow} = 0$. In this work a simple Stoner model is applied to model magnetism. Here, an exchange splitting between the electronic majority-bands ($\uparrow$-bands) and minority-bands ($\downarrow$-bands) is introduced in the same way as in the original Stoner model [19, 20]. The exchange splitting depends on the magnetic d-moment of the corresponding atom and a Stoner parameter I:

$$\varepsilon_{i\mu}^{\text{exc}} = I_{i\mu} \cdot m_i^d \,. \tag{2.45}$$

The calculation of the magnetic moments in the tight-binding framework is explained later. At the moment it is enough to know, that $m_i^d = N_{i,d}^{\uparrow} - N_{i,d}^{\downarrow}$ for collinear magnets, where $N_{i,d}^{\sigma}\,(\sigma = \uparrow, \downarrow)$ is the number of electrons in the $\uparrow$- , $\downarrow$-d-bands. In figure 2.7 one can see the connection between the exchange splitting and the filling of $\uparrow$- and $\downarrow$-bands via a simple DOS consideration.

For the case of collinear magnetism the Stoner-part of the Hamiltonian in spin-space has the following form:

$$[H_{\text{mag}}]_{i\mu}^{j\nu} = \begin{pmatrix} -\frac{I_{i\mu}}{2} \cdot m_i^d & 0 \\ 0 & \frac{I_{i\mu}}{2} \cdot m_i^d \end{pmatrix} \cdot \delta_{ij}\delta_{\mu\nu} \,. \tag{2.46}$$

Therefore the Stoner-part modifies exclusively the on-site energies of the system. In the Stoner-part only the magnetic d-moments are used to determine the exchange splitting, because in $3d$-transition metals (like Fe) the magnetism is originated mainly from the $3d$-electrons. This can be shown again with the help of a simple DOS-model and the Stoner criterion: $I \cdot D(\varepsilon_F) > 1$ for ferromagnetic materials, where $D(\varepsilon_F)$ is the DOS at the Fermi energy.

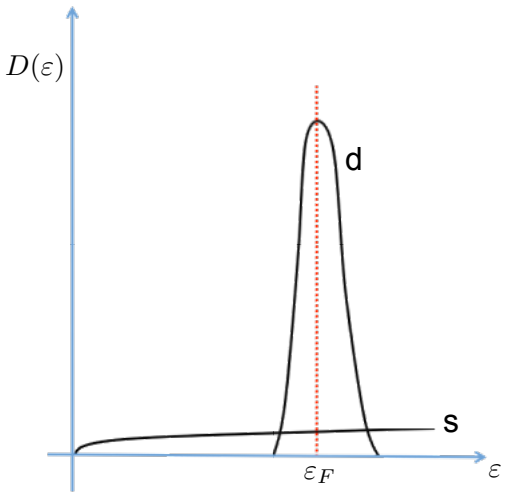

Figure 2.8: Simplified DOS of a $3d$-transition metal. The partial DOS in the s-states at the Fermi energy is much lower than the partial DOS in the d-states. Therefore the d-states dominate the magnetic behaviour.

Essential for the formation of ferromagnetism is the density of states at the Fermi energy. In figure 2.8 the simplified DOS of a $3d$-transition metal is shown. Typically for transition metals the DOS at the Fermi energy consists mainly of the partial DOS of the d-orbitals. As a consequence, a small exchange splitting in the d-states lead to large magnetic d-moments, so that $|m^d| \gg |m^s|,|m^p|$. Using only the d-moments to determine the exchange splitting simplifies the below described self-consistent tight-binding calculation without loosing much accuracy.

The Hamiltonian depends on the magnetic d-moments, which are calculated from the eigenenergies and eigenvectors of the Hamiltonian. Now one can calculate the magnetic moments in a self-consistent scheme until convergence is reached. In figure 2.9 the self-consistent scheme, together with the local charge neutrality described in section 2.5, is displayed. The local charge neutrality part shifts the on-site energies of the atoms until the charges are converged as described in detail in section 2.5. The Stoner-model modifies also the on-site energies of the system, but now an exchange splitting between the on-site energies of the $\uparrow$- and $\downarrow$-bands is introduced. This splitting changes during the self-consistent scheme until the magnetic moments are converged. In the converged case the system has reached a stable equilibrium with respect to the charges and the magnetic moments.

Now one should take a look, how these magnetic moments can be calculated. The magnetic moments and also the (net-)charges can be determined with the help of the density matrix $\underline{\boldsymbol{\rho}}$. The density matrix for the i-th atom and μ-th orbital has the following form in spin-space with the z-axis as quantization axis:

$$\underline{\boldsymbol{\rho}}_{i\mu} = \begin{pmatrix} \rho_{i\mu}^{\uparrow\uparrow} & \rho_{i\mu}^{\uparrow\downarrow} \\ \rho_{i\mu}^{\downarrow\uparrow} & \rho_{i\mu}^{\downarrow\downarrow} \end{pmatrix} , \tag{2.47}$$

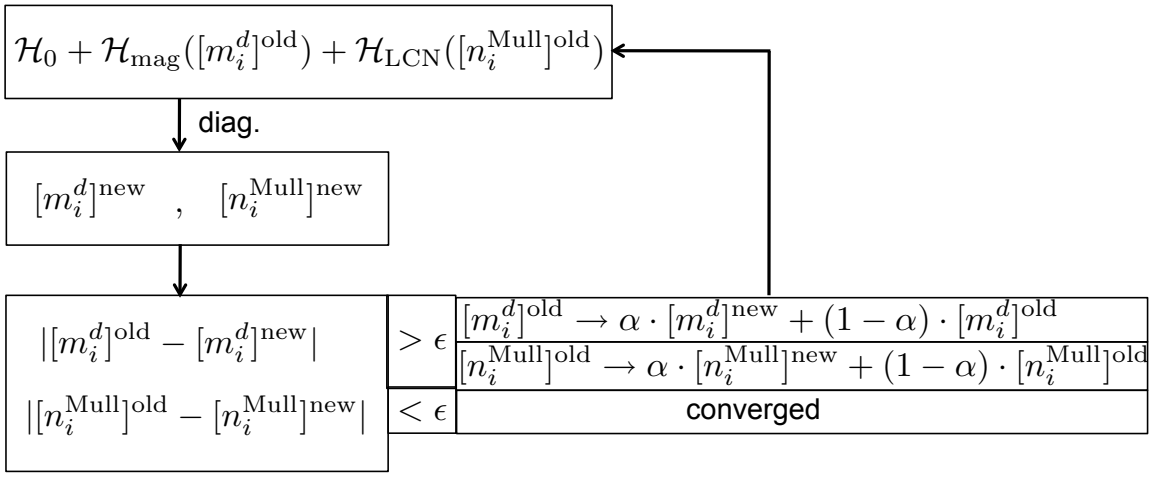

Figure 2.9: Self-consistent cycle via the Stoner part and the local charge neutrality

with

$$\rho_{i\mu}^{\sigma\sigma'} = \sum_{\boldsymbol{k},n} f(\varepsilon_{\boldsymbol{k},n}, \varepsilon_F) \cdot (\boldsymbol{\Psi}_{\boldsymbol{k},n}^{\dagger})_{i\mu}^{\sigma} \cdot (\boldsymbol{\Psi}_{\boldsymbol{k},n})_{i\mu}^{\sigma'} . \tag{2.48}$$

The (net-)charge of the i-th atom and μ-th orbital is the trace of the density matrix:

$$n_{i\mu}^{\mathrm{net}} = tr[\underline{\boldsymbol{\rho}}_{i\mu}] = \rho_{i\mu}^{\uparrow\uparrow} + \rho_{i\mu}^{\downarrow\downarrow} . \tag{2.49}$$

In the special case of a non-magnetic system one obtains the result 2.37. The magnetic moment of the i-th atom and μ-th orbital can be determined for all the three spatial directions as follows:

$$(\boldsymbol{m}_{i\mu})_x = 2\,\mathrm{Re}[\rho_{i\mu}^{\uparrow\downarrow}] \tag{2.50}$$

$$(\boldsymbol{m}_{i\mu})_y = 2\,\mathrm{Im}[\rho_{i\mu}^{\uparrow\downarrow}] \tag{2.51}$$

$$(\boldsymbol{m}_{i\mu})_z = \rho_{i\mu}^{\uparrow\uparrow} - \rho_{i\mu}^{\downarrow\downarrow} \tag{2.52}$$

These equations can be directly derived from the definition

$$[\boldsymbol{m}_{i\mu}]_\alpha = tr[\underline{\boldsymbol{\rho}}_{i\mu}^{\dagger} \cdot \underline{\boldsymbol{\sigma}}_\alpha] \qquad \alpha = x, y, z , \tag{2.53}$$

where $\underline{\boldsymbol{\sigma}}_\alpha$ are the well-known Pauli-matrices. Similarly to the charges there is a distinction between magnetic net moments and magnetic Mulliken moments. With eqs. 2.50-2.52 the magnetic net moments are calculated, whereas the magnetic Mulliken moments can be determined by

$$[\rho_{i\mu}^{\sigma\sigma'}]^{\mathrm{Mull}} = \sum_{\boldsymbol{k},n} f(\varepsilon_{\boldsymbol{k},n}, \varepsilon_F) \cdot (\boldsymbol{\Psi}_{\boldsymbol{k},n}^{\dagger})_{i\mu}^{\sigma} \cdot (\underline{\boldsymbol{S}}(\boldsymbol{k}) \cdot \boldsymbol{\Psi}_{\boldsymbol{k},n})_{i\mu}^{\sigma'} . \tag{2.54}$$

Normally, one should use here the Mulliken moments. However, using the net moments instead of the Mulliken moments does not make a big difference in the converged results and one could stick to the simpler net moments.

We close this section with a derivation of an expression for the exchange energy contribution to the total energy as promised in section 2.5. The total energy E_{tot} is not any more only the band energy E_{band} (see eq. 2.34), there is a double counting term, which has to be considered. One can show [37], that the total energy of the Hamiltonian $\mathcal{H}_0 + \mathcal{H}_{\text{mag}}$ is

$$E_{\text{tot}} = E^0_{\text{tot}} - \frac{1}{4}\sum_{i,\mu} I_{i,\mu} \cdot m_i^\mu \cdot m_i^d \,, \tag{2.55}$$

where

$$E^0_{\text{tot}} = \sum_{\boldsymbol{k},n} f(\varepsilon_{\boldsymbol{k},n}, \varepsilon_F) \cdot \sum_{\mu,\nu}\sum_{i,j}\sum_{\sigma,\sigma'} (\boldsymbol{\Psi}^\dagger_{\boldsymbol{k},n})^\sigma_{i\mu} \cdot (\boldsymbol{\Psi}_{\boldsymbol{k},n})^{\sigma'}_{j\nu} \cdot [H_0]^{j\nu\sigma'}_{i\mu\sigma} \tag{2.56}$$

is the total energy of the non-magnetic system. Easily accessible is the band energy, which is calculated in the following:

$$\begin{aligned}
E_{\text{band}} &= \sum_{\boldsymbol{k},n} f(\varepsilon_{\boldsymbol{k},n}, \varepsilon_F) \cdot \varepsilon_{\boldsymbol{k},n} \\
&= \sum_{\boldsymbol{k},n} f(\varepsilon_{\boldsymbol{k},n}, \varepsilon_F) \cdot \sum_{\mu,\nu}\sum_{i,j}\sum_{\sigma,\sigma'} (\boldsymbol{\Psi}^\dagger_{\boldsymbol{k},n})^\sigma_{i\mu} \cdot (\boldsymbol{\Psi}_{\boldsymbol{k},n})^{\sigma'}_{j\nu} \cdot \\
&\quad \left([H_0]^{j\nu\sigma'}_{i\mu\sigma} - \frac{I_{i,\mu}}{2} \cdot \sigma \cdot m_i^d \cdot \delta_{\sigma\sigma'}\delta_{ij}\delta_{\mu\nu} \right) \\
&= E^0_{\text{tot}} - \sum_{\boldsymbol{k},n} f(\varepsilon_{\boldsymbol{k},n}, \varepsilon_F) \sum_{i,\mu,\sigma} |(\boldsymbol{\Psi}_{\boldsymbol{k},\boldsymbol{n}})^\sigma_{i\mu}|^2 \cdot \frac{I_{i,\mu}}{2} \cdot m_i^d \cdot \sigma \\
&= E^0_{\text{tot}} - \sum_{i,\mu} \frac{I_{i,\mu}}{2} \cdot m_i^d \cdot m_i^\mu \,.
\end{aligned} \tag{2.57}$$

If one compares eq. 2.55 with eq. 2.57, one can determine the double counting:

$$E_{\text{tot}} = E_{\text{band}} + \sum_i \frac{I_{i,\mu}}{4} \cdot m_i^\mu \cdot m_i^d \,. \tag{2.58}$$

2.7 Spin-orbit coupling

The spin-orbit coupling (SOC) is a relativistic effect with the energy scale well below 0.5 eV. A very important aspect of SOC is the symmetry breaking it causes in a ferromagnet. Many interesting effects like the Rashba-splitting [38] or the Dzyaloshinskii-Moriya interaction (DMI) [3, 4], which is introduced in section 2.10 of this thesis, are based on SOC.

Due to the relativistic nature of SOC one has to examine the Dirac equation to understand its origin. In a non-relativistic expansion of the Dirac equation the following expression for SOC can be derived [39]:

$$H_{\text{SOC}} \propto (\nabla V(\boldsymbol{r}) \times \boldsymbol{p}) \cdot \boldsymbol{\sigma} \,, \tag{2.59}$$

where $\boldsymbol{\sigma}$ is the vector containing the Pauli-matrices, $V(\boldsymbol{r})$ is the electrostatic potential and $\boldsymbol{p}$ is the momentum of the electron. In solids the electric field, i.e. $\nabla V(\boldsymbol{r})$, is strongest close to the nucleus, where the potential is almost spherical. Therefore using a spherical potential $V(\boldsymbol{r}) = V(r)$ is a good approximation and the expression 2.59 can be rewritten:

$$H_{\mathrm{SOC}} = \xi(r) \cdot \boldsymbol{L} \cdot \boldsymbol{S}\,, \tag{2.60}$$

with $\boldsymbol{L} = \boldsymbol{r} \times \boldsymbol{p}$ the angular momentum, $\boldsymbol{S} = \frac{\hbar}{2} \cdot \boldsymbol{\sigma}$ the spin of the electron and the radial-dependent function $\xi(r) = \frac{1}{2m^2c^2} \cdot \frac{1}{r} \cdot \frac{\partial V(r)}{\partial r}$.

In representation of the atomic orbitals, using $\langle \boldsymbol{r} | i\mu \rangle = R_{i\mu}(r) \cdot Y_{\mu}^{(i)}(\Theta, \phi)$ with $R_{i\mu}(r)$ a radial function and $Y_{\mu}^{(i)}(\Theta, \phi)$ a spherical harmonic function, the expression has the following form:

$$\begin{aligned}
(H_{\mathrm{SOC}})_{i\mu\sigma}^{j\nu\sigma'} &= \langle i, \mu, \sigma |\, \xi(r) \cdot \boldsymbol{L} \cdot \boldsymbol{S} \,| j, \nu, \sigma' \rangle \\
&= \underbrace{\frac{\hbar}{2} \left[\int dr \cdot r^2 \xi(r) R_{i\mu}^{*}(r) \cdot R_{j\nu}(r) \right]}_{\xi_{i\mu,j\nu}} \cdot \\
&\qquad \left[\int_0^{2\pi} \int_0^{\pi} d\Theta d\phi \, \sin\Theta \cdot [Y_{\mu}^{(i)}]^{*}(\Theta, \phi) \cdot Y_{\nu}^{(j)}(\Theta, \phi) \cdot \langle \sigma |\, \boldsymbol{L} \cdot \boldsymbol{\sigma} \,| \sigma' \rangle \right] \\
&= \xi_{i\mu,j\nu} \cdot \langle \mu\sigma |\, \boldsymbol{L} \cdot \boldsymbol{\sigma} \,| \nu\sigma' \rangle \ .
\end{aligned}$$

The function $\xi(r)$ is usually localized near $r = 0$, therefore $\xi_{i\mu,j\nu} \approx \delta_{ij}\, \xi_{\mu\nu}$ is a reasonable approximation. The representation of the angular moment $\boldsymbol{L}$ in atomic orbitals, i.e. $L_{\mu}^{\nu} = \langle \mu |\, \boldsymbol{L} \,| \nu \rangle$, can be found in the appendix in A.1. Important to notice is that $\langle \mu |\, \boldsymbol{L} \,| \nu \rangle$ is block-diagonal with respect to s-,p- and d-orbitals. Therefore only three SOC-parameters per basis atom are necessary for describing SOC in tight-binding:

- $\xi_{i,p}$, SOC-parameter of p-orbitals
- $\xi_{i,d}$, SOC-parameter of d-orbitals
- $\xi_{i,f}$, SOC-parameter of f-orbitals

There is no contribution to SOC from the s-orbital due to $l = 0$. In this work the f-orbitals are not used, but usually they have a large contribution to SOC for the rare-earth metals.

Combining these results leads to the following expression for SOC in representation of the atomic orbitals in spin-representation with the z-axis as quantization axis:

$$(H_{\mathrm{SOC}})_{i\mu}^{j\nu} = \xi_{i\mu} \cdot \begin{pmatrix} (L_z)_{\mu}^{\nu} & (L_x)_{\mu}^{\nu} - \mathrm{i} \cdot (L_y)_{\mu}^{\nu} \\ (L_x)_{\mu}^{\nu} + \mathrm{i} \cdot (L_y)_{\mu}^{\nu} & -(L_z)_{\mu}^{\nu} \end{pmatrix} \cdot \delta_{ij}\,, \tag{2.61}$$

where $(L_{\alpha})_{\mu}^{\nu}$ are the aforementioned angular momentum components in atomic orbital representation (see A.1).

For an arbitrary spin quantization axis the SOC-matrix 2.61 has to be rotated with a spin-rotation matrix $\mathcal{U}$ (see eq. 2.66):

$$\tilde{H}_{\mathrm{SOC}} = \mathcal{U} \cdot H_{\mathrm{SOC}} \cdot \mathcal{U}^{\dagger} \,. \tag{2.62}$$

Switching on SOC leads to non-vanishing expectation values for the orbital moments $\langle \boldsymbol{L_i} \rangle$. The following equation is used to determine the orbital moment of the i-th atom:

$$\langle \boldsymbol{L}_i \rangle = \sum_{\boldsymbol{k},n} f(\varepsilon_{\boldsymbol{k},n}, \varepsilon_F) \cdot \sum_{\mu,\nu,\sigma} (\boldsymbol{\Psi}^{\dagger}_{\boldsymbol{k},n})^{\sigma}_{i\mu} \cdot (\boldsymbol{\Psi}_{\boldsymbol{k},n})^{\sigma}_{i\nu} \cdot \boldsymbol{L}^{\nu}_{\mu} \,. \tag{2.63}$$

The above moments are net moments. For a determination of the orbital Mulliken moments one has to include the overlap matrix as in eq. 2.54:

$$\langle \boldsymbol{L}^{\mathrm{Mull}}_i \rangle = \sum_{\boldsymbol{k},n} f(\varepsilon_{\boldsymbol{k},n}, \varepsilon_F) \cdot \sum_{\mu,\nu,\sigma} (\boldsymbol{\Psi}^{\dagger}_{\boldsymbol{k},n})^{\sigma}_{i\mu} \cdot (\underline{\boldsymbol{S}}(\boldsymbol{k}) \cdot \boldsymbol{\Psi}_{\boldsymbol{k},n})^{\sigma}_{i\nu} \cdot \boldsymbol{L}^{\nu}_{\mu} \,. \tag{2.64}$$

2.8 Non-collinear magnetism

2.8.1 Non-collinear magnetism in the unit-cell

Many interesting phenomena appear due to non-collinear magnetism, for example the Néel-state in magnetic frustrated systems [40] or spin-spiral ground states in Cr/W(110) [12], 2Fe/W(110) [8] or even Fe(110)-monolayers [41]. Implementing non-collinear magnetism in the tight-binding scheme is rather straightforward. In figure 2.10 a magnetic moment is pointing in an arbitrary direction, which is defined by the angles Θ and ϕ in the spherical coordinates representation:

$$\boldsymbol{m} = |\boldsymbol{m}| \cdot \begin{pmatrix} \cos\phi \, \sin\Theta \\ \sin\phi \, \sin\Theta \\ \cos\Theta \end{pmatrix} \,. \tag{2.65}$$

We proceed by defining two frames of reference. The global frame is the representation of the spins with the z-axis as quantization axis, whereas the local frame is the representation with the direction of $\boldsymbol{m}$ as quantization axis. The following spin-rotation matrix $\mathcal{U}$ rotates the spin up state $|\uparrow\rangle = \begin{pmatrix} 1 \\ 0 \end{pmatrix}$ of the global frame into the spin up state $|\uparrow\rangle_{\boldsymbol{m}}$ of the local frame [42]:

$$\mathcal{U}(\Theta, \phi) = \begin{pmatrix} \mathrm{e}^{-\mathrm{i}\frac{\phi}{2}} \cdot \cos(\frac{\Theta}{2}) & -\mathrm{e}^{-\mathrm{i}\frac{\phi}{2}} \cdot \sin(\frac{\Theta}{2}) \\ \mathrm{e}^{\mathrm{i}\frac{\phi}{2}} \cdot \sin(\frac{\Theta}{2}) & \mathrm{e}^{\mathrm{i}\frac{\phi}{2}} \cdot \cos(\frac{\Theta}{2}) \end{pmatrix} \,. \tag{2.66}$$

Therefore it follows:

$$|\uparrow\rangle_{\boldsymbol{m}} = \mathcal{U}(\Theta, \phi) \; |\uparrow\rangle = \mathrm{e}^{-\mathrm{i}\frac{\phi}{2}} \cdot \cos\left(\frac{\Theta}{2}\right) \; |\uparrow\rangle + \mathrm{e}^{\mathrm{i}\frac{\phi}{2}} \cdot \sin\left(\frac{\Theta}{2}\right) \; |\downarrow\rangle \,. \tag{2.67}$$

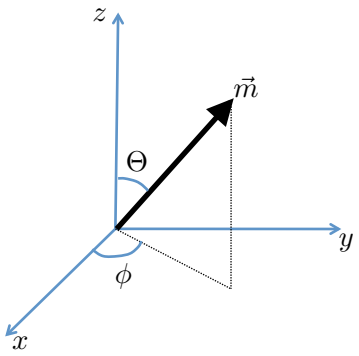

Figure 2.10: Magnetic moment in spherical coordinate representation.

The magnetic part of the Hamiltonian has the following form in its local frame (see eq. 2.46):

$$\begin{aligned}
[H_{\mathrm{mag}}]_{i\mu}^{j\nu} &= \begin{pmatrix} -\frac{I_{i\mu}}{2} \cdot m_i^d & 0 \\ 0 & \frac{I_{i\mu}}{2} \cdot m_i^d \end{pmatrix} \cdot \delta_{ij}\delta_{\mu\nu} \\
&= -\frac{I_{i\mu}}{2} \cdot \boldsymbol{m_i^d} \cdot \boldsymbol{\sigma} \cdot \delta_{ij}\delta_{\mu\nu} \,. \qquad (2.68)
\end{aligned}$$

We will show that this expression is, as expected, invariant under spin-rotations. In the special case of $\boldsymbol{m}_i^d = m_i^d \cdot \boldsymbol{e}_z$ the local frame and global frame are the same. $[H_{\mathrm{mag}}]_{i\mu}^{j\nu}$ can be transformed into the global frame using the transformation matrix $\mathcal{U}$:

$$[H_{\mathrm{mag}}^{\mathrm{global}}]_{i\mu}^{i\mu} = \mathcal{U}(\Theta_i, \phi_i) \cdot [H_{\mathrm{mag}}]_{i\mu}^{i\mu} \cdot \mathcal{U}^{\dagger}(\Theta_i, \phi_i) \,, \qquad (2.69)$$

where Θ_i and ϕ_i are the angles defining the direction of the magnetic moment $\boldsymbol{m}_i^d$. This leads to the following expression:

$$\begin{aligned}
[H_{\mathrm{mag}}^{\mathrm{global}}]_{i\mu}^{i\mu} &= \frac{I_{i\mu}}{2} \cdot \begin{pmatrix} -m_i^d \cdot \cos\Theta_i & -m_i^d \cdot \sin\Theta_i \cdot \mathrm{e}^{-\mathrm{i}\phi_i} \\ -m_i^d \cdot \sin\Theta_i \cdot \mathrm{e}^{\mathrm{i}\phi_i} & m_i^d \cdot \cos\Theta_i \end{pmatrix} \\
&= \frac{I_{i\mu}}{2} \cdot \begin{pmatrix} -(\boldsymbol{m}_i^d)_z & -[(\boldsymbol{m}_i^d)_x - \mathrm{i} \cdot (\boldsymbol{m}_i^d)_y] \\ -[(\boldsymbol{m}_i^d)_x + \mathrm{i} \cdot (\boldsymbol{m}_i^d)_y] & (\boldsymbol{m}_i^d)_z \end{pmatrix} \\
&= -\frac{I_{i\mu}}{2} \cdot \boldsymbol{m}_i^d \cdot \boldsymbol{\sigma} \,. \qquad (2.70)
\end{aligned}$$

The components of the magnetic d-moment $(m_i^d)_\alpha$ are determined via equations 2.50-2.52. Treating non-collinear magnetism using equation 2.69 increases the number of variables in the self-consistent scheme (figure 2.9) by a factor of two. For the collinear case one component of the d-moments $[\boldsymbol{m}_i^d]_\alpha$ is sufficient, whereas the complete vector $\boldsymbol{m}_i^d$ is necessary in the non-collinear case.

Performing self-consistent calculations for a non-collinear case makes it necessary to use another constraint, in addition to the local charge neutrality term, in order to pin the directions of the magnetic moments. Following a scheme of R. Gebauer [43], one

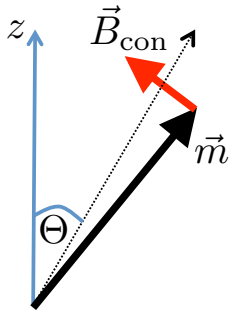

Figure 2.11: Magnetic field $\boldsymbol{B}_{\text{con}}$ in the constraint.

should minimize the following generalized total energy:

$$E_{\text{tot}}[n(\boldsymbol{r}), \boldsymbol{m}(\boldsymbol{r})] = E^0_{\text{tot}}[n(\boldsymbol{r}), \boldsymbol{m}(\boldsymbol{r})] + \lambda \cdot \int d\boldsymbol{r}\, (\boldsymbol{m}(\boldsymbol{r}) - \bar{\boldsymbol{m}}(\boldsymbol{r}))^2\,, \tag{2.71}$$

where $E^0_{\text{tot}}[n(\boldsymbol{r}), \boldsymbol{m}(\boldsymbol{r})]$ is the total energy without the constraint and $\lambda \cdot \int d\boldsymbol{r}\, (\boldsymbol{m}(\boldsymbol{r}) - \bar{\boldsymbol{m}}(\boldsymbol{r}))^2$, with $\bar{\boldsymbol{m}}(\boldsymbol{r})$ the predefined magnetic moment, a constraint for the direction of the magnetic moment. In [43] it is shown, that for our purposes the following constraint is able to pin the Θ-angle of the moments up to a small region around the predefined direction:

$$E_{\text{con}} = \lambda \cdot \sum_i \left(\arccos\left(\frac{[\boldsymbol{m}^d_i]_z}{|\boldsymbol{m}^d_i|} \right) - \Theta_i \right)^2 . \tag{2.72}$$

The Hamiltonian then has to be complemented with the following expression:

$$[H_{\text{con}}]^{j\nu}_{i\mu} = -\boldsymbol{\sigma} \cdot \boldsymbol{B}_{\text{con}}(\boldsymbol{m}^d_i) \cdot \delta_{ij}\delta_{\mu\nu}\,, \tag{2.73}$$

where $\boldsymbol{B}_{\text{con}}$ is a magnetic field, which is perpendicular to $\boldsymbol{m}^d_i$ (figure 2.11) pointing in the direction of the chosen angle. The strength of $\boldsymbol{B}_{\text{con}}$ depends on the difference between the chosen angle Θ_i and the current angle $\arccos\left(\frac{[\boldsymbol{m}^d_i]_z}{|\boldsymbol{m}^d_i|}\right)$:

$$\boldsymbol{B}_{\text{con}} = -\frac{2\lambda \cdot \left(\arccos\left(\frac{[\boldsymbol{m}^d_i]_z}{|\boldsymbol{m}^d_i|} \right) - \Theta_i \right)}{\left(1 - \left(\frac{[\boldsymbol{m}^d_i]_z}{|\boldsymbol{m}^d_i|} \right)^2 \right)^{1/2} \cdot |m^d_i|^3} \cdot \begin{pmatrix} [\boldsymbol{m}^d_i]_z \cdot [\boldsymbol{m}^d_i]_x \\ [\boldsymbol{m}^d_i]_z \cdot [\boldsymbol{m}^d_i]_y \\ -[\boldsymbol{m}^d_i]^2_x - [\boldsymbol{m}^d_i]^2_y \end{pmatrix} . \tag{2.74}$$

The constraint does not fix the absolute value of the magnetic moments due to the fact that $\boldsymbol{B}_{\text{con}}$ is perpendicular to $\boldsymbol{m}^d_i$.

The application of this constraint leads in some cases to problems, particularly in fixing small magnetic moments. This also includes the polarized Pt-moments in Fe/Pt layers, which are discussed in chapter 5.

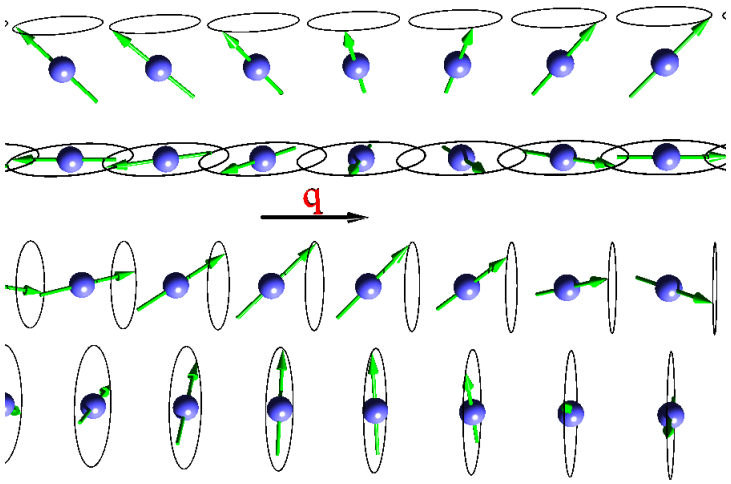

Figure 2.12: Four examples of spin-spirals with spin rotation axis perpendicular (upper two) and parallel (lower two) to the spin-spiral vector $\boldsymbol{q}$. For each case two spirals with cone-angles of $\Theta = \frac{\pi}{2}$ and $\Theta = \frac{\pi}{4}$ are shown.

2.8.2 Spin-spirals

Some materials like Cr/W(110) do not show a ferromagnetic ground state, but rather a spin-spiral structure [12]. A spin-spiral is a periodic magnetic structure, in which the directions of the spins are determined as follows:

$$\boldsymbol{S}_i = \begin{pmatrix} \cos(\boldsymbol{q} \cdot \boldsymbol{R}_n) \cdot \sin\Theta \\ \sin(\boldsymbol{q} \cdot \boldsymbol{R}_n) \cdot \sin\Theta \\ \cos\Theta \end{pmatrix} . \tag{2.75}$$

The cone-angle Θ is the angle between the spins and the rotation axis of the spin-spiral. In equation 2.75 the rotation axis is defined along the z-axis. The rotation angle of the spin-spiral is defined via the spiral vector $\boldsymbol{q}$, which also defines the direction along which the spins are rotated. The rotation angle of the spin at position $\boldsymbol{R}_n$ is defined as $\phi_n = \boldsymbol{q} \cdot \boldsymbol{R}_n$. In figure 2.12 different spin-spirals with cone-angles Θ and spiral-vectors $\boldsymbol{q}$ are displayed.

There are two approaches how to treat spin-spiral systems computationally. One possibility is to describe spin-spirals with rational $|\boldsymbol{q}|$-values in a super-cell using the transformation 2.69 for H_{mag} (see picture 2.13a). A big disadvantage of this method is the huge amount of computational time needed in particular for small q-values. However, within this scheme the implementation of SOC can be done in a straightforward way (see section 2.6).

Another possibility to describe spin-spirals in periodic systems is via the generalized Bloch theorem (see figure 2.13b , [21, 22, 23]). The Bloch theorem according to eq. 2.9 is not any more valid for a spin-spiral due to the non-periodicity of the potential. But if one combines a lattice-translation with the corresponding spin-rotation, each unit-cell is equivalent. Therefore a generalized Bloch theorem remains valid and can be expressed

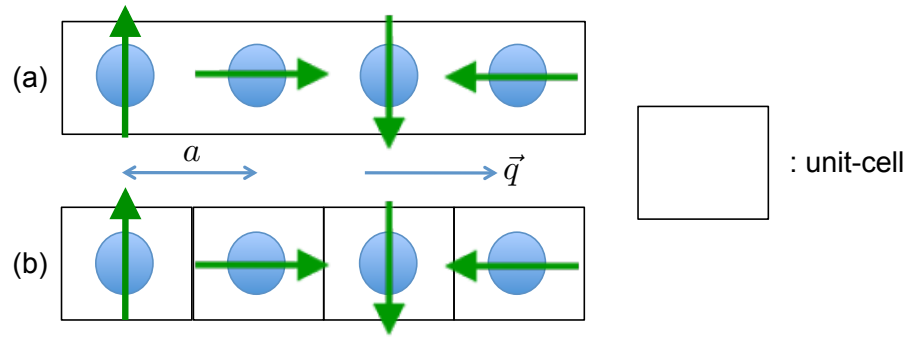

Figure 2.13: Different possibilities of treating spin-spirals: (a) large super-cell for commensurate q-values, (b) generalized Bloch theorem.

as:

$$\mathcal{U}(\boldsymbol{q}\cdot\boldsymbol{R}_n)\cdot\mathcal{T}(\boldsymbol{R}_n)\cdot\begin{pmatrix}\Phi^{\uparrow}(\boldsymbol{k},\boldsymbol{r})\\ \Phi^{\downarrow}(\boldsymbol{k},\boldsymbol{r})\end{pmatrix}=\exp(\mathrm{i}\boldsymbol{k}\cdot\boldsymbol{r})\cdot\begin{pmatrix}\exp(-\frac{\mathrm{i}}{2}\boldsymbol{q}\cdot\boldsymbol{R}_n)\cdot\Phi^{\uparrow}(\boldsymbol{k},\boldsymbol{r})\\ \exp(\frac{\mathrm{i}}{2}\boldsymbol{q}\cdot\boldsymbol{R}_n)\cdot\Phi^{\downarrow}(\boldsymbol{k},\boldsymbol{r})\end{pmatrix}, \tag{2.76}$$

where $\mathcal{T}(\boldsymbol{R}_n)$ is a lattice-translation operator, $\mathcal{U}(\boldsymbol{q}\cdot\boldsymbol{R}_n)$ is a spin-rotation matrix with a rotation angle $\phi_n=\boldsymbol{q}\cdot\boldsymbol{R}_n$ and the z-axis as rotation axis, and $\Phi^{\sigma}(\boldsymbol{k},\boldsymbol{r})\,(\sigma=\uparrow,\downarrow)$ is the σ-component of the Bloch-wave $\Phi(\boldsymbol{k},\boldsymbol{r})$.

As in eq. 2.8 one can construct Bloch-waves, which satisfy the generalized Bloch theorem:

$$|\Phi^{\uparrow}_{i\mu}(\boldsymbol{k})\rangle = \frac{1}{\sqrt{N}}\cdot\sum_n \mathrm{e}^{\mathrm{i}\boldsymbol{k}\cdot(\boldsymbol{R}_n+\boldsymbol{\tau}_i)}\cdot|\boldsymbol{n},i,\mu\rangle\cdot\begin{pmatrix}\mathrm{e}^{-\frac{\mathrm{i}}{2}\boldsymbol{q}\cdot(\boldsymbol{R}_n+\boldsymbol{\tau}_i)}\cdot\cos\frac{\Theta}{2}\\ \mathrm{e}^{\frac{\mathrm{i}}{2}\boldsymbol{q}\cdot(\boldsymbol{R}_n+\boldsymbol{\tau}_i)}\cdot\sin\frac{\Theta}{2}\end{pmatrix} \tag{2.77}$$

$$|\Phi^{\downarrow}_{i\mu}(\boldsymbol{k})\rangle = \frac{1}{\sqrt{N}}\cdot\sum_n \mathrm{e}^{\mathrm{i}\boldsymbol{k}\cdot(\boldsymbol{R}_n+\boldsymbol{\tau}_i)}\cdot|\boldsymbol{n},i,\mu\rangle\cdot\begin{pmatrix}-\mathrm{e}^{-\frac{\mathrm{i}}{2}\boldsymbol{q}\cdot(\boldsymbol{R}_n+\boldsymbol{\tau}_i)}\cdot\sin\frac{\Theta}{2}\\ \mathrm{e}^{\frac{\mathrm{i}}{2}\boldsymbol{q}\cdot(\boldsymbol{R}_n+\boldsymbol{\tau}_i)}\cdot\cos\frac{\Theta}{2}\end{pmatrix}. \tag{2.78}$$

In representation of these Bloch-waves one obtains the following Hamiltonian $H^{j\nu}_{i\mu}(\boldsymbol{k})$:

$$\langle\Phi^{\sigma}_{i\mu}|\,\mathcal{H}\,|\Phi^{\sigma'}_{j\nu}\rangle=[H^{j\nu}_{i\mu}(\boldsymbol{k},\boldsymbol{q})]^{\sigma\sigma'}=\sum_n \mathrm{e}^{\mathrm{i}\boldsymbol{k}\cdot(\boldsymbol{R}_n+\boldsymbol{\tau}_j-\boldsymbol{\tau}_i)}\cdot[s^j_i(\boldsymbol{q}\cdot\boldsymbol{R}_n)]^{\sigma\sigma'}\cdot H^{\boldsymbol{n}j\nu}_{\boldsymbol{0}i\mu}, \tag{2.79}$$

where $[s^j_i(\boldsymbol{q}\cdot\boldsymbol{R}_n)]^{\sigma\sigma'}$ are phase-factors for the $\sigma\sigma'$-components of the Hamiltonian:

$$(s^j_i(\boldsymbol{q}\cdot\boldsymbol{R}_n))^{\uparrow\uparrow} = \mathrm{e}^{-\mathrm{i}\frac{\boldsymbol{q}}{2}\cdot(\boldsymbol{R}_n+\boldsymbol{\tau}_j-\boldsymbol{\tau}_i)}\cdot\cos^2\left(\frac{\Theta}{2}\right)+\mathrm{e}^{\mathrm{i}\frac{\boldsymbol{q}}{2}\cdot(\boldsymbol{R}_n+\boldsymbol{\tau}_j-\boldsymbol{\tau}_i)}\cdot\sin^2\left(\frac{\Theta}{2}\right) \tag{2.80}$$

$$(s^j_i(\boldsymbol{q}\cdot\boldsymbol{R}_n))^{\downarrow\downarrow} = \mathrm{e}^{\mathrm{i}\frac{\boldsymbol{q}}{2}\cdot(\boldsymbol{R}_n+\boldsymbol{\tau}_j-\boldsymbol{\tau}_i)}\cdot\cos^2\left(\frac{\Theta}{2}\right)+\mathrm{e}^{-\mathrm{i}\frac{\boldsymbol{q}}{2}\cdot(\boldsymbol{R}_n+\boldsymbol{\tau}_j-\boldsymbol{\tau}_i)}\cdot\sin^2\left(\frac{\Theta}{2}\right) \tag{2.81}$$

$$(s^j_i(\boldsymbol{q}\cdot\boldsymbol{R}_n))^{\uparrow\downarrow} = 2\mathrm{i}\cdot\sin\left(\frac{\boldsymbol{q}}{2}\cdot(\boldsymbol{R}_n+\boldsymbol{\tau}_j-\boldsymbol{\tau}_i)\right)\cdot\sin\left(\frac{\Theta}{2}\right)\cdot\cos\left(\frac{\Theta}{2}\right) \tag{2.82}$$

$$(s^j_i(\boldsymbol{q}\cdot\boldsymbol{R}_n))^{\downarrow\uparrow} = [(s^j_i(\boldsymbol{q}\cdot\boldsymbol{R}_n))^{\uparrow\downarrow}]^* \tag{2.83}$$

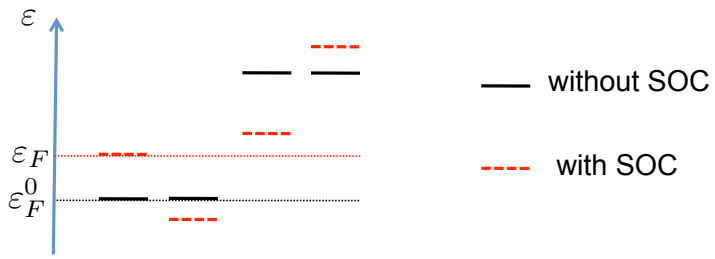

Figure 2.14: Change in the Fermi energy after adding 1st-order SOC contribution. ε_F is the Fermi energy with SOC, whereas ε_F^0 is the Fermi energy without SOC.

In the appendix in A.2 one can find a detailed derivation of these expressions.

Important to notice is that the Hamiltonian $[H_{i\mu}^{j\nu}(\boldsymbol{k},\boldsymbol{q})]^{\sigma\sigma'}$ of eq. 2.79 is expressed in representation of the local spin-frame, which originates that the magnetic part of the Hamiltonian is diagonal in spin (see eq. 2.46). In the local spin-frame the phase-factors $[s_i^j(\boldsymbol{q}\cdot\boldsymbol{R}_n)]^{\sigma\sigma'}$ are a bit more complicated than in the global frame (see [26]), whereas the magnetic Hamiltonian-part is of a simpler structure in the local frame.

The total energy of a spin-spiral system depends on the cone-angle Θ and the spiral-vector $\boldsymbol{q}$. A very insightful quantity is the magnon dispersion $E(\boldsymbol{q})$ of a spin-spiral with fixed cone-angle. This curve $E(\boldsymbol{q})$ can be used to determine the Heisenberg exchange-coupling parameters J_{ij} or the Dzyaloshinskii-Moriya vectors $\boldsymbol{D}_{ij}$ (see section 2.10, equations 2.102 and 2.104). For DMI SOC is necessary, which brings up the question how to implement SOC in the framework of the generalized Bloch theorem. SOC breaks symmetries by introducing a preferred direction for the magnetization, therefore in its presence the generalized Bloch theorem is not valid. Within the generalized Bloch theorem each unit cell, independent of the direction of the magnetic moments, is equivalent. Therefore we add an additional energy-contribution induced by SOC after having calculated the spin-spiral energies without SOC with the generalized Bloch theorem. This is possible if one treats SOC in a perturbation-theoretical way [24, 9]:

$$\varepsilon_{\boldsymbol{k},n}(\boldsymbol{q}) = \varepsilon^0_{\boldsymbol{k},n}(\boldsymbol{q}) + \Delta\varepsilon_{\boldsymbol{k},n}(\boldsymbol{q})\,, \tag{2.84}$$

where $\varepsilon^0_{\boldsymbol{k},n}(\boldsymbol{q})$ is the eigenenergy of the spin-spiral without SOC and

$$\Delta\varepsilon_{\boldsymbol{k},n}(\boldsymbol{q}) = \langle \boldsymbol{\Psi}_{\boldsymbol{k},n}|\, H_{\mathrm{SOC}}\, |\boldsymbol{\Psi}_{\boldsymbol{k},n}\rangle \tag{2.85}$$

the 1st-order contribution due to SOC.

There is a possibility to calculate the new Fermi energy ε_F after adding $\Delta\varepsilon_{\boldsymbol{k},n}(\boldsymbol{q})$ to the spin-spiral eigenenergies or to use the old Fermi energy ε_F^0 of the spin-spiral system without SOC. In general the Fermi energies can shift considerable as indicated in the figure 2.14. While *ab-initio* calculations for Fe/W-systems exhibit, that the new recalculated Fermi energy is nearly the same as the old Fermi energy [9], the Fe/Pt-systems, which will be discussed in the applications of this thesis, show a non-negligible difference between the old or new Fermi energy.

For the more detailed discussion of SOC it is intuitive, to take a look at the total 1st-order SOC contribution to the total energy using the new or old Fermi energy:

(a) unchanged Fermi energy:

$$\begin{aligned}\Delta E_{SOC}(\boldsymbol{q}) &= \sum_{\boldsymbol{k},n} f(\varepsilon^0_{\boldsymbol{k},n}, \varepsilon^0_F) \cdot (\varepsilon^0_{\boldsymbol{k},n}(\boldsymbol{q}) + \Delta\varepsilon_{\boldsymbol{k},n}(\boldsymbol{q})) - \\ &\quad \sum_{\boldsymbol{k},n} f(\varepsilon^0_{\boldsymbol{k},n}, \varepsilon^0_F) \cdot \varepsilon^0_{\boldsymbol{k},n}(\boldsymbol{q}) \\ &= \sum_{\boldsymbol{k},n} f(\varepsilon^0_{\boldsymbol{k},n}, \varepsilon^0_F) \cdot \Delta\varepsilon_{\boldsymbol{k},n}(\boldsymbol{q}) \end{aligned} \tag{2.86}$$

It can be proven [24] that

$$\Delta\varepsilon_{\boldsymbol{k},n}(-\boldsymbol{q}) = -\Delta\varepsilon_{\boldsymbol{k},n}(\boldsymbol{q})\,. \tag{2.87}$$

On the other hand, for the eigenenergies of the spin-spiral system without SOC we have

$$\varepsilon^0_{\boldsymbol{k},n}(-\boldsymbol{q}) = \varepsilon^0_{\boldsymbol{k},n}(\boldsymbol{q}) \tag{2.88}$$

due to symmetry. Therefore the SOC-contribution fulfils the following relation:

$$\Delta E_{\mathrm{SOC}}(-\boldsymbol{q}) = -\Delta E_{\mathrm{SOC}}(\boldsymbol{q})\,. \tag{2.89}$$

It is also obvious that $\Delta E_{\mathrm{SOC}} \propto \xi_{\mathrm{SOC}}$, which can be seen in expression 2.85.

(b) recalculated Fermi energy:

$$\begin{aligned}\Delta E_{\mathrm{SOC}}(\boldsymbol{q}) &= \sum_{\boldsymbol{k},n} f(\varepsilon^0_{\boldsymbol{k},n} + \Delta\varepsilon_{\boldsymbol{k},n}(\boldsymbol{q}), \varepsilon_F) \cdot (\varepsilon^0_{\boldsymbol{k},n} + \Delta\varepsilon_{\boldsymbol{k},n}(\boldsymbol{q})) - \sum_{\boldsymbol{k},n} f(\varepsilon^0_{\boldsymbol{k},n}, \varepsilon^0_F) \cdot \varepsilon^0_{\boldsymbol{k},n} \\ &= \sum_{\boldsymbol{k},n} [f(\varepsilon^0_{\boldsymbol{k},n} + \Delta\varepsilon_{\boldsymbol{k},n}(\boldsymbol{q}), \varepsilon_F) - f(\varepsilon^0_{\boldsymbol{k},n}, \varepsilon^0_F)] \cdot \varepsilon^0_{\boldsymbol{k},n} + \\ &\quad \sum_{\boldsymbol{k},n} f(\varepsilon^0_{\boldsymbol{k},n} + \Delta\varepsilon_{\boldsymbol{k},n}(\boldsymbol{q}), \varepsilon_F) \cdot \Delta\varepsilon_{\boldsymbol{k},n}(\boldsymbol{q}) \\ &\approx \sum_{\boldsymbol{k},n} [f(\varepsilon^0_{\boldsymbol{k},n}, \varepsilon^0_F) \cdot \Delta\varepsilon_{\boldsymbol{k},n}(\boldsymbol{q}) + (\varepsilon^0_{\boldsymbol{k},n}(\boldsymbol{q}) + \Delta\varepsilon_{\boldsymbol{k},n}(\boldsymbol{q})) \cdot \\ &\quad (\frac{\partial f}{\partial \varepsilon^0_{\boldsymbol{k},n}} \cdot \Delta\varepsilon_{\boldsymbol{k},n}(\boldsymbol{q}) + \frac{\partial f}{\partial \varepsilon^0_F} \cdot (\varepsilon_F - \varepsilon^0_F))] \end{aligned} \tag{2.90}$$

It is obvious that the relation 2.89 is not any more valid. In the case of $\varepsilon_F \approx \varepsilon^0_F$ it is fulfilled to a good approximation and we can use the old Fermi energy without causing a significant error.

We should remark that treating SOC for spin-spirals in 1st-order perturbation theory does not allow to calculate the magneto-crystalline anisotropy energy (MCA) of the system. To treat also the MCA, one has to extend the mechanism to 2nd-order perturbation theory [24, 9], which is not implemented in the used tight-binding framework yet. Instead collinear SOC calculations are used to determine the MCA.

2.9 Force theorem

The self-consistent scheme of the tight-binding method (see figure 2.9) can require a lot of computational time for systems with many basis atoms. Especially for magnon dispersions, calculations for a large set of $\boldsymbol{q}$-values have to be performed. Fortunately one can spare a lot of computing time using the so-called force theorem [44, 45, 46].

The force theorem can be used in systems, where a small perturbation $\delta\mathcal{H}$ is added to a system $\mathcal{H}_0$, whose self-consistent solution is known:

$$\mathcal{H} = \mathcal{H}_0 + \delta\mathcal{H} \qquad \text{with} \qquad \underline{\boldsymbol{H_0}} \cdot \boldsymbol{\Psi}^0_{\boldsymbol{k},n} = \varepsilon^0_{\boldsymbol{k},n} \cdot \boldsymbol{\Psi}^0_{\boldsymbol{k},n} \,. \tag{2.91}$$

For the perturbed system only one iteration is done, which is also known as "one-shot-calculation". Of course this one-shot-calculation depends delicately on the starting values for the magnetic moments and Mulliken charges, therefore reasonable starting values are necessary. The charges and moments of the converged unperturbed problem should provide good starting values if the perturbation $\delta\mathcal{H}$ is small.

The force theorem can be expressed by the following relation:

$$\begin{aligned} E_{\text{tot}} - E^0_{\text{tot}} &= E_{\text{band}} - E^0_{\text{band}} \\ &= \sum_{\boldsymbol{k},n} f(\varepsilon_{\boldsymbol{k},n}, \varepsilon_F) \cdot \varepsilon_{\boldsymbol{k},n} - \sum_{\boldsymbol{k},n} f(\varepsilon^0_{\boldsymbol{k},n}, \varepsilon^0_F) \cdot \varepsilon^0_{\boldsymbol{k},n} \,, \end{aligned} \tag{2.92}$$

where E_{band} is the band energy of the perturbed system, E^0_{band} is the band energy of the unperturbed system and E_{tot} is the total energy of the perturbed system for a self-consistent calculation (including double counting terms). Within the force theorem the difference of the single particle energies is taken as approximation for the difference of the total energies.

In the treatment of spin-spirals a self-consistent calculation for $\boldsymbol{q} = 0$ (ferromagnetic case) is performed and the converged charges and moments are used as starting-values for a one-shot-calculation for $\boldsymbol{q} \neq 0$.

To ensure that the force theorem is a proper approximation, in this case the spin-spiral for $\boldsymbol{q} \neq 0$ has to be only slightly different in comparison to the $\boldsymbol{q} = 0$-case. This is definitely true for small cone angles Θ and small q-values, but the validity for larger cone-angles and larger q-values is examined in chapter 3 and 5.

2.10 Extended Heisenberg model

It is common to use a model-Hamiltonian to describe the magnetic interactions in a (periodic) system. In the following sections the extended Heisenberg model is described in detail [5].

In the extended Heisenberg model the following assumptions are taken into account:

- The magnetic moment of each atom is described by a localized (classical) spin-vector $\boldsymbol{S}_i$ at the corresponding lattice position.

- The magnetic moment has a fixed absolute value, i.e. the absolute value of the magnetic moment does not change with the q-value, which is an approximation for larger cone-angles Θ in the spin-spiral case.

The extended Heisenberg model can be written as generalized scalar-product of spins:

$$\mathcal{H}_{\text{ex.Heisenberg}} = -\sum_{i,j} \boldsymbol{S}_i^T \cdot \underline{\boldsymbol{V}}_{ij} \cdot \boldsymbol{S}_j \,. \tag{2.93}$$

Here, $\underline{\boldsymbol{V}}_{ij}$ is a 3×3 matrix, which can be divided into a symmetric and an antisymmetric part, $\underline{\boldsymbol{V}}_{ij}^S$ and $\underline{\boldsymbol{V}}_{ij}^A$:

$$\underline{\boldsymbol{V}}_{ij} = \frac{1}{2}(\underline{\boldsymbol{V}}_{ij} + \underline{\boldsymbol{V}}_{ij}^T) + \frac{1}{2}(\underline{\boldsymbol{V}}_{ij} - \underline{\boldsymbol{V}}_{ij}^T) = \underline{\boldsymbol{V}}_{ij}^S + \underline{\boldsymbol{V}}_{ij}^A \,. \tag{2.94}$$

It is common to divide the symmetric matrix $\underline{\boldsymbol{V}}_{ij}^S$ into a traceless part and an isotropic exchange part:

$$\underline{\boldsymbol{V}}_{ij}^S = [\underline{\boldsymbol{V}}_{ij}^S - J_{ij} \cdot \underline{\boldsymbol{I}}] + J_{ij} \cdot \underline{\boldsymbol{I}} \,, \tag{2.95}$$

with

$$J_{ij} = \frac{1}{3} \cdot tr[\underline{\boldsymbol{V}}_{ij}^S] \,. \tag{2.96}$$

The antisymmetric part can be expressed using a cross-product:

$$\boldsymbol{S}_i^T \cdot \underline{\boldsymbol{V}}_{ij}^A \cdot \boldsymbol{S}_j = \boldsymbol{D}_{ij} \cdot (\boldsymbol{S}_i \times \boldsymbol{S}_j) \,, \tag{2.97}$$

where

$$[\underline{\boldsymbol{V}}_{ij}^A]_{nn'} = \sum_l [\boldsymbol{D}_{ij}]_l \cdot \epsilon_{lnn'} \,. \tag{2.98}$$

Here, $\epsilon_{lnn'}$ is the Levi-Civita tensor.

Summarizing the extended Heisenberg model consist of the following parts:

$$\begin{aligned} \mathcal{H}_{\text{ex.Heisenberg}} \;=\; -\sum_{i,j}[& \underbrace{J_{ij} \cdot \boldsymbol{S}_i^T \cdot \boldsymbol{S}_j}_{\text{symmetric isotropic exchange}} + \underbrace{\boldsymbol{S}_i^T \cdot (\underline{\boldsymbol{V}}_{ij}^S - J_{ij} \cdot \underline{\boldsymbol{I}}) \cdot \boldsymbol{S}_j}_{\text{symmetric anisotropic exchange}} + \\ & \underbrace{\boldsymbol{D}_{ij} \cdot (\boldsymbol{S}_i \times \boldsymbol{S}_j)}_{\text{Dzyaloshinskii}-\text{Moriya interaction}}] \,. \end{aligned} \tag{2.99}$$

In many cases the symmetric anisotropic exchange part is neglected except for the diagonal part

$$\boldsymbol{S}_i^T \cdot (\underline{\boldsymbol{V}}_{ij}^S - J_{ij} \cdot \underline{\boldsymbol{I}}) \cdot \boldsymbol{S}_j \approx \boldsymbol{S}_i^T \cdot \underline{\boldsymbol{K}}_i \cdot \boldsymbol{S}_i \cdot \delta_{ij} \,, \tag{2.100}$$

which describes the magneto-crystalline anisotropy (MCA) of the system with the MCA-matrix $\underline{\boldsymbol{K}}_i$.

2.10.1 Symmetric isotropic exchange

This part is the well-known Heisenberg exchange, which describes a ferromagnetic ($J_{ij} > 0$) or anti-ferromagnetic ($J_{ij} < 0$) coupling between the spins $\boldsymbol{S}_i$ and $\boldsymbol{S}_j$. If one considers only next-neighbour coupling a collinear alignment of the spins would be the ground-state solution. In general, it can be proven that a solution of the Heisenberg Hamiltonian in a periodic system is a spin-spiral. For a spin-spiral with a cone-angle Θ, spiral-vector $\boldsymbol{q}$ and the z-axis as the rotation axis, the Heisenberg model can be rewritten in the following way using

$$\boldsymbol{S}_i = \begin{pmatrix} \cos(\boldsymbol{q}\cdot\boldsymbol{R}_n)\cdot\sin\Theta \\ \sin(\boldsymbol{q}\cdot\boldsymbol{R}_n)\cdot\sin\Theta \\ \cos\Theta \end{pmatrix} \quad :$$

$$-\sum_m \sum_{n\in\text{shell}(m)} J_m \cdot \boldsymbol{S}_0 \cdot \boldsymbol{S}_n = -\sum_m \sum_{n\in\text{shell}(m)} J_m \cdot \left[\cos^2\Theta + \sin^2\Theta\cdot\cos(\boldsymbol{q}\cdot\boldsymbol{R}_n)\right]. \quad (2.101)$$

Here a shell is a set of atoms, which have the same fixed distance from the reference atom. For example shell(1) includes all nearest neighbours of the reference atom. If one calculates the magnon dispersion $E(\boldsymbol{q})$, the Heisenberg exchange-coupling parameters J_n can be determined via the following equation:

$$\frac{1}{\sin^2\Theta}\cdot\left[E(\boldsymbol{q}) - E(0)\right] = -\sum_m \sum_{n\in\text{shell}(m)} J_m \cdot \left[\cos(\boldsymbol{q}\cdot\boldsymbol{R}_n) - 1\right]. \quad (2.102)$$

The coupling parameters can be calculated via a fitting procedure to quantum-mechanical results of the energy $E(\boldsymbol{q})$.

An important quantity is the so-called spin-stiffness constant A, which describes the pre-factor of the quadratic q-dependence in the magnon dispersion for very long-wavelength spin-spirals, i.e. very small q-values. This quadratic q-dependence can be easily seen from eq. 2.102 due to $(1-\cos(\boldsymbol{q}\cdot\boldsymbol{R}_n)) \approx (\boldsymbol{q}\cdot\boldsymbol{R}^n)^2$ for small q.

2.10.2 Dzyaloshinskii-Moriya interaction

The antisymmetric exchange part in the extended Heisenberg model is also known as Dzyaloshinskii-Moriya interaction (DMI) [3, 4]. In contrast to the symmetric exchange part the energies of the antisymmetric exchange part are in general different for different rotational senses of the spin-spirals. This can be easily seen by rewriting the antisymmetric part of the Hamiltonian as follows:

$$\begin{aligned} E_{\text{DM}} &= -\sum_m \sum_{n\in\text{shell}(m)} \boldsymbol{D}_m \cdot (\boldsymbol{S}_0 \times \boldsymbol{S}_n) \\ &= -\sum_m \sum_{n\in\text{shell}(m)} \boldsymbol{D}_m \cdot \begin{pmatrix} -\sin\Theta\cdot\cos\Theta\cdot\sin(\boldsymbol{q}\cdot\boldsymbol{R}_n) \\ \sin\Theta\cdot\cos\Theta\cdot(\cos(\boldsymbol{q}\cdot\boldsymbol{R}_n)-1) \\ \sin^2\Theta\cdot\sin(\boldsymbol{q}\cdot\boldsymbol{R}_n) \end{pmatrix}. \end{aligned} \quad (2.103)$$

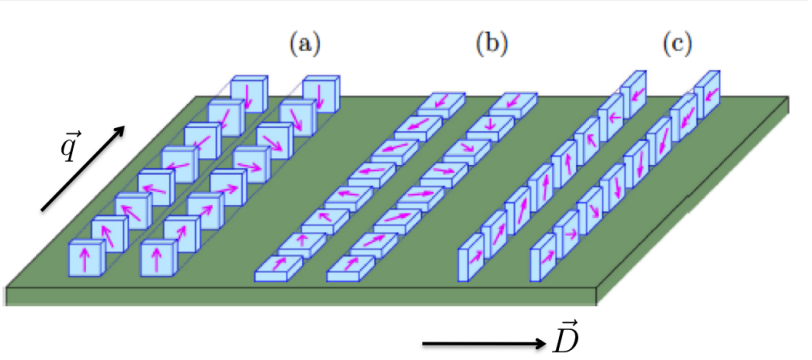

Figure 2.15: Different spin-spirals on an isotropic surface. Each case (a), (b) and (c) is explained in the text. | modified fig. from [8]

In the special case of flat-spirals ($\Theta = \frac{\pi}{2}$), the equation simplifies to

$$E_{\mathrm{DM}}(\boldsymbol{q}) = -\sum_{m} \sum_{n \in \mathrm{shell}(m)} (\boldsymbol{D}_m)_z \cdot \sin(\boldsymbol{q} \cdot \boldsymbol{R}_n)\,. \tag{2.104}$$

From this expression it becomes clear that $E_{\mathrm{DM}}(-\boldsymbol{q}) = -E_{\mathrm{DM}}(\boldsymbol{q})$. Of course the expression for the DMI would be of an analogous form for flat-spirals in the x-z or y-z plane.

In many cases only the first neighbour shell is considered for the DMI, therefore the DM-constant $D := D_1$ is determined via a linear fit to the magnon dispersion for small q-values for which $\sin(\boldsymbol{q} \cdot \boldsymbol{R}_n) \approx \boldsymbol{q} \cdot \boldsymbol{R}^n$ is valid.

Crucial for the appearance of the DMI is the presence of SOC and a non-inversion-symmetric environment. Both requirements are needed, otherwise, the energy of a spin-spiral is independent of the rotational sense due to symmetry arguments, i.e. $E_{\mathrm{DM}} = 0$. As a deep understanding of the symmetry arguments is crucial for further analyse, we provide a more detailed explanation.

If SOC is not considered, real-space and spin-space would be independent and a global spin-transformation would not change the energy of the system. Now there exists a mirror-transformation applied to a flat-spiral leads to the reversion of its rotation sense. This mirror-plane is the plane, which is spanned by the spiral vector $\boldsymbol{q}$ and the rotation axis of the spin-spiral. Since a global spin-transformation does not change the energy in the system without SOC, it holds $E_{\mathrm{DM}}(-\boldsymbol{q}) = E_{\mathrm{DM}}(\boldsymbol{q}) = -E_{\mathrm{DM}}(\boldsymbol{q}) = 0$.

The argument for a non-inversion-symmetric environment as requirement for non-vanishing DMI is a little bit more complicated to understand, because the type of spin-spiral plays also an important role. Figure 2.15 should help with the explanation. Here, flat spin-spirals on a surface are displayed. In each case (a), (b) and (c) two spin-spirals with equal $|\boldsymbol{q}|$ but opposite rotational sense are shown. The only difference among (a), (b) and (c) is the rotation axis. In the cases (a) and (b) there is a preserved mirror-plane, which leads to vanishing DMI. In the case (c) there is no mirror-plane due

to the symmetry-breaking effect of the surface, which leads to a non-vanishing DMI-contribution. These statements correspond to the case of an isotropic surface. For more details about the symmetry of the DMI for more general systems the reader is referred to reference [47].

2.10.3 Symmetric anisotropic exchange

As already mentioned in the extended Heisenberg model only the diagonal part of the symmetric anisotropic exchange is considered, which can be identified as MCA. The MCA is important to investigate the occurence of spin-spirals due to DMI, because eventually the MCA can inhibit the development of a spin-spiral. For example if the system in figure 2.15(c) has an easy axis perpendicular to the plane of the spin-spiral and the MCA is strong enough, the system could favour a collinear alignment along the easy axis over the spin-spiral structure even in the presence of DMI.

The stability of spin-spirals can be most easily investigated with a micromagnetic model [48, 49]. Without going into details, we note that relations between the spin-stiffness constant A, the DM-constant D and the MCA give a stability condition for the development of a spin-spiral in the system. The micromagnetic model is based on a continuum-theoretical approach for long-wavelength spin-spirals, which leads to the following equation for the energy E of the spin-spiral in dependence of the spin-spiral period length λ:

$$E(\lambda) = A \cdot \lambda^{-2} + D \cdot \lambda^{-1} + \bar{K} \,. \tag{2.105}$$

The derivation of the spin-stiffness constant A and the DM-constant D with the help of the magnon dispersion $E(\boldsymbol{q})$, is explained in section 2.10.1 and 2.10.2. The connection to eq. 2.105 can be easily seen by using $|\boldsymbol{q}| \propto \lambda^{-1}$ in eq. 2.102 and 2.104 for small q-values. The constant $\bar{K}$ describes the average MCA over an entire period of the spin-spiral. In section 5.3 the constants A and D are derived for Fe/Pt(001) layers.

3 Pure Fe-Systems

3.1 Introduction

Pure Fe-systems are well suited for comparing the results of the TB-calculations with *ab-initio* results. Systems like bcc-Fe, Fe monolayers and Fe chains do not need a large amount of computational time and their simplicity allows for a deeper understanding of the physics behind our tight-binding scheme. Although the systems are simple, the whole physics behind the tight-binding Hamiltonian

$$\mathcal{H} = \mathcal{H}_0 + \mathcal{H}_{\text{mag}} + \mathcal{H}_{\text{LCN}} + \mathcal{H}_{\text{SOC}} \tag{3.1}$$

can be tested.

The quality of the Slater-Koster parametrization is examined by comparing non-magnetic bcc-Fe calculations with corresponding *ab-initio* results (see section 3.2). There, the splitting in the band structure due to SOC enables a possibility to test the accuracy of the SOC-parameters ξ_μ^{Fe}. The magnetic part of the Hamiltonian, described via the Stoner model, predicts magnetic moments of the Fe-systems, which are compared to *ab-initio* values (see section 3.3 and 3.4). To test the local charge neutrality part of $\mathcal{H}$, $\mathcal{H}_{\text{LCN}}$, a system with non-equivalent basis atoms has to be examined. Here, a multilayer system of Fe atoms gives us the opportunity to examine the charge transfer to the surface (see section 3.4).

Interesting properties can be observed in the calculation of spin-spirals in Fe-systems. In section 3.4 an indication for the Bethe-Slater behaviour [50, 51, 52, 53] in Fe chains is presented. In section 3.3 the Heisenberg exchange-coupling parameters $J_{nn'}$ for bcc-Fe are compared to *ab-initio* results. Finally, the magneto-crystalline anisotropy energy (MCA) is calculated for different systems such as an Fe chain and Fe monolayers of different crystallographic orientations (see section 3.4).

3.2 Quality of the Slater-Koster parametrization

The parametrization of the hopping elements and on-site energies is explained in detail in section 2.3. The parameters $a_{ll'm}$, $b_{ll'm}$, $c_{ll'm}$ and $d_{ll'm}$ of eq. 2.21 and the on-site parameters α, β, γ, δ and λ of eq. 2.23 for Fe can be found in the appendix in the tables B.1 and B.2. There exists a parameter set for Fe, which is obtained from LDA *ab-initio* calculations [15, 16] and one obtained from GGA *ab-initio* calculations [54, 16]. Experience shows that $3d$-transition metals are usually better described within GGA, therefore the GGA-parameter set for Fe is used in this thesis, unless differently indicated.

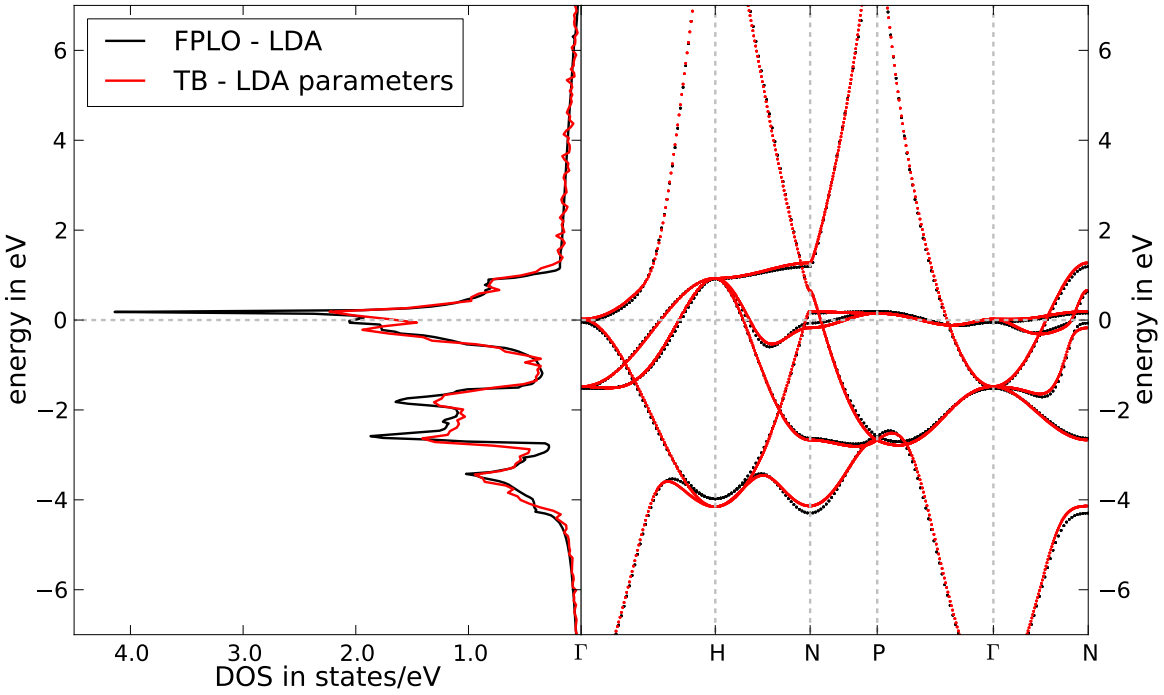

Figure 3.1: Non-magnetic band structure and DOS of bcc-Fe for the LDA case. The black curve is an FPLO-calculation [55] and the red one a TB-calculation with the LDA parameter set.

In figure 3.1 and 3.2 the band structure of non-magnetic bcc-Fe without SOC at the experimental equilibrium lattice parameter $a = 2.87\,\text{Å}$ is displayed along high-symmetry directions in the Brillouin zone. We investigate the band structure of non-magnetic bcc-Fe to evaluate the quality of the paramagnetic Fe parameter sets, while magnetic calculations would include the Stoner model as an approximate method to describe magnetism. In figure 3.1 the band structure from a tight-binding calculation with the LDA parameter set is compared to LDA *ab-initio* calculations[1] [55], whereas in figure 3.2 the GGA parameter set is compared to the GGA *ab-initio* results[2] [56]. For the TB-calculations of bcc-Fe in the sections 3.2 and 3.3 64000 k-points in the full Brillouin zone were used. The width of the lorentzian functions in the DOS calculation is 50 meV.

Both TB-parameter sets are in a good agreement with the *ab-initio* results. This can be observed in the density of states (DOS), which is presented in the left panel of figure 3.1 and 3.2. The TB-scheme does not reproduce the very sharp peak just above the Fermi energy $\varepsilon_F = 0$, due to the slightly stronger dispersion of the bands in this region, especially for the GGA case. Therefore one can expect a difference in the description of physical properties of Fe, which have a very sensitive dependence on the Fermi surface.

[1] Calculation was performed by H. Zhang with an FPLO-code using following computational parameters: $N_k = 1728$. The basis set consisted of $3s$, $3p$, $3d$, $4s$, $4p$, $4d$, $5s$ orbitals.

[2] Calculation was performed by H. Zhang with the FLEUR-code using following computational parameters: $N_k = 8000$, $R_{\text{max}} = 2.28\,\text{a.u.}$, $k_{\text{max}} = 3.4\,\text{a.u.}^{-1}$, $l_{\text{max}} = 6$.

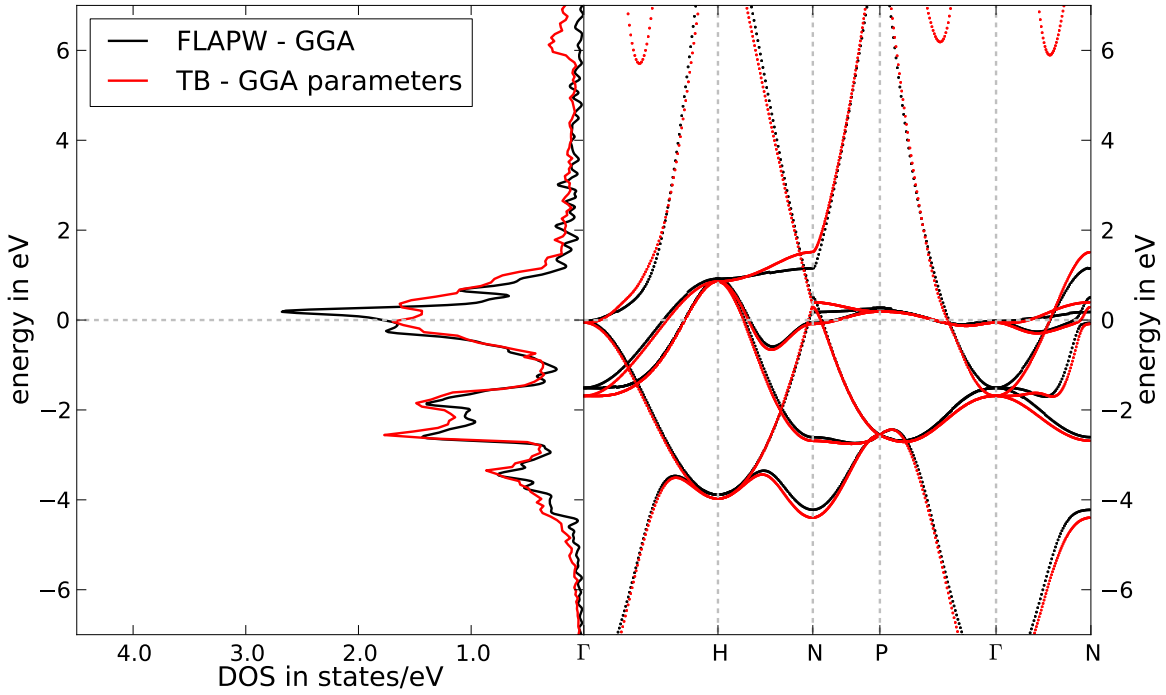

Figure 3.2: Non-magnetic band structure and DOS of bcc-Fe for the GGA case. The black curve is an FLAPW-calculation [56] and the red one a TB-calculation with the GGA parameter set.

The band structures are only compared in a region of a few eV around the Fermi energy. In this region a proper description of the electronic structure is necessary to expect reasonable results for more complex magnetic structures than bcc-Fe. The conduction bands far away from ε_F are not properly described with the parameter sets. This does not constitute a considerable problem, since these conduction bands hardly influence the valence electron properties.

The following SOC-parameters, used in [26, 25], lead to a reasonable description of SOC in Fe-systems:

$$\xi_d^{\mathrm{Fe}} = 0.06\,\mathrm{eV} \quad \text{and} \quad \xi_p^{\mathrm{Fe}} = 0.18\,\mathrm{eV}\,. \tag{3.2}$$

To test the quality of these parameters, a non-magnetic TB-calculation including SOC was performed and it was compared to a corresponding *ab-initio* calculation. In the left panel of figure 3.3 a zoom into the region 1.5 meV below ε_F of the band structure around the Γ-point is displayed. Both band structures in the left panel of fig. 3.3 are calculated with the LDA parameter set in a tight-binding scheme, but in one case a calculation without SOC and in the other case a calculation with SOC was performed.

One can clearly observe the splitting of the degenerate bands at the Γ-point into a two-fold degenerate band and a single split-off band due to SOC. In the right panel of figure 3.3 the splitting obtained by a tight-binding calculation is compared to the splitting obtained by an *ab-initio* LDA calculation. The splitting of about 90 meV is observed in both cases, therefore ξ_d^{Fe} and ξ_p^{Fe} are reasonable values to model SOC in Fe.

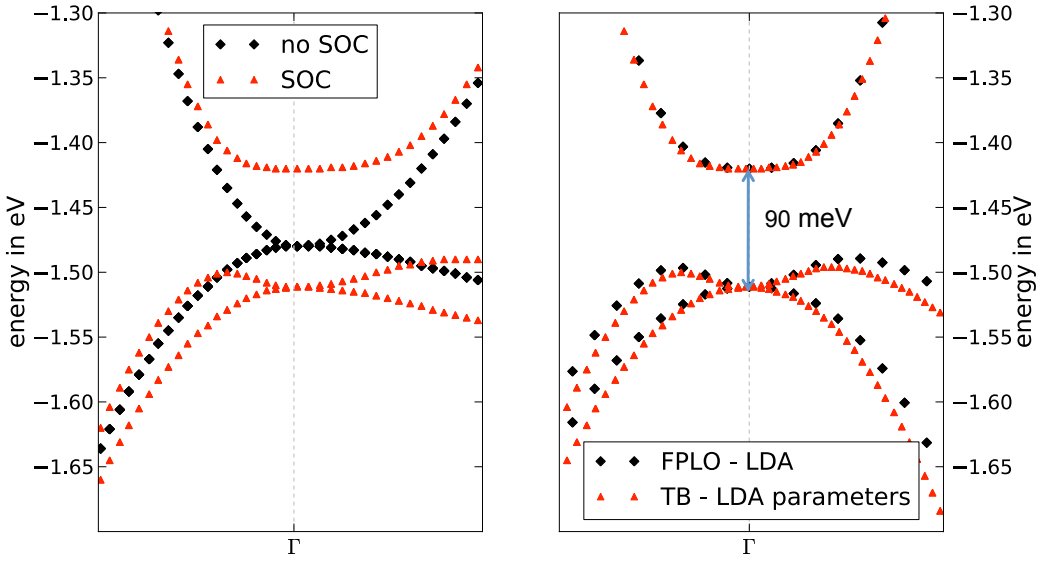

Figure 3.3: Left Panel: Splitting of the bands at the Γ-point due to SOC in non-magnetic bcc-Fe in a TB-calculation. The black curve is the band structure without SOC, whereas the red curve is the band structure with SOC. The splitting is about 90 meV. Right panel: Splitting of the bands at the Γ-point due to SOC. The black curve is the band structure for an FPLO-calculation and the red one for a TB-calculation.

The spin-orbit coupling parameter of the p-bands ξ_p^{Fe} plays a minor role, because mainly the d-bands have an influence close to the Fermi energy. We have chosen a reasonable value for the p-SOC-parameter by setting it three times larger than the SOC-parameter for the d-orbitals, but in principle this value can be varied without changing noticeably the band structure close to the Fermi energy.

3.3 Magnetism via Stoner model in bcc-Fe

A Stoner model is used to model magnetism in the tight-binding framework. The detailed theory about this can be found in section 2.6 of the present thesis. We use the following Stoner parameters for Fe:

$$I_d^{\mathrm{Fe}} = 0.96\,\mathrm{eV} \quad \text{and} \quad I_s^{\mathrm{Fe}} = I_p^{\mathrm{Fe}} = \frac{I_d^{\mathrm{Fe}}}{10}\,. \tag{3.3}$$

In [26, 25] these Stoner parameters provide a good description of magnetism in Fe. As one can see from the following calculations, we also find that these Stoner parameters lead to reasonable results. The Stoner model is of course only an approximate method to describe the magnetic interaction of the band electrons. Therefore one should compare

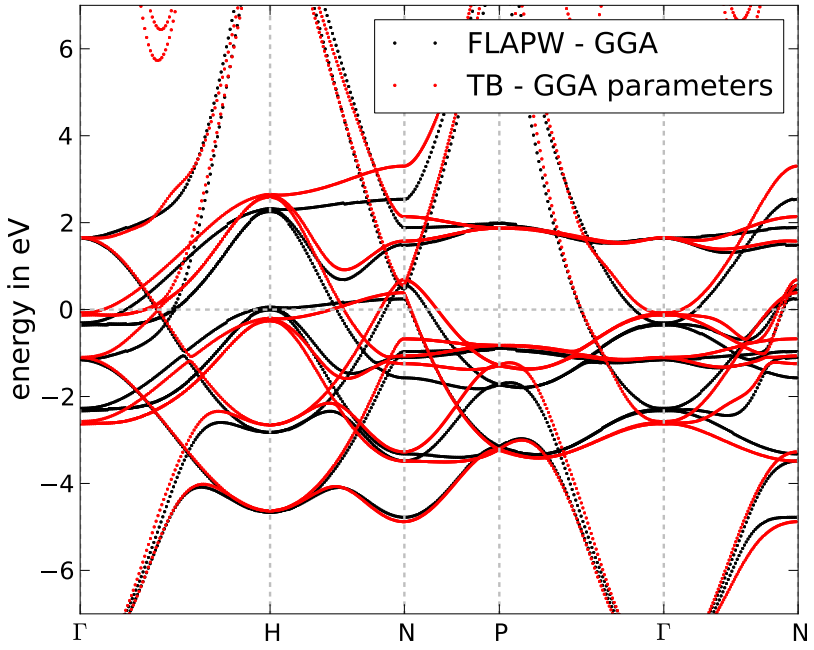

Figure 3.4: Band structure of ferromagnetic bcc-Fe including SOC within tight-binding (red) and FLAPW (black). In the TB-calculation a Stoner model is used to model magnetism.

the band structure and the corresponding magnetic moment of Fe with *ab-initio* results[3], presented in figure 3.4.

Overall the tight-binding calculation for bcc-Fe corresponds well to the *ab-initio* results. There are some differences near the Fermi energy, which prevent a quantitative good description of physical properties, sensitive to an accurate description of the Fermi surface (e.g. conductivities, MCA etc.). This can be also observed in the orbital-resolved and spin-resolved DOS in figure 3.5. The magnetic moment of the Fe-atom is $2.30\,\mu_B$ in the *ab-initio* calculation and $2.34\,\mu_B$ in the TB-calculation, which for our purposes constitutes a very good agreement. We are interested in a qualitatively reasonable description of Fe in Fe/Pt-systems (see chapter 5) or Fe in systems beyond bcc-Fe. Therefore the accuracy of the band structure via the tight-binding parametrization is sufficient, as we shall demonstrate.

Further evidence of the good quality of the TB-description can be found by examining the spin-spiral spectrum of bcc-Fe. The magnon dispersion $E(\boldsymbol{q})$ is calculated via the force theorem (see chapter 2.9) for a spin-spiral with a cone angle $\Theta = 30°$ along high-symmetry directions in the Brillouin zone. The result is compared to a corresponding *ab-initio* calculation[4] in figure 3.6. With an exception of the dispersion of larger q-values

[3]Calculation was performed by H. Zhang with the FLEUR-code [56] using following computational parameters: $N_k = 8000$, $R_{\max} = 2.28\,\text{a.u.}$, $k_{\max} = 3.4\,\text{a.u.}^{-1}$, $l_{\max} = 6$.

[4]Calculation was performed by A. Jakobsson with the FLEUR-code [56]. The J_{ij}-calculation was

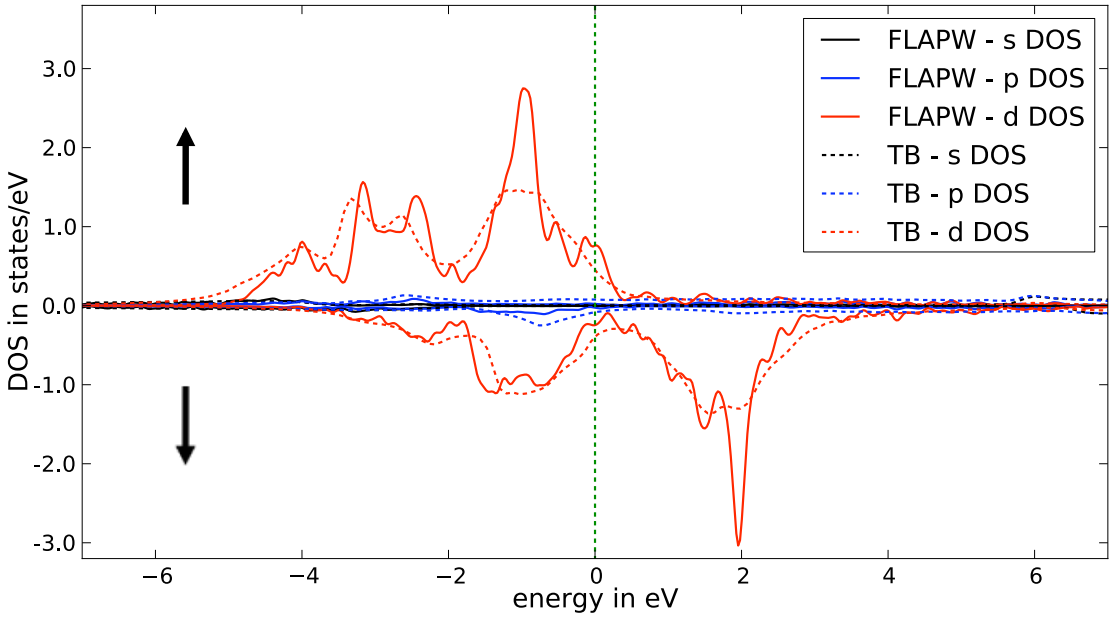

Figure 3.5: Spin-resolved and orbital-resolved DOS of ferromagnetic bcc-Fe corresponding to figure 3.4. The result of FLAPW (solid lines) is compared to the TB result (dashed lines).

the results are in good agreement. Also, the Heisenberg exchange-coupling parameters J_n in figure 3.6 show overall a good agreement, although the J_n-values for the first two shells are overestimated in tight-binding.

An important detail which should be discussed is the validity of the force theorem for different cone angles. In figure 3.7 force theorem calculations for different Θ-angles are compared to self-consistent calculations. In general the magnetic moment depends on the q-values, therefore the force theorem is an approximation. But as one can see in figure 3.7, the force theorem is a reasonable approximation in particular for smaller cone angles and small q-values for which the magnetic moment hardly differs compared to the ferromagnetic case. Thus, by default the force theorem will be used for all spin-spiral calculations in this thesis, unless differently indicated.

3.4 Transferability of the tight-binding parameters

In this section we take a look at the magnetism in Fe monolayers and Fe chains. The same parameter sets as for bcc-Fe are used, therefore we test the transferability of this parametrization as mentioned in chapter 2.3.

performed by D. Bauer.

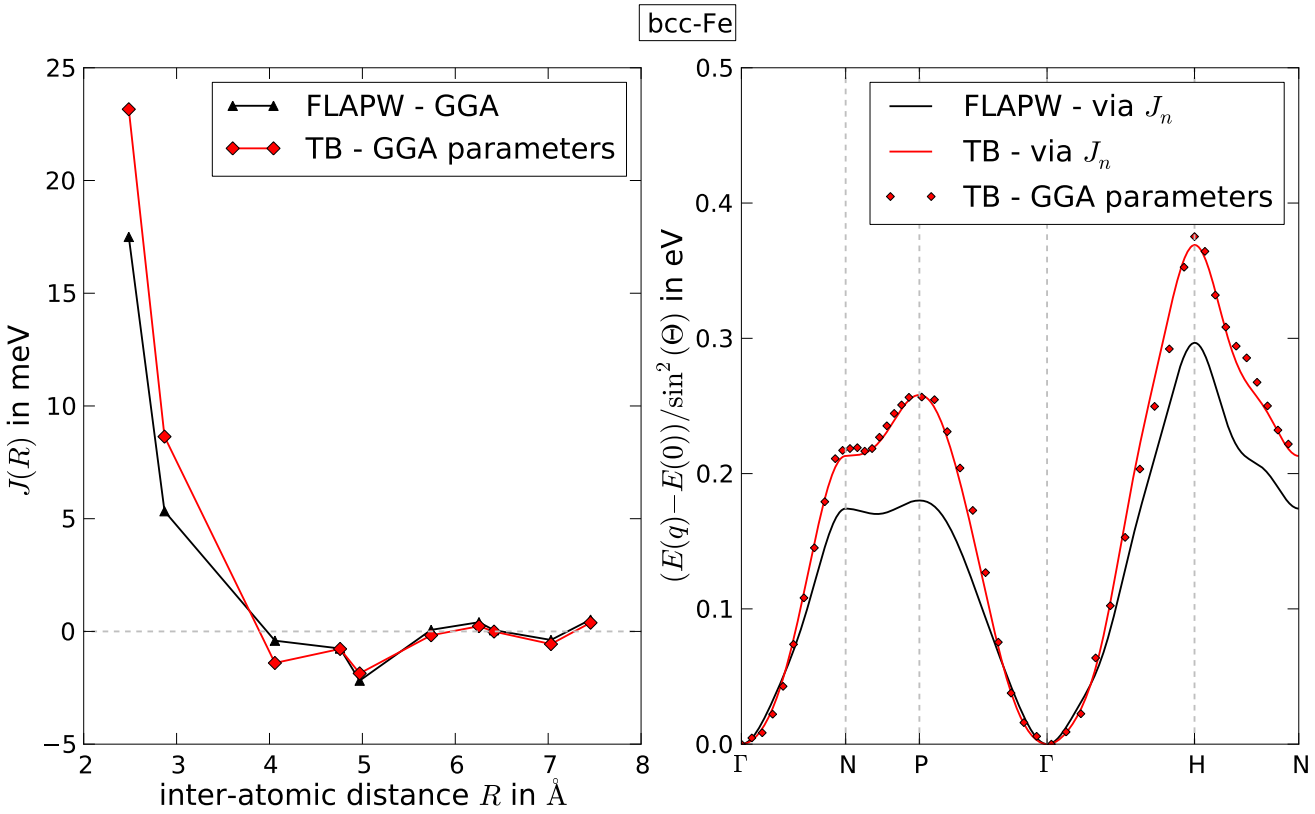

Figure 3.6: Left panel: Heisenberg exchange coupling parameters J_n of bcc-Fe derived by least square fit using $E(\boldsymbol{q})$ of a $\Theta = 30°$ spin-spiral for 47 $\boldsymbol{q}$-values in the irreducible part of the Brillouin zone (see eq. 2.102). The black curve is the result of an FLAPW-calculation and the red curve is the result of a TB-calculation. Right panel: Magnon dispersion along high-symmetry directions of bcc-Fe. The solid lines display the reconstructed magnon dispersion from the Heisenberg exchange constants, see left panel, whereas the dots are calculated within the force theorem by the TB-code.

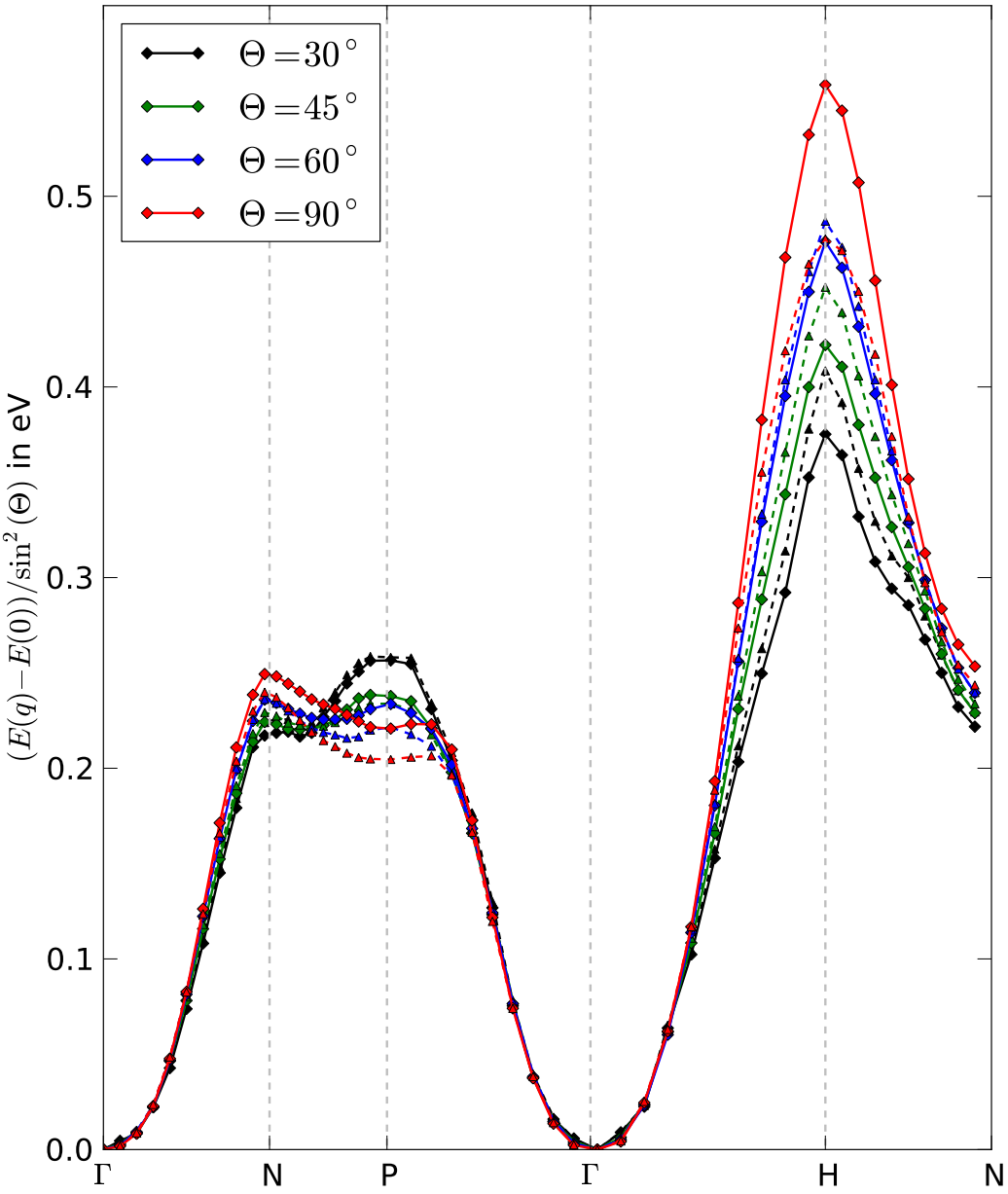

Figure 3.7: Magnon dispersion of bcc-Fe calculated with TB, where the solid lines are the results using the force theorem and the dashed lines are the self-consistent results. The calculations were performed for four different cone angles Θ.

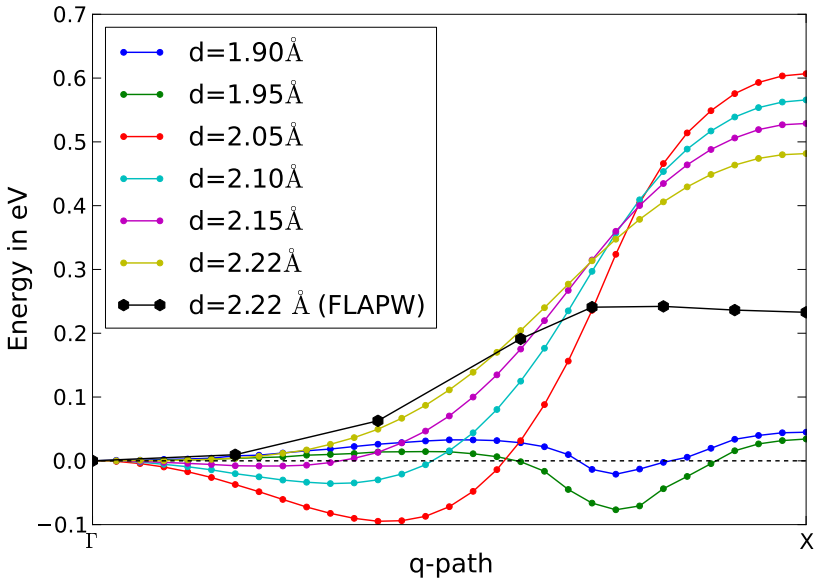

Figure 3.8: Magnon dispersion of an Fe chain for different lattice parameters a. The hexagons are values for the magnon dispersion of the Fe chain with $a = 2.22$ Å calculated with an FLAPW method [57].

3.4.1 Free-standing Fe chain

First we investigate magnetism in Fe mono-atomic chains depending on the lattice parameter a.[5] For the calculations 200 k-points in the full Brillouin zone were used. In figure 3.8 the magnon dispersion of a spin-spiral in a mono-atomic chain is displayed for several lattice parameters a of the chain. Decreasing the lattice parameter below the equilibrium value of about 2.22 Å leads to the tendency of forming a spin-spiral as magnetic ground state. This behaviour is consistent with the Bethe-Slater curve [50, 51, 52, 53]. This curve builds up a dependence of the exchange-integral J on the distance between the atoms. For the Fe chain, with the equilibrium lattice parameter $a = 2.22$ Å, the value of J is positive, therefore the Fe chain tends to a ferromagnetic structure. But J is not very large [53], therefore a slight decrease of the lattice parameter leads to a situation, where the ferromagnetic and anti-ferromagnetic structure have almost the same energy. In this case, it is known that the system tends to form a spin-spiral as ground state.

This tendency is well described via the tight-binding scheme, but one should note, that the used parameter set has been fitted to bulk bcc-Fe properties. Therefore it is not ideal to describe hoppings in the Fe chain. This problem, also known as the transferability problem, can be seen by comparing the magnon dispersion for $a = 2.22$ Å with the magnon dispersion for $a = 2.22$ Å calculated via FLAPW[6]. Therefore the TB-scheme

[5] Here the LDA-parameter set is used.

[6] Calculation was performed by F. Schubert with the FLEUR-code [56] using following computational

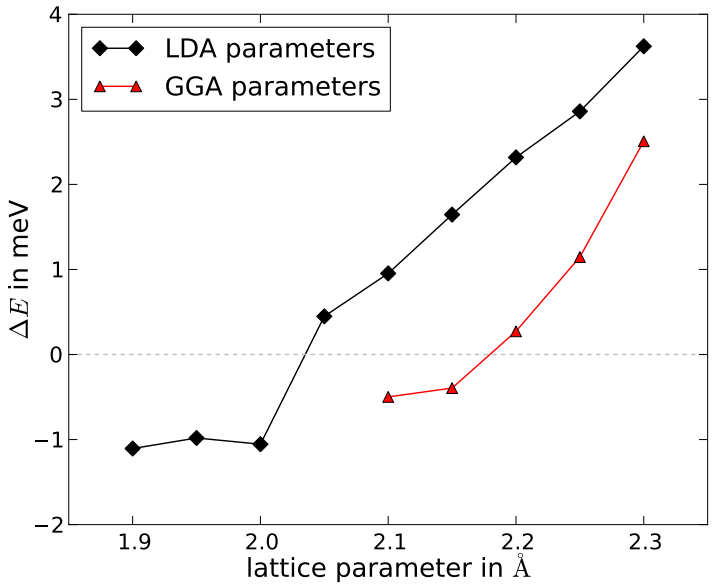

Figure 3.9: MCA $\Delta E = E_z - E_x$ of the Fe chain depending on the lattice parameter. The red curve corresponds to the values obtained with the GGA-parameter set, whereas the black curve was obtained with the LDA-parameter set. E_z is the total energy of the Fe chain with the magnetization perpendicular to the chain, whereas E_x is the energy along the chain.

only gives us the possibility to describe the qualitative tendencies for Fe-systems, which are geometrically very different compared to bcc-Fe.

Another interesting tendency is the dependence of the MCA of Fe chains on the lattice constant, which is shown in figure 3.9. In this case tight-binding calculations were performed with the LDA- and GGA-parameter set. Both parameter sets predict the same qualitative behaviour for the MCA, but the values differ considerably. Furthermore the magnetic moment of the Fe-atom rapidly drops to zero for lattice parameters under 2.1 Å in the GGA-case, whereas in the LDA-case it drops from large values about $3\,\mu_B$ to moderate values about $1\,\mu_B$. Therefore we can again observe transferability problems for the parameter sets. The qualitative tendency, that the Fe chain tends to an in-chain magnetization for larger lattice parameters remains the same for the parameter sets. The results for the LDA-parameter are also analysed in more detail in [25]. It should be noticed, that no dipole-dipole interaction is taken into account for all MCA-calculations within tight-binding in this work.

parameters: $N_k = 128$, $R_{\max} = 2.1\,\text{a.u.}$, $k_{\max} = 4.2\,\text{a.u.}^{-1}$, $l_{\max} = 8$.

		tight-binding				*ab-initio*			
	d	E_{MCA}	m^{Mull}	$L_{\uparrow}^{\mathrm{Mull}}$	$L_{\rightarrow}^{\mathrm{Mull}}$	E_{MCA}	m^{Mull}	$L_{\uparrow}^{\mathrm{Mull}}$	$L_{\rightarrow}^{\mathrm{Mull}}$
(001)	2.87	1.3	3.50	0.18	0.13	0.69	3.19	0.14	0.11
(110)	2.49	0.8	3.03	0.10	0.10	0.60	2.92	0.07	0.07
(111)	4.06	5.8	3.99	0.63	0.32	1.15	3.53	0.33	0.26

Table 3.1: The table shows the MCA $E_{\mathrm{MCA}} = E_{\rightarrow} - E_{\uparrow}$ (in meV) for Fe monolayers of different orientations with nearest neighbour distance d (in Å) calculated within tight-binding and within *ab-initio*. There $E_{\uparrow}$ is the total energy for an out-of-plane magnetization and $E_{\rightarrow}$ is the total energy for the in-plane magnetization along the x-axis. The magnetic (Mulliken-) moment m^{Mull} and the orbital moments for out-of-plane magnetization $L_{\uparrow}^{\mathrm{Mull}}$ and in-plane magnetization $L_{\rightarrow}^{\mathrm{Mull}}$ are also shown. They are all given in units of μ_B. The magnetic moment does not change significantly upon changing the magnetic direction.

3.4.2 Free-standing Fe monolayer and Fe slab

Next we investigate the MCA of free-standing Fe monolayers of different orientations and compare the values to *ab-initio* results[7]. In table 3.1 the MCA of a (001)-, a (110)- and a (111)-monolayer of Fe is presented together with the magnetic and orbital moments. For this calculation 40000 k-points in the full Brillouin zone were used, which is enough to ensure an accuracy of about 0.1 meV for the MCA. The convergence with respect to the number of k-points is presented in the appendix in B.2.

If we compare the MCA of the TB-calculation with the values obtained from *ab-initio*, we conclude that the TB-values overestimate the MCA, but in all cases an out-of-plane magnetization is the favourable one. The results for the (111)-monolayer are surprising, because the MCA is unexpectedly large and the magnetic moment is nearly of the atomic value of $4\,\mu_B$. The (111)-surface has the largest nearest neighbour distance of all three orientations, which is about 4.06 Å. Therefore in the TB-calculation the system shows tendencies of free Fe atoms due to the exponential behaviour of the distance parametrization for the hopping elements. But overall the tendencies are described well within the tight-binding scheme.

Finally, the local charge neutrality part $\mathcal{H}_{\mathrm{LCN}}$ of the Hamiltonian should be also examined. For systems with equivalent basis atoms no charge transfer occurs, therefore we perform a test on a system with non-equivalent basis atoms to investigate the effect of $\mathcal{H}_{\mathrm{LCN}}$. To this end we choose a thick (001)-Fe slab of 30 layers. The atoms at and near the surface have different surroundings than the bulk-like atoms in the middle of the slab. The local charge neutrality part should prevent too large and unphysical charge transfers, as explained in section 2.5. In figure 3.10 the Mulliken charge, the magnetic moment and the orbital moment for each layer is shown. The closer the atoms are to the surface

[7] Calculation was performed by B. Schweflinghaus with the FLEUR-code [56] using following computational parameters: $N_k = 1936$, $R_{\mathrm{max}} = 2.3$ a.u., $k_{\mathrm{max}} = 4.0$ a.u.$^{-1}$, $l_{\mathrm{max}} = 6$.

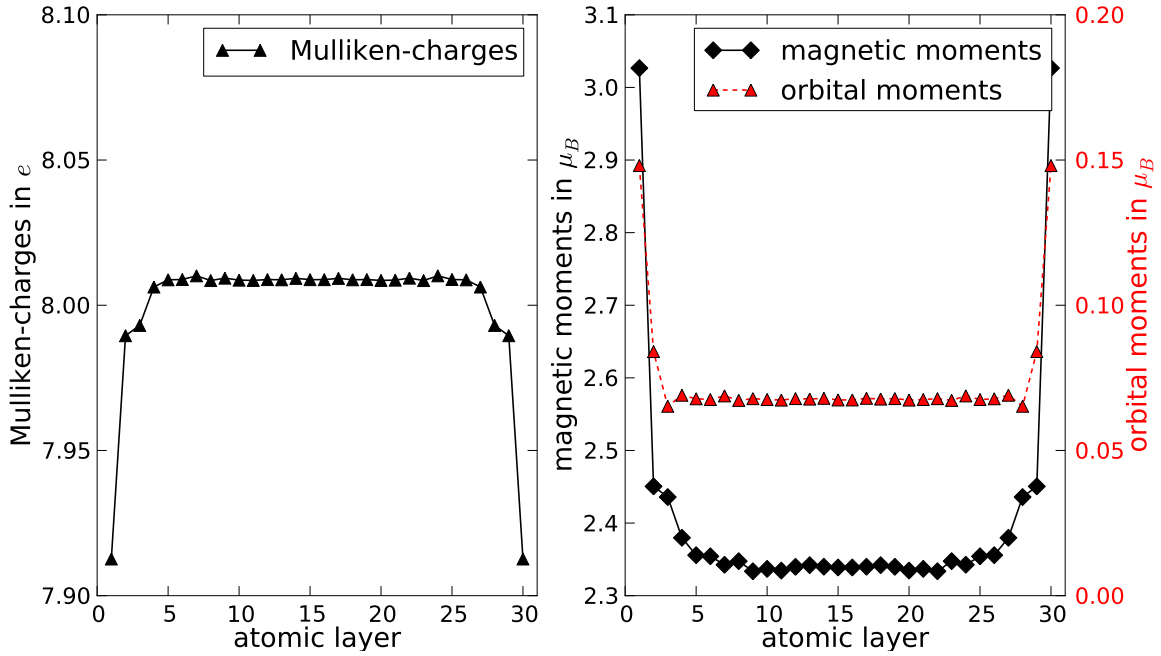

Figure 3.10: Magnetic moments (black curve in right plot), orbital moments (red curve in right plot) and Mulliken charges (left plot) of a 30-layer (001)-Fe slab. For the bulk-like atoms in the middle of the slab, the values are approximately those of bcc-Fe, whereas the surface atoms have different values. For the calculation 6400 k-points in the full Brillouin zone were used.

the larger the moments and the smaller the charges are. The bulk-like atoms in the middle of the slab-system have moments and charges, which are close to those of bcc-Fe. Therefore we can conclude, that the local charge neutrality part operates reasonably well in Fe slab systems. In chapter 5, where the charge transfer in the $L1_0$-Fe/Pt structure is investigated, the local charge neutrality part plays an important role not only for geometrically non-equivalent basis atoms, but also for chemically non-equivalent atoms.

3.5 Conclusion

The TB-scheme is able to describe all magnetic Fe-systems discussed in this chapter, at least qualitatively. For bcc-Fe the used parameter sets are well-adapted, therefore the quantitative description of bcc-Fe is in good agreement to *ab-initio* results. For free-standing Fe monolayers and Fe chains the TB-scheme allows us to predict at least their qualitative magnetic behaviour. These results allow us to expect that the TB-scheme is able to give a reasonable description of magnetism in Fe/Pt-systems.

4 Pure Pt-Systems

4.1 Introduction

Pt in its equilibrium bulk fcc structure with the lattice parameter $a = 3.92\,\mathring{A}$ is non-magnetic. So, why is it nevertheless an interesting element to examine magnetism? The answer is that Pt has a strong spin-orbit coupling and therefore can lead to very interesting SOC-induced magnetic behaviour in e.g. Fe/Pt-systems, as discussed in chapter 5. In chapter 3 the description of pure Fe-systems via the tight-binding scheme is examined, whereas this chapter focuses on pure Pt-systems. In section 4.2 the quality of the Pt-parameter set is examined via a comparison of the TB-band structure with an *ab-initio* result. Furthermore the SOC-parameters ξ_μ^{Pt} are determined with the help of the band splitting in the band structure. In section 4.3 the Stoner parameters of Pt are determined.

4.2 Band structure of fcc-Pt

In this thesis a LDA-parameter set for the tight-binding hopping parameters of Pt is used [15, 16]. The parameter set for Pt is presented in the appendix in the table B.3 of this thesis. In figure 4.1 the band structure of Pt calculated by the tight-binding scheme without SOC is compared to the band structure calculated by *ab-initio*[1]. For the TB-calculations of fcc-Pt in the sections 4.2 and 4.3 64000 k-points were used. Overall, the band structures are in good agreement, but there are some differences around the X- and L-point at the Fermi energy $\varepsilon_F = 0$, which could cause problems in determining sensitive Fermi surface properties such as the MCA.

It is essential to have a proper description of SOC in Pt to expect reasonable results for magnetism in Fe/Pt-systems. Therefore the SOC-parameters ξ_p^{Pt} and ξ_d^{Pt} are adjusted to the SOC-splitting in the band structure of an *ab-initio* calculation. To adjust the SOC-parameter ξ_d^{Pt} of the d-orbitals a band splitting of pure d-bands is needed. In figure 4.2 one can see such a splitting at the Γ-point, at which the d-orbitals are decoupled from the p-orbitals. A SOC-parameter of $\xi_d^{\mathrm{Pt}} = 0.53\,\mathrm{eV}$ leads to a good agreement of the TB-calculations and the *ab-initio* results. The SOC-splitting in the p-bands is not as important as the splitting in the d-bands for Pt, because the unoccupied p-bands lie too high in energy above the d-bands. Nevertheless, the SOC-splitting of the p-bands is not as completely negligible as for Fe. A value of $\xi_p^{\mathrm{Pt}} = 2.5\,\mathrm{eV}$ seems reasonable in

[1] Calculation was performed by H. Zhang with the FLEUR-code [56] using following computational parameters: $N_k = 6900$, $R_{\max} = 2.55\,\mathrm{a.u.}$, $k_{\max} = 3.9\,\mathrm{a.u.}^{-1}$, $l_{\max} = 8$.

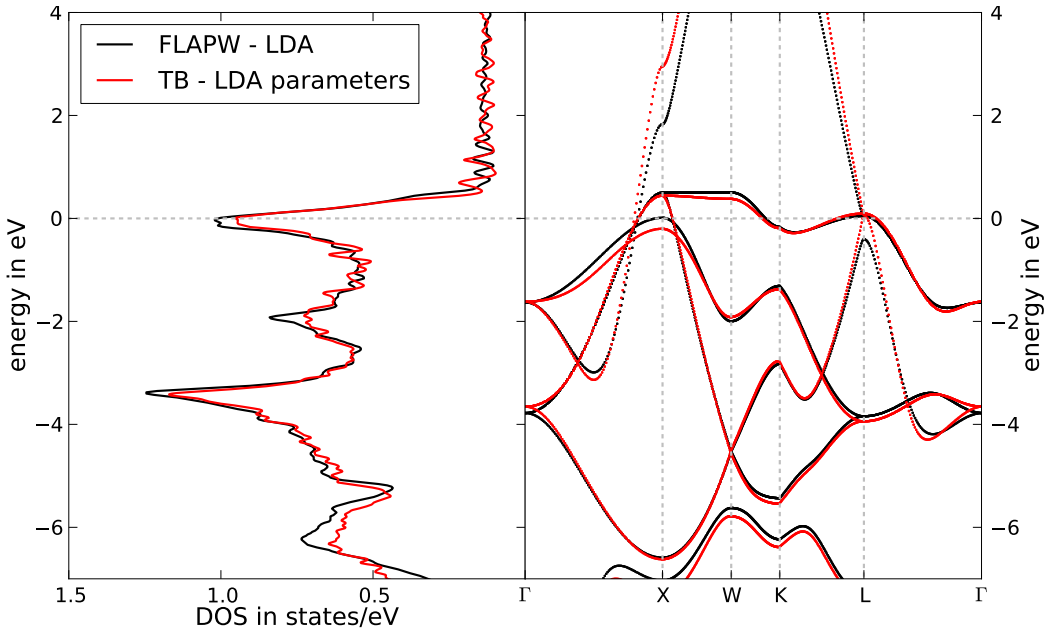

Figure 4.1: Band structure and DOS of fcc-Pt for the LDA case, the black curve is an FLAPW-calculation and the red one is a TB-calculation with a LDA parameter set. A lorentzian width of 50 meV is used for the DOS-calculation.

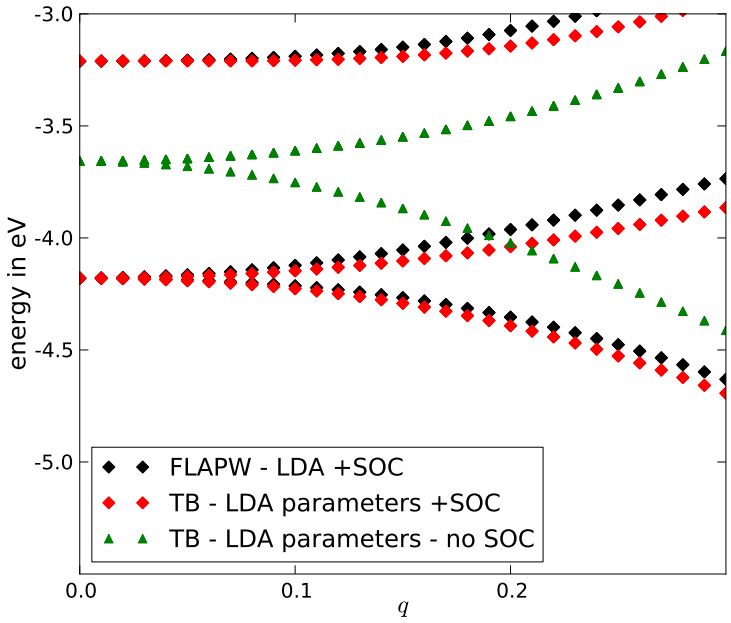

Figure 4.2: SOC-splitting of the d-bands around the Γ-point $q = 0$. The black curve is an FLAPW-calculation, whereas the red and green curve are TB-calculations with the LDA-parameter set and a d-SOC parameter of $\xi_d^{\mathrm{Fe}} = 0.53\,\mathrm{eV}$. The red curve is the result of a calculation with SOC and the green curve is a calculation without SOC.

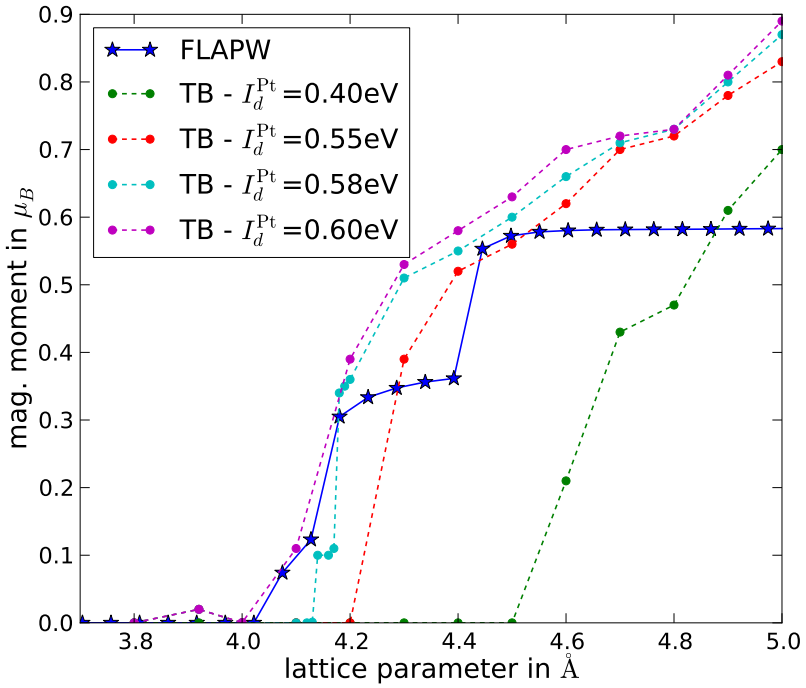

Figure 4.3: The magnetic moment of fcc-Pt depending on the lattice parameter a. The blue stars are FLAPW-calculations, whereas the rest of the curves are TB-calculations with different Stoner parameters I_d^{Pt}.

comparison to ξ_d^{Pt} and the bands above the Fermi energy are well described in a region of about 4 eV. We have chosen this value, because in *ab-initio* calculations the expectation value of the SOC-matrix in the p-orbitals is about 5-times larger than the expectation value in the d-orbitals. The expectation value in the d-orbitals was determined to about 0.56 eV within FLAPW.

4.3 Stoner parameters of Pt

Although fcc-Pt is non-magnetic, we determine the Stoner parameters of Pt for various reasons. First, Pt becomes magnetic for larger lattice parameters due to an increase of the exchange energy contribution over the kinetic energy contribution. This behaviour is described by the Stoner model, because the density of states at the Fermi energy increases the larger the lattice parameter of Pt becomes. Therefore, the Stoner criterion is fulfilled from a certain lattice parameter and on. Furthermore, Pt becomes polarized in Fe/Pt-systems due to the presence of the Fe atoms. There, the magnetic moments of the Pt atoms strongly depend on the used Stoner parameters of Pt.

We determine the Stoner parameters via the magnetic behaviour of fcc-Pt with increasing lattice parameter. In figure 4.3 the magnetic moment of fcc-Pt in dependence on

the lattice parameter is displayed. The result of an *ab-initio* calculation[2] is compared to TB-calculations with different Stoner parameters I_d^{Pt}. We always use $I_s^{\mathrm{Pt}} = I_p^{\mathrm{Pt}} = \frac{I_d^{\mathrm{Pt}}}{10}$ as approximation for the *s*- and *p*-magnetism. In principle the best agreement is achieved for $I_d^{\mathrm{Pt}} = 0.6\,\mathrm{eV}$, because fcc-Pt becomes magnetic at about $4.0\,\mathring{A}$ as in the FLAPW-calculation. However, the tight-binding calculation with $I_d^{\mathrm{Pt}} = 0.6\,\mathrm{eV}$ shows a small magnetic moment for the equilibrium lattice parameter of $a = 3.92\,\mathring{A}$ due to unknown reasons, which is the reason why we are using a Stoner parameter of $I_d^{\mathrm{Pt}} = 0.58\,\mathrm{eV}$ instead. In the *ab-initio* calculation the curve shows a plateau at about $4.4\,\mathring{\mathrm{A}}$ before rising to the atomic value of Pt of $2.0\,\mu_B$ for very large lattice parameters. The magnetic moment in the tight-binding scheme is strictly increasing to the atomic value without showing a plateau. This different behaviour is based mainly on the parametrization of the on-site elements for Pt, which is only very accurate in a small region around the equilibrium lattice parameter.

It should be noticed that the transition region around $4.0\,\mathring{A}$ to $4.2\,\mathring{A}$ from non-magnetic fcc-Pt to magnetic fcc-Pt is very sensitive to starting values, number of k-points and other properties, which have a strong influence on a self-consistent calculation. In this region the non-magnetic state and the magnetic state with a certain magnetic moment have almost the same energy. Therefore a Stoner parameter between 0.55 eV to 0.6 eV is a reasonable choice. The values of the Stoner parameters of Fe and Pt are in a good agreement with results obtained by DFT calculations [58, 59]. Whether the Stoner parameters are able to give a reasonable description of the polarization of the Pt atoms in Fe/Pt-systems is examined in chapter 5.

4.4 Conclusion

We have determined the SOC-parameters and Stoner parameters for Pt via comparisons with *ab-initio* results. Unlike in chapter 3 about pure Fe-systems, we do not present any results for systems beyond fcc-Pt. Therefore we can not be sure yet, that the parameters lead to a reasonable description of magnetism in Pt-systems. This examination still remains to be done in chapter 5.

[2] Calculation was performed by B. Schweflinghaus with the FLEUR-code [56]. An input generator was used, which optimized the computational parameters to the following range: $N_k = 5280 - 8736$, $R_{\max} = 2.41\,\mathrm{a.u.} - 3.17\,\mathrm{a.u.}$, $k_{\max} = 3.3\,\mathrm{a.u.}^{-1} - 4.1\,\mathrm{a.u.}^{-1}$, $l_{\max} = 8$.

5 Fe/Pt-systems

5.1 Introduction

Why is the magnetism in Fe/Pt systems so interesting and challenging? One could expect, that the magnetic behaviour of an Fe/Pt layer hardly differs compared to a pure Fe layer, which is examined in section 3.4. But this expectation is wrong because of various reasons. First, Pt is a non-magnetic element and becomes polarized in the presence of Fe mainly due to the hybridization of the Fe d-orbitals with the Pt d-orbitals. Furthermore, Pt atoms have a strong SOC compared to Fe atoms, therefore SOC-induced effects, like the Dzyaloshinskii-Moriya interaction (DMI) and the magnetic anisotropy, play an important role in Fe/Pt systems.

This chapter begins with an examination of the MCA of the $L1_0$-FePt structure depending on the ratio $\frac{c}{a}$ of the lattice constants and the Stoner parameters of Pt and Fe. The calculation of the $L1_0$ structure does not require as much computational time as the Fe/Pt slab systems and physical properties like the polarization of the Pt atoms, which play an essential role for the Fe/Pt slabs, can be computed very easily. Furthermore, *ab-initio* results exist for the MCA of the $L1_0$-FePt structure, which is compared to the tight-binding results in section 5.2. Therefore the $L1_0$-FePt structure is an appropriate introduction into the Fe/Pt systems. In section 5.3 the DMI in Fe/Pt layers is examined. Little is known about the DMI in this system, therefore it is enlightening to examine the dependence of the strength and the sign of the DMI on properties like the polarization of the Pt atoms or the band filling, which is presented in section 5.3. In the calculations, the polarization can be controlled via the Stoner parameter I_d^{Pt} within the tight-binding scheme, whereas the band filling is controlled via the number of electrons. Calculating the DMI in Fe/Pt slabs is computationally very challenging, therefore the numerical properties of the method and its problems are described in detail in sections 5.3 and 5.4.

5.2 $L1_0$-FePt structure

The $L1_0$-FePt structure consists of alternating atomic layers of Fe and Pt along the (001)-direction, which will be referred to as c-axis in the following. The $L1_0$ structure is displayed in figure 5.1. In our tight-binding calculations a lattice parameter of $a = 2.721\,\text{Å}$ and a ratio of $c/a = 1.389$ are used to compare the MCA with *ab-initio* results. The $L1_0$-FePt system shows a large MCA of about 2.7 meV with the easy axis along the c-axis in *ab-initio* calculations [60, 61, 62]. A capped Pt-Fe-Pt(001) layer system has an even larger MCA than the $L1_0$ structure [63]. Therefore chemically ordered Fe/Pt systems are promising candidates for magnetic storage devises.

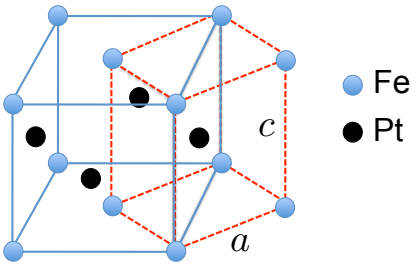

Figure 5.1: $L1_0$ structure. We use the two-atomic tetragonal unit cell (red dashed lines) with $a = 2.721$ Å and $c/a = 1.389$.

For our tight-binding calculations of the MCA of the $L1_0$-FePt structure 64000 k-points were used, which is enough to guarantee that the MCA is converged to 0.1 meV accuracy. We find a value of 4.1 meV for the MCA with the c-axis as easy axis, which is about 50% larger than the values derived via *ab-initio*, although the direction of the easy axis is correctly reproduced. The magnetic moment of Fe is $2.15\,\mu_B$ and the polarized Pt atom has a moment of $0.43\,\mu_B$.

We should note that the value for the MCA depends on the on-site energies of Fe and Pt and there exists no rule which parameter λ should be used in the expression 2.24 for the local atomic density:

$$\rho_i = \sum_{j \neq i} e^{-\lambda_j^2 \cdot R_{ij}} \cdot f_c(R_{ij})\,. \tag{5.1}$$

In this thesis λ_j is used, which can be motivated by the assumption that the local atomic density of atom i can be expressed as sum over densities coming from neighbouring atoms. But in principle a new parametrization for the on-site elements and the Fe-Pt hoppings (see eq. 2.23 and 2.21) would be necessary for more accurate results, as it is done for some binary compounds in [16, 17]. Therefore to estimate the error, which occurs due to an inefficient on-site parametrization , we also calculated the MCA using λ_i and $\frac{1}{2}(\lambda_i + \lambda_j)$ instead of λ_j in eq. 2.24. Using λ_i leads to a MCA of 2.3 meV with magnetic moments of $2.67\,\mu_B$ for Fe and $0.40\,\mu_B$ for Pt in good agreement to the experimental result of a total moment of $3.00\,\mu_B$ [64], whereas using $\frac{1}{2}(\lambda_i + \lambda_j)$ leads to a MCA of 3.3 meV and a magnetic moment of $2.38\,\mu_B$ for Fe and $0.42\,\mu_B$ for Pt. Besides the fact that the values are not in nice agreement, therefore the parametrization is not able to allow a quantitative good description, there is the good message, that the easy axis is along the c-axis for all cases. This gives us hope that in the same way as for Fe monolayers, Fe slabs and Fe chains (see section 3.4) a qualitatively good description is possible for Fe/Pt systems. To underline this statement, the MCA of the $L1_0$-FePt structure is calculated depending on the $\frac{c}{a}$-ratio. The results of the MCA and the corresponding magnetic moments for Pt and Fe can be seen in figure 5.2. For larger $\frac{c}{a}$-ratios the system tends to have its easy axis along the c-axis, whereas for smaller $\frac{c}{a}$-ratios the easy axis is perpendicular to the c-axis. This behaviour is in qualitatively good agreement with the results in [62, 65]. Furthermore the magnetic moment of the Pt atom increases with decreasing $\frac{c}{a}$-ratio due to a larger hybridization between the Fe

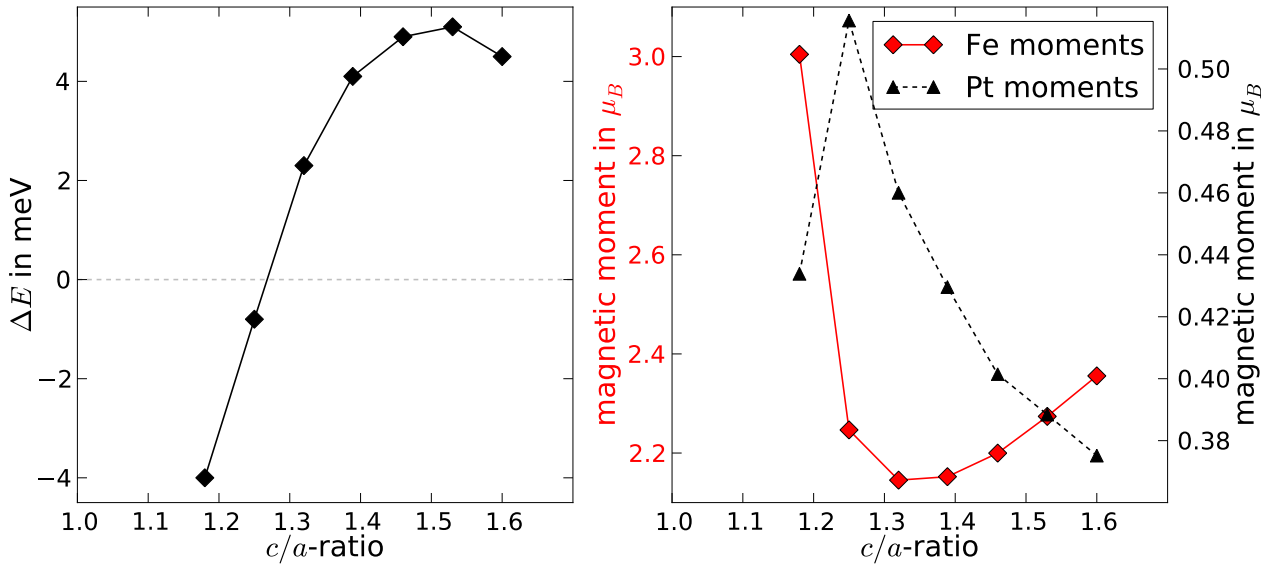

Figure 5.2: Left panel: The MCA $\Delta E = E_{\rightarrow} - E_{\uparrow}$ of the $L1_0$-FePt structure depending on the $\frac{c}{a}$-ratio. $E_{\rightarrow}$ is the energy for the system with magnetization along the a-axis, whereas $E_{\uparrow}$ is the energy for the system with magnetization along the c-axis. Right panel: The magnetic moments of the Fe (red curve) and Pt (black curve) atom of the $L1_0$-FePt structure depending on the $\frac{c}{a}$-ratio.

3d-electrons and the Pt 5d-electrons.

Let us try to answer the question, why does the $L1_0$-FePt structure show such a large MCA for a bulk system? First one can take a look to the extreme cases $\frac{c}{a} = 1$ and $\frac{c}{a} \rightarrow \infty$ for which we know the MCA. The case $\frac{c}{a} = 1$ describes a cubic system in the CsCl structure, therefore the MCA is zero (to second order), whereas the case $\frac{c}{a} \rightarrow \infty$ describes isolated Fe monolayers, for which we expect a large MCA. Therefore the uniaxial symmetry is crucial for the large MCA of the $L1_0$-FePt structure, which is also explained in more detail in [61, 66]. Besides the uniaxial symmetry, the large SOC of the Pt atoms also plays an important role. We have performed a calculation, in which we have switched off the SOC on the Pt atoms. The MCA of the system with a value of about 0.4 meV with the c-axis as easy axis is much smaller than the MCA of 4.1 meV with SOC on the Pt atoms.

Calculations of the MCA of the $L1_0$ structure with different Stoner parameters for Pt and Fe were also performed. The MCA and the magnetic moment of Pt is almost independent of the Stoner parameter of Pt, if the Stoner parameter is not increased to values, where Pt becomes magnetic even without the presence of the Fe atoms. On the contrary, the Stoner parameter of Fe has a big influence on the MCA and the magnetic moment of Pt. This is an indication, that the magnetic moment of Pt is mainly coming from the hybridization between the Fe states and Pt states.

Therefore we come to the conclusion, that the large MCA of the $L1_0$-FePt structure

is based on the uniaxiality of the system and the large SOC of Pt in combination with the hybridization with the Fe states. After all the tight-binding scheme seems to be able to describe also binary systems like Fe/Pt systems, at least qualitatively, although the used parametrization is not suited to binary systems and we had to improvise with eqs. 2.24 and 2.25.

5.3 Examination of the Dzyaloshinskii-Moriya interaction

The Dzyaloshinskii-Moriya interaction (DMI) is a quite recent field of research, although the corresponding symmetries were examined in the 1960's by Dzyaloshinskii and Moriya in weak ferromagnetic systems [3, 4]. Recently a spin-spiral ground state with a unique rotational sense has been found in Mn/W(110) using spinresolved STM-measurements [10, 11], which can be theoretically explained by the DMI. Therefore a calculation to obtain the strength and the sign of the DMI is very interesting. Computationally the DMI is very challenging due to its small energy scale of at most a few meV. Furthermore, slabs consisting of several layers of transition metals are typically examined in order to compare the results with experimental studies. Therefore we are confronted with the problem of having to use a lot of k-points for describing a large system. Some of these numerical problems are discussed in section 5.4 and the delicate numerical behaviour depending on the number of k-points is examined in this section. Afterwards the qualitative behaviour of the DMI depending on the thickness of the slab, the Stoner parameter of Pt and the band filling, is examined. The calculations are performed using some approximations as the 1st-order perturbation theoretical treatment of spin-orbit coupling so that use can be made of the generalized Bloch theorem. First, however, we study the validity of this approximation using a very simple test system.

5.3.1 Validity of the 1st-order SOC approximation

First of all it should be mentioned, that spin-spirals of the type (c) in figure 2.15 are used to examine the DMI. Therefore the phase factors $(s_i^j(\boldsymbol{q}\cdot\boldsymbol{R}_n))^{\sigma\sigma'}$ of the form A.12 are used for the calculations using the generalized Bloch theorem (see section 2.8). All the calculations in section 5.3.2 use the force theorem (see section 2.9) and a 1st-order SOC description (see section 2.8) to utilize the computational advantages of the generalized Bloch theorem. The DMI is analysed for Fe/Pt-slabs, therefore it has to be discussed if the 1st-order SOC description is sufficient for a system, where one has to deal with a large SOC strength. In the following, a supercell calculation with full SOC (see fig. 2.13a) is compared to a corresponding calculation in a small unit cell using the generalized Bloch theorem and 1st-order SOC to obtain the DMI (see fig. 2.13b). Due to the small q-values we are going to focus on, we use one of the simplest systems with non-vanishing DMI, which is an Fe/Pt zigzag chain (see fig. 5.3). For this system the values obtained by the tight-binding method are not very reliable due to the very different structure compared to the Fe and Pt bulk structure. Nevertheless the system should be sufficient to evaluate

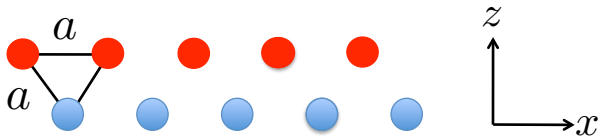

Figure 5.3: Fe/Pt zigzag chain with a lattice parameter of $a = 2.22\,\text{Å}$. The Fe atoms are indicated in red and the Pt atoms are blue.

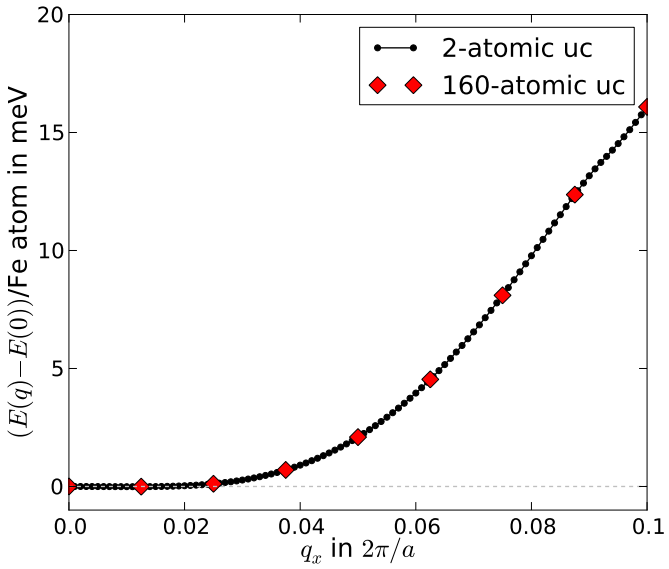

Figure 5.4: Magnon dispersion of the Fe/Pt zigzag chain without SOC along the way $0 \leq q \leq 0.1$. The red diamonds display the results for the non-collinear 160-atom supercell calculation, whereas the results for the 2-atomic unit cell using the generalized Bloch theorem is depicted by the black circles.

the quality of the 1st-order SOC description. For all calculations for the zig-zag chain the force theorem[1] is used, unless differently indicated.

For the calculation of the 1st-order SOC contribution in the frame of the generalized Bloch theorem a 2-atomic unit cell with a lattice parameter of $a = 2.22\,\text{Å}$, containing one Fe and one Pt atom, is used. A large number of 3200 k-points guarantees that the DMI is converged even in the region of the small q-values, where one has to handle very small energy differences of about $10^{-4}\,\text{eV}$. To allow a comparison for small q-values between the 1st-order SOC calculation and the full SOC calculation, a 160-atomic supercell with 40 k-points is used. Therefore the smallest q-value (besides $q = 0$), which can be treated in the supercell, is $q = 0.0125$.

In figure 5.4 the magnon dispersion of the Fe-Pt chain for the supercell calculation (red diamonds) and the generalized Bloch theorem calculation (black curve) are displayed in

[1]The force theorem needs a reasonable starting density, which is the converged density for the ferromagnetic case without SOC using 3200 k-points for the small unit cell and 40 k-points for the supercell, unless differently specified.

a region of $0 \leq q \leq 0.1$. In these calculations no SOC was considered, therefore the two methods should lead to the same results, as shown in the figure. The magnon dispersion starts remarkably flat from $q = 0$, which can be explained again by the Bethe-Slater curve as indicated in figure 3.8.

In figure 5.5 the pure SOC contribution to the band energy is displayed in dependence of q for several different calculations . For the 1st-order SOC calculation in the framework of the generalized Bloch theorem, $\Delta E_{\mathrm{SOC}}(q)$ via eq. 2.86 (black curve) and 2.90 (green solid curve) are displayed. In the first case the Fermi energy remains unchanged after adding the 1st-order perturbation theoretical contributions from SOC, whereas the second case considers the change in the Fermi energy due to the shifts in the band energies (see fig. 2.14). As discussed in section 2.8, there is a non-negligible difference between $\Delta E_{\mathrm{SOC}}(q)$ determined with or without recalculated Fermi energy even for the smaller q-values. Using a starting density for the force theorem calculations, which is based on a ferromagnetic system with consideration of SOC, leads to the blue curve for the case of recalculated Fermi energy. Therefore also the choice of the starting density leads to differences, which is also examined in [12]. Nevertheless the linear behaviour near $q = 0$ is the same in all three cases. Thus, if we are only interested in the determination of the DM-constant[2] D, it is not necessary to recalculate the Fermi energy after adding the SOC-contribution in 1st-order perturbation theory. But it should be emphasized again, that the pure SOC contribution could differ drastically for the different calculations for larger q-values, as long as the starting density is ferromagnetic.

The red markers in figure 5.5 display the pure SOC-contribution depending on q for the 160-atom supercell, considering full SOC. The presented data is the difference between a full SOC calculation and a calculation without SOC, therefore $(E_{\mathrm{SOC}}(q) - E_{\mathrm{no-SOC}}(q)) - (E_{\mathrm{SOC}}(0) - E_{\mathrm{no-SOC}}(0))$. For the calculation with full SOC, the density of the corresponding ferromagnetic system with SOC was used as starting density for the force theorem calculation. In contrast the green hexagonal markers are the results, if we use the difference between spin-spirals of opposite rotation-sense, i.e. $\frac{1}{2} \cdot [E_{\mathrm{SOC}}(q) - E_{\mathrm{SOC}}(-q)]$, motivated by $\Delta E_{\mathrm{SOC}}(-q) = -\Delta E_{\mathrm{SOC}}(q)$ for small q. It is not quite clear which of the curves should be used to compare the SOC-contribution to the band energy of a full SOC calculation with a corresponding calculation using the 1st-order perturbation theory approach. The curve obtained by the difference between spin-spirals of opposite rotation-sense is in a better qualitative agreement with the 1st-order perturbation theoretical calculations. But in both cases, there are again non-negligible differences compared to the 1st-order perturbation theoretical treatment, except for very small q-values.

As conclusion one can say that all methods are in a good agreement concerning the determination of the DM-constant D. Nevertheless for q-values larger than $q = 0.02$ all methods predict somewhat different results, which can even differ in sign, as can be observed in figure 5.6, showing the DMI over half of the Brillouin zone. Despite this large numerical differences, there are some similarities in the curve behaviour, e.g. the

[2] This constant becomes important in the framework of a micromagnetic model [48, 49] (see also section 2.10).

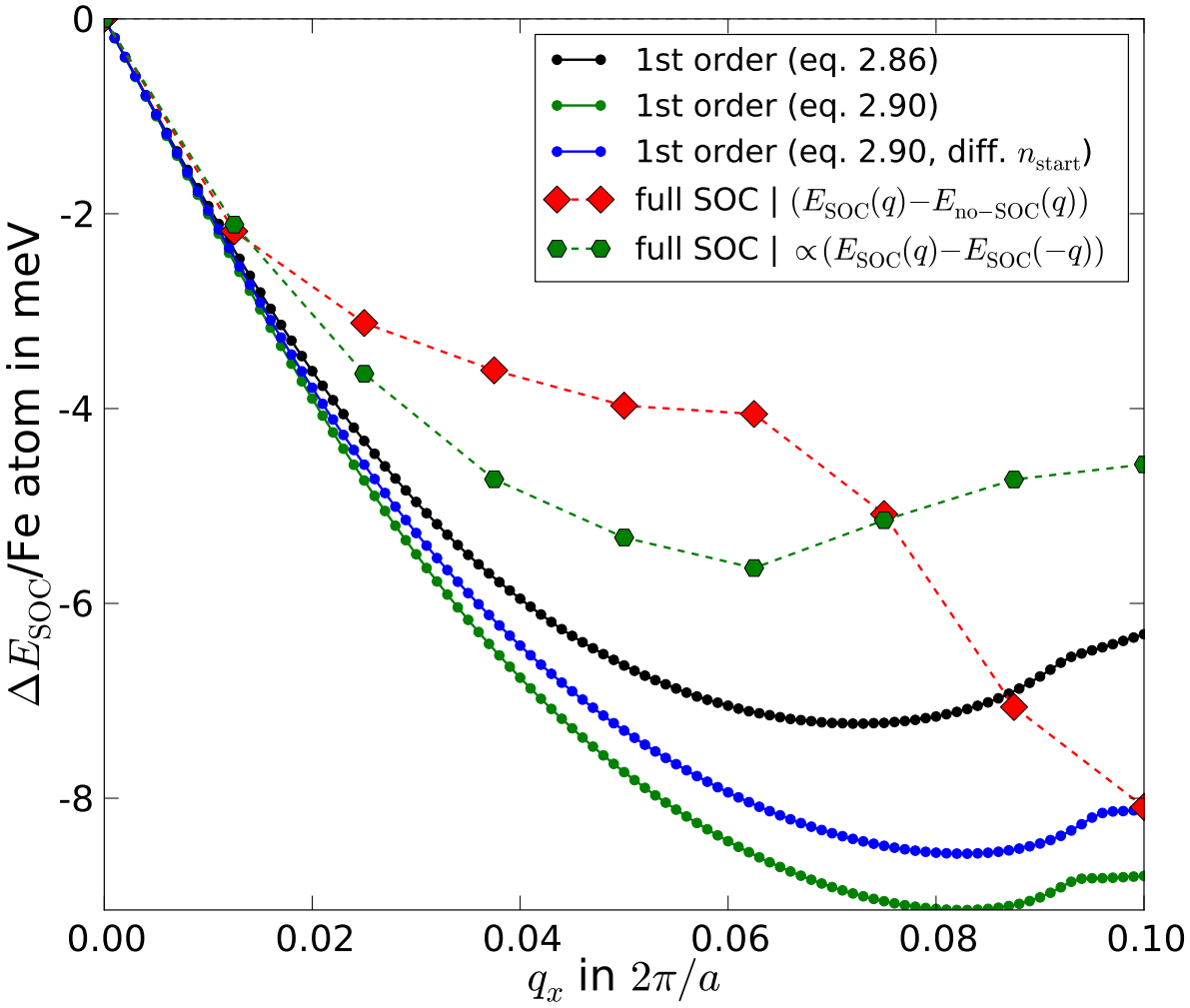

Figure 5.5: The pure SOC-contribution to the band energy from several calculations for the Fe/Pt zigzag chain. The black, blue and green solid curves are the results using 1st-order perturbation theory to treat SOC for spin-spirals. For the black curve eq. 2.86 is used, whereas the green curve is the result using eq. 2.90. For the blue curve eq. 2.90 is also used, but a different starting density n_{Start} is used (more details in text). The green hexagonal markers and the red markers are the results using the supercell with full SOC. For the red markers $E_{\mathrm{SOC}}(q) - E_{\mathrm{no-SOC}}(q) - (E_{\mathrm{SOC}}(0) - E_{\mathrm{no-SOC}}(0))$ is used to obtain the pure SOC-contribution, whereas $\frac{1}{2} \cdot [E_{\mathrm{SOC}}(q) - E_{\mathrm{SOC}}(-q)]$ is used for the green hexagonal markers.

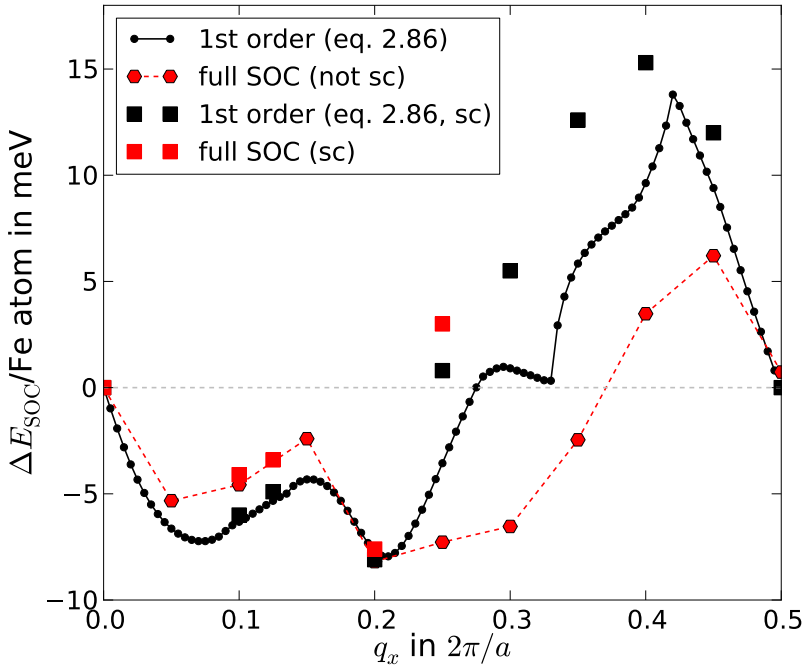

Figure 5.6: The pure SOC-contribution of the Fe/Pt zigzag chain in half of the Brillouin zone. The red hexagons display the results for the 160-atom supercell calculation, whereas the results for the 2-atomic unit cell using the generalized Bloch theorem are represented by the black curve. The squares display the results of corresponding self-consistent calculations.

single sign-change of the DMI and the amplitude of the DMI. Whether these large numerical differences are only due to the different treatments of SOC or if the force theorem approximation plays also an essential role was examined as well. This was done by comparing the self-consistent results of the supercell considering full SOC and the 2-atomic unit cell with the 1st-order perturbation treatment of SOC for selected q-points. Before adding the 1st-order SOC-contribution, the spin-spiral without SOC was calculated self-consistently for these certain q-values. Calculations for $q = 0.1$, $q = 0.125$, $q = 0.2$, and $q = 0.25$ were performed, which are presented as squares in figure 5.6. The black markers are the results for the 1st-order perturbation theoretical treatment on top of the self-consistent spin-spiral calculation and the red markers display the self-consistent results for the full SOC treatment in the supercell. The results of the force theorem calculations are in good agreement with the corresponding self-consistent results for smaller q-values. Therefore the differences between the 1st-order perturbation theoretical treatment of SOC and the full SOC calculations in figure 5.5 occur due to the different treatment of SOC and not due to the force theorem approximation. For larger q-values the difference between the self-consistent results and the force theorem results increases as one would expect from figures like 3.7 or 5.13. There is no comparison between self-consistent results and force theorem results for values $q > 0.25$ for the full

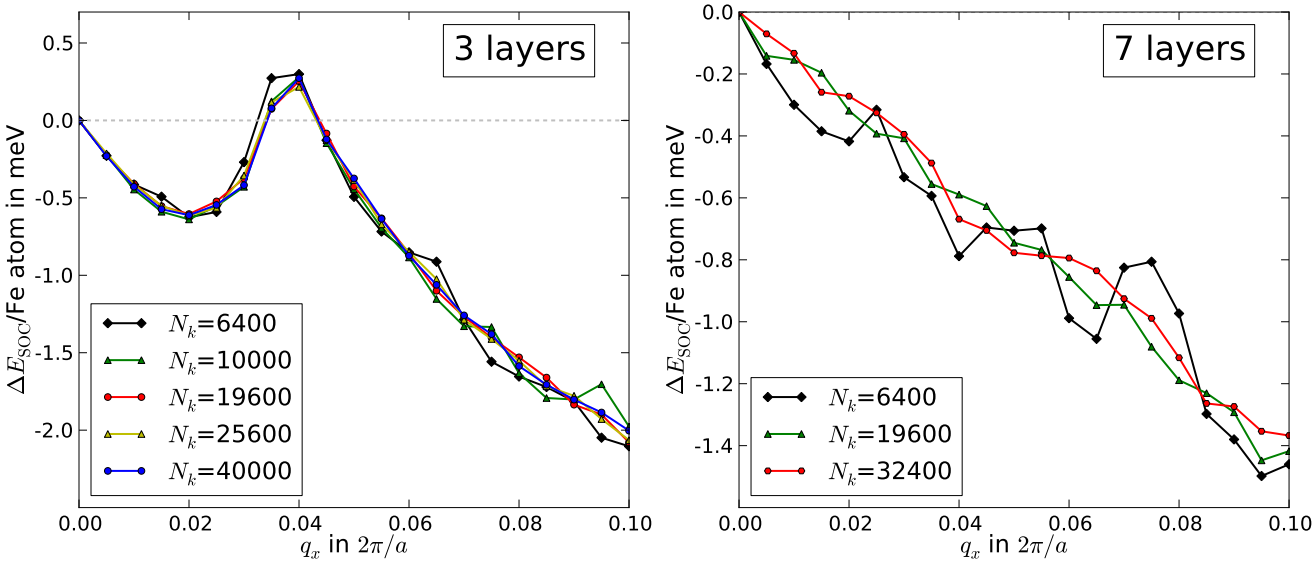

Figure 5.7: Left panel: DMI of the Fe/Pt(001) slab, consisting of 3 layers Pt, for different number of k-points N_k. Right panel: DMI of the Fe/Pt(001) slab, consisting of 7 layers Pt, for different number of k-points N_k.

SOC treatment in the supercell due to convergence problems, as the constraint is not working well for these cases (see section 5.4.2).

5.3.2 Dzyaloshinskii-Moriya interaction in Fe/Pt(001) slabs

The comparison in 5.3.1 between the full SOC calculation in a supercell and the 1st-order perturbation theoretical treatment of SOC for the Fe/Pt zigzag chain has yielded, that the 1st-order perturbation theory treatment is sufficient to determine the DM-constant D. Even more the qualitative behaviour of the SOC-contribution of the band energy is in a satisfactory agreement for $q \leq 0.1$ (see fig. 5.5). Therefore the magnon dispersion and the SOC-contribution to the band energy for the Fe/Pt(001) slabs is examined only in the region of $0 \leq q \leq 0.1$ using 1st-order perturbation theory for SOC. The Fe/Pt(001) slab consists of one mono-layer Fe and several layers Pt with the crystallographic (001) orientation of an fcc lattice. In the following a lattice parameter of $a = 2.77186$ Å of the quadratic Bravais lattice is used and as distance between the layers a value of 1.96 Å is used.

Convergence with the number of k-points: Due to the small energy scale of the DMI, we have to use a lot of k-points in the force theorem calculations to guarantee converged results and a smooth curve behaviour. In figure 5.7 the convergence of the DMI with the number of k-points for an Fe/Pt(001) slab, consisting of 3 layers Pt (left panel) and 7 layers Pt (right panel), are presented. The system with 3 layers converges much faster than the system with 7 layers. For a reliable treatment of the DMI more

than 7 layers are required, and therefore together with some memory-storage problems, explained in section 5.4, it was not possible to obtain a smooth curve behaviour for the DMI for the Fe/Pt slabs in a reasonable amount of computational time. However one can see in fig. 5.7, that the overall slope is consistent for all presented k-point numbers, so that the DM-constant D could be even found by a fit in the case using 6400 k-points. All following calculations are done with 19600 k-points.

This numerical problem to obtain a smooth curve behaviour is not present for the magnon dispersions without SOC. Due to their larger energy scale in the interval $0 \leq q \leq 0.1$, the curves are sufficiently smooth for 19600 k-points.

Dependence on number of Pt layers: We investigate the magnon dispersion with and without SOC in Fe/Pt(001) slabs depending on the number of Pt layers. We compare the results for 3, 5, 7, 9 and 11 layers Pt and determine the spin-stiffness constant A and the DM-constant D for each case using linear regression. As explained in section 2.10.1 and 2.10.2, we can determine D by using linear regression on the antisymmetric part of the magnon dispersion $E(\boldsymbol{q})$, i.e. the SOC-contribution $\Delta E_{\mathrm{SOC}}(\boldsymbol{q})$. To obtain the spin-stiffness constant A, one can use a quadratic fit to the magnon dispersion $(E(\boldsymbol{q}) - E(0))$ of the Fe/Pt slab without SOC. But of course also a linear regression, which is used in this thesis, applied on $\sqrt{E(\boldsymbol{q}) - E(0)}$ can be used to derive A as long as $E(\boldsymbol{q}) - E(0) \geq 0$. Due to the fact that the linear behaviour of the DMI is only valid for small q-values, as assumed in the micromagnetic model (see eq. 2.105), we use only the values for $q \leq 0.02$ to determine D. In our case this corresponds to 5 q-points, which are used for the linear regression. The quadratic behaviour of the magnon dispersion without SOC is valid over a wider range, as one can see in the left panel of fig. 5.8 and therefore we use all q-values up to 0.05, i.e. 10 q-points, to determine the spin-stiffness constant A. The error, which is automatically calculated within the linear regression strongly underestimates the "real" error. Therefore to estimate a rough error for A and D, linear regressions with a few more or less q-points were performed to compare the values for A and D.

In figure 5.8 the magnon dispersion without SOC (left panel) and the SOC-contribution to the band energy (right panel) is displayed for Fe/Pt(001) slabs, consisting of different numbers of Pt layers. For the magnon dispersion without SOC a convergence concerning the number of layers is recognizable, starting with 7 layers of Pt. This can be also observed in the spin-stiffness constant A, which is displayed in the table 5.1. But for the DM-constant D, which can be seen in table 5.1, a clear convergence with the number of Pt layers is not observed yet. This could be caused by the long-ranged behaviour of the DMI. Therefore more Pt-layers are needed to obtain convergence concerning the number of layers.

Nevertheless one can observe a tendency to a similar behaviour of the DMI for the systems with 7, 9 and 11 Pt layers. The systems with 3 and 5 layers of Pt behave very differently compared to the systems with 7, 9 or 11 layers of Pt due to the symmetry-breaking effect at the Pt surface and the long-ranged DMI. This symmetry-breaking effect at the Pt surface is the reason, why the layer-decomposed DMI has a large con-

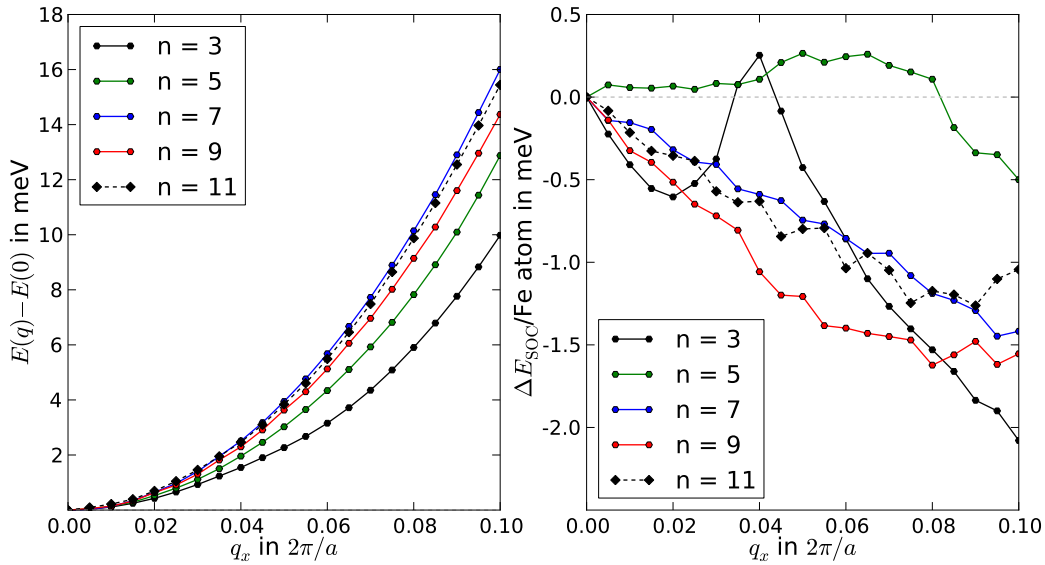

Figure 5.8: Left panel: Magnon dispersion without SOC for several Fe/Pt slabs consisting of different number of Pt layers n. Right panel: SOC-contribution to band energy via eq. 2.86 for several Fe/Pt slabs consisting of different number of Pt layers n.

n_{Layer}	3	5	7	9	11
A in meV $\cdot$ nm^2	78 $\pm$ 10	96 $\pm$ 5	120 $\pm$ 10	113 $\pm$ 5	125 $\pm$ 15
D in meV $\cdot$ nm	-10.7 $\pm$ 1.0	1.4 $\pm$ 0.5	-4.1 $\pm$ 0.7	-7.8 $\pm$ 0.8	-5.9 $\pm$ 0.9

Table 5.1: The spin-stiffness constant A and the DM-constant D of Fe/Pt(001) slabs, consisting of one Fe layer and n_{Layer} Pt.

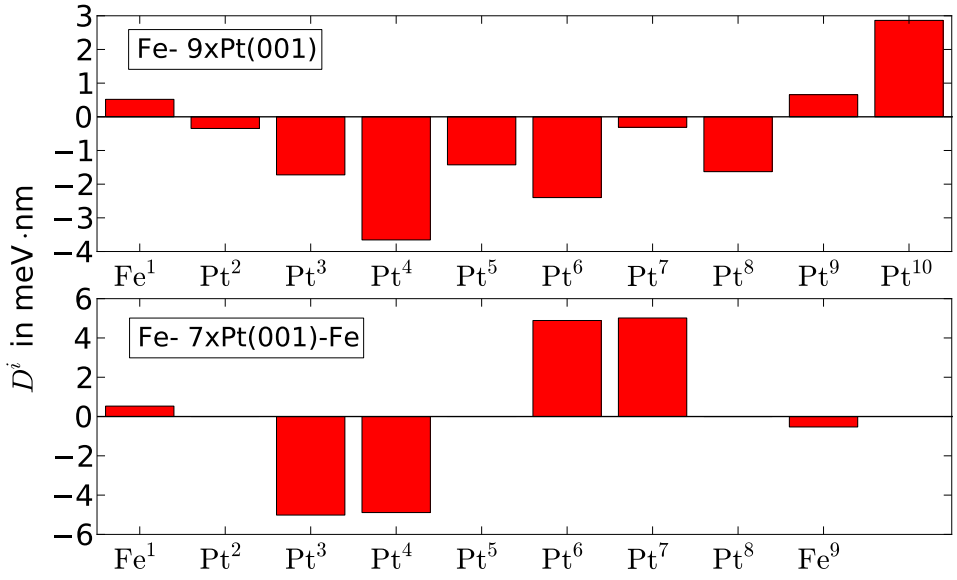

Figure 5.9: Upper panel: Layer-decomposition of the DM-constant D into layer-decomposed contributions D^i for the Fe/Pt(001) slab, consisting of 9 layers Pt. The symmetry-breaking effect on the Pt-surface leads to a large contribution to the DMI. Lower panel: Layer decomposition of a symmetric Fe/Pt(001) slab, consisting of 7 layers Pt. The layer-decomposed contributions D^i of the atoms Pt^2 and Pt^8 are about $0.02\text{meV} \cdot \text{nm}$, therefore not observable on this scale. The layer-decomposed contribution to the atom Pt^5 is zero, due to symmetry reasons.

tribution at the Pt surface even for the system with 11 layers of Pt. In the upper panel of figure 5.9 the contribution to the DM-constant from each layer of the Fe/Pt(001) slab, consisting of 9 layers Pt, is presented. To determine the contribution from each layer, the SOC-contribution to the band energy is layer-decomposed straightforwardly via eq. 2.85. One can obtain the layer-resolved DM-constants by using linear regression on these energy-contributions. The DMI should decay with increasing distance from the Fe surface, but in our calculations of the Fe/Pt slabs no decaying behaviour is observable, reflecting the quantum confinement that is still present for 9 layers. We suppose, that we need a lot more layers to properly describe the layer dependence of the DMI.

To avoid the large contribution to the DMI from the Pt-surface, a symmetric Fe/Pt slab can be used. The total DMI in a symmetric Fe/Pt slab is zero due to the presence of inversion-symmetry, but the layer-decomposed DMI does not vanish. In the lower panel of figure 5.9 the layer-decomposed DMI of a symmetric Fe/Pt(001) slab, consisting of 7 layers Pt, is displayed. For the first 5 layers, consisting of 1 Fe layer and 4 Pt layers, the spin stiffness constant has a value of $(101 \pm 6)\,\text{meV} \cdot \text{nm}^2$ and the DM-constant has a value of $(-9.2 \pm 0.3)\,\text{meV} \cdot \text{nm}$. A remarkable result of the layer-decomposed analysis is the low DMI in the Pt layers, which are adjacent to the Fe layers. This is in contrast to the finding that the largest contribution to DMI comes from these adjacent layers in

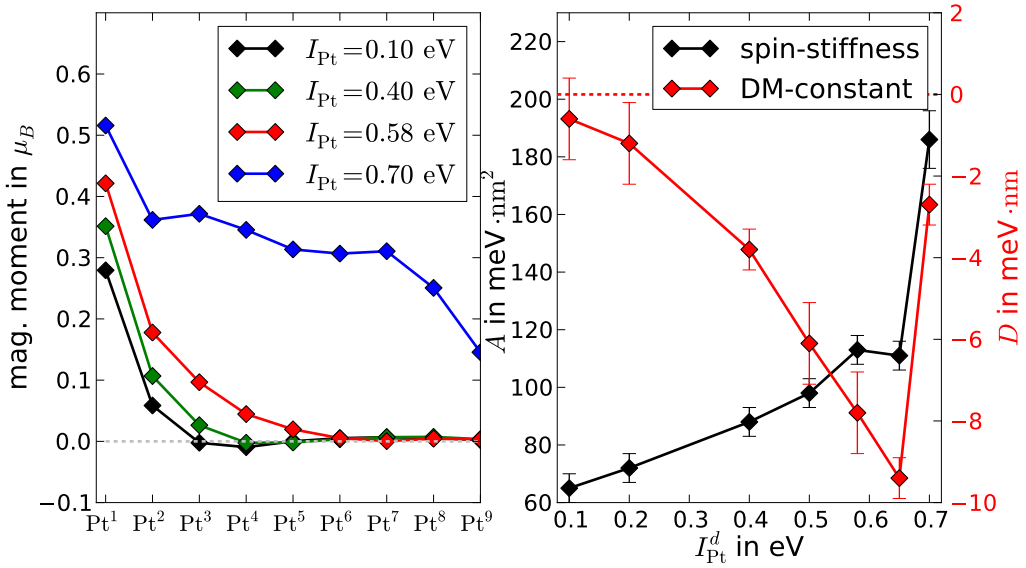

Figure 5.10: Left panel: Magnetic (Mulliken-)moments of Pt in the converged ferromagnetic Fe/Pt(001) slab, consisting of 9 layers Pt in dependence of the Stoner parameter I^d_{Pt}. Negative values of the magnetic moments correspond to magnetic moments pointing along the $-z$-direction. Right Panel: Spin stiffness A (black curve) and DM-constant D (red curve) in dependence of the Stoner parameter of Pt. The error-bars show the roughly estimated errors for A and D (see text).

Cr/W slabs or Fe/W slabs [12]. Possibly this again reflects the quantum confinement in the slab.

Dependence on the Stoner parameter of Pt: One would expect a delicate dependence of the polarized Pt moments on the Stoner parameter I^d_{Pt} of Pt. But in the examination of the $L1_0$-FePt structure in section 5.2, a surprising result was obtained, that the magnetic moment of Pt was almost independent of the Stoner parameter. Therefore it would be interesting to examine the influence of the Stoner parameter on the polarized Pt moments in an Fe/Pt(001) slab, consisting of 9 layers Pt. In the left panel of figure 5.10 the magnetic (Mulliken-)moments of the Pt atoms are displayed for different Stoner parameters I^d_{Pt}. There one can clearly observe a delicate dependence of the magnetic moments on the Stoner parameter. For a smaller Stoner parameter the magnetic moments of Pt decrease stronger with increasing distance from the Fe layer. But the magnetic moment of Pt does not vanish for a Stoner parameter of zero, due to a strong hybridization between Fe and Pt. For a Stoner parameter of $I^d_{\mathrm{Pt}} = 0.7\,\mathrm{eV}$ Pt becomes magnetic even without the presence of Fe, which is the reason why the Pt moments behave very different compared to the other cases.

Due to the strong dependence of the magnetic moments on the Stoner parameter, one can expect also a large influence on the spin-stiffness constant A and the DM-constant

D. In the right panel of figure 5.10, A (left scale) and D (right scale) are displayed versus the Stoner parameter I^d_{Pt}. The spin-stiffness constant increases with increasing Stoner parameter, which can be simply understood by taking into account the behaviour of the magnetic moments. As long as the Stoner parameter does not exceed the value, where Pt becomes strongly magnetic, A seems to be linearly dependent on the Stoner parameter. The absolute value of the DM-constant D has also the tendency to increase for increasing Stoner parameter, but as soon as Pt becomes strongly magnetic the absolute value of D is diminished.

At this point we should come back to the determination of the Stoner parameter I^d_{Pt} via the lattice parameter dependence of the magnetic moment in fcc-Pt as it is done in section 4.3. Due to the sensitivity of the magnetic moment of Pt, especially in the transition region between non-magnetic fcc-Pt and magnetic fcc-Pt, this method is probably not the optimal method to determine I^d_{Pt}. In addition, the parameter set of Pt [15, 16] only ensures an accurate description of the electronic structure for a small area around the equilibrium lattice constant of fcc-Pt. A more appropriate method to determine I^d_{Pt}, in particular for the treatment of Fe/Pt slabs, could be based on the polarization of the Pt atoms in Fe/Pt slabs, as it is presented in the left panel of fig. 5.10. An FLAPW-calculation of the polarization of the Pt atoms in an Fe/Pt slab could be used to obtain the specific Stoner parameter, for which the polarization is well described.

Dependence on the band filling: An interesting examination, which can be done very easily within the tight-binding scheme, is to examine the behaviour of A and D with respect to a change in the band filling. The band filling in an Fe/Pt(001) slab, consisting of 9 layers Pt, is changed by varying the number of electrons of the Pt atoms[3]. In the following the number of electrons vary between 9.0 and 11.0 in 0.25-steps. A Pt atom consists of 10 valence electrons, therefore if we change this number, our slab does not describe an Fe/Pt slab any more. For example the case of 11 electrons models the band filling in a Fe/Au slab, whereas the case of 9 electrons models the band filling in a Fe/Ir slab. It should be noted, that Au and Ir are not properly described only by adjusting the band filling. In principle the hopping parameters, the Stoner parameters and the SOC-parameters have to be also adjusted, which is not done in the following.

In figure 5.11 A (black curve) and D (red curve) are displayed depending on the number of electrons per Pt atom. For A an increasing tendency for increasing occupation number can be clearly observed, although there are fluctuations after 10.5 electrons. In [67] the Heisenberg exchange coupling parameter J was examined for a material consisting of two sorts of atoms with a number of localized electrons N_1 and N_2. Depending on these numbers N_1 and N_2 the Heisenberg exchange coupling parameter was displayed, which tendencies resemble the behaviour of A depending on the occupation number.

For the DM-constant D it is difficult to determine a tendency, due to the aforementioned numerical problems, which can be also observed in the large estimated errors on D. Nevertheless there seems to be a sign change of D for larger occupation numbers,

[3]The band filling is enforced by the local charge neutrality constraint during the self consistent calculation to obtain an appropriate starting density for the force theorem.

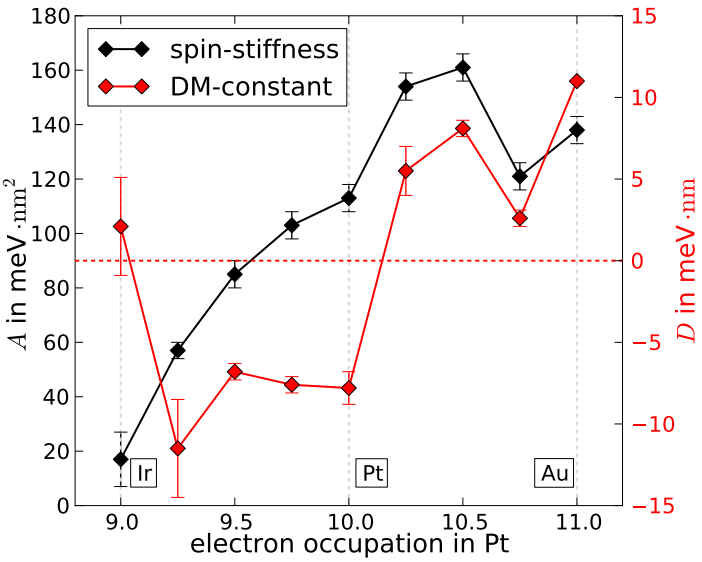

Figure 5.11: Spin stiffness A (black curve) and DM-constant D (red curve) of an Fe/Pt(001) slab, consisting of 9 layers Pt, depending on the valence electron number of the Pt atoms. The error-bars show the roughly estimated errors for A and D (see text).

which would lead to an interesting possibility to switch the rotation sense of a spin-spiral. Surprisingly the SOC-contribution to the band energy looks much smoother for larger occupation numbers than 10, which is reflected in the smaller errors of D. This is an indication, that the numerical problems are based on the relative position between the d-orbitals of Pt and the Fermi energy. Therefore the numerical problems vanish, if the Fermi energy lies above the d-states.

To conclude we have to face some numerical problems to treat the DMI in Fe/Pt slabs, which makes the predictions for the DMI in these systems not completely reliable. Nevertheless some results show an expected behaviour, which would justify a deeper examination via *ab-initio* codes or via an improved tight-binding scheme. The sign change in the DM-constant D within changing the electron occupation number is an appropriate starting point to gain a deeper understanding of the DMI. The results for the spin-stiffness constant A, for which we do not have to face these numerical problems, seem to be reliable.

5.4 Numerical aspects

Calculating complex magnetic structures is computationally very challenging. Usually very small energy differences have to be resolved, which makes it necessary to use a dense k-mesh and small Fermi broadening. Therefore one has to deal with large computational times and difficulties to obtain converged results. Of course the tight-binding method has the same problems, but due to its simplicity the computational time is drastically re-

n_{Layer}	3	5	7	9	11	13
t (in min)	1.0	2.5	5.0	8.0	12.5	17.0

Table 5.2: The time t is the computational time for one iteration of a self-consistent calculation for the ferromagnetic structure of an Fe/Pt slab with n_{Layer} Pt(111) layers ($N_{\text{at}} = n_{\text{Layer}} + 1$). For this calculation $N_k = 6400$ k-points were used and the calculations were performed on 1 CPU.

duced compared to *ab-initio* methods. In this section the computational time needed by the tight-binding method is analysed and compared to some *ab-initio* methods. We will also discuss the improvements, which can be included into the program. This includes the discussion about some remaining numerical problems of the tight-binding method and the present status of our code.

5.4.1 Computational time

One of the biggest advantages of the tight-binding method is its simplicity and therefore the reduction of the computational time compared to *ab-initio* methods. Before we present values of the computational time, we should analyse which numerical steps take the most part of the computational time. Roughly one can say, that diagonalizing the Hamiltonian $\mathcal{H}$ and the calculation of the expressions $\underline{\boldsymbol{S}}(\boldsymbol{k}) \cdot \boldsymbol{\Psi}_n(\boldsymbol{k})$ (see eq. 2.35) take almost the whole computational time. The DOS-calculation needs also some time, but it will be not considered in the following. If we consider each iteration step, there are two important parameters, which have a strong influence on the computational time. These are the number of basis atoms N_{at} in the system and the number of k-points N_k. The computational time for diagonalizing $\mathcal{H}$ is proportional to $N_{\text{at}}^3 \cdot N_k$, whereas the matrix vector multiplication scales with $N_{\text{at}}^2 \cdot N_k$. Therefore one should try to define the unit cell of the system as small as possible and using more k-points instead (e.g. the red unit cell in figure 5.1 instead of the blue one).

In table 5.2 the computational times for one iteration step in a calculation for the total energy of Fe/Pt slabs consisting of one monolayer Fe and n_{Layer} of Pt with (111) as crystallographic orientation, are presented. Compared to *ab-initio* methods, the tight-binding method is much faster. For example an FLAPW-calculation[4] (with the massively parallelized FLEUR code [56]) of a Cr/W(110)-slab with 7 layers of W takes about 6 minutes per iteration using 512 k-points on 16 CPUs. Therefore in a rough estimation the tight-binding calculation is about two orders faster than FLAPW.

The code, which is based on the tight-binding scheme, is not MPI-parallelized yet, therefore the advantage in the computational time could be strengthened to treat very large systems on state-of-the-art computers. The parallelization could be easily applied

[4]The calculation was performed by B. Zimmermann with following computational parameters: $l_{\max} = 6$, $k_{\max} = 3.8$.

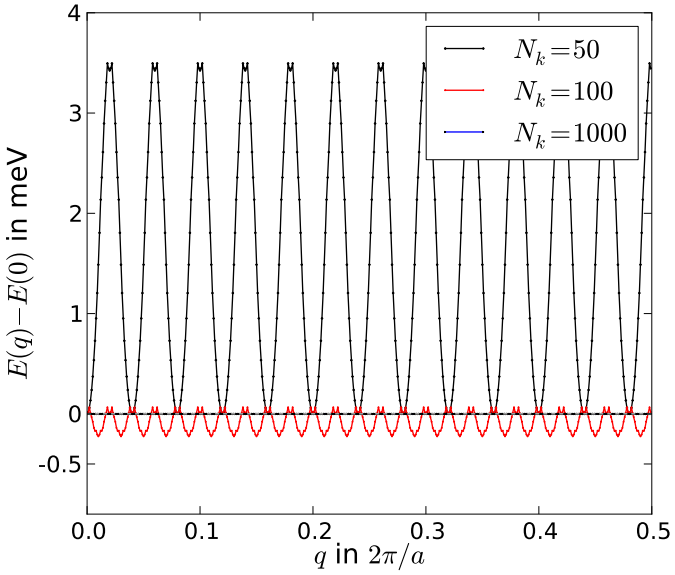

Figure 5.12: Magnon dispersion of a free standing mono-atomic Fe chain ($a = 2.22\,\text{Å}$) for a cone angle of $\Theta = 0°$ depending on the number of k-points N_k. All curves show an oscillatory behaviour due to numerical reasons, but the oscillations for $N_k = 1000$ are too small to see on this scale.

to the k-points in the diagonalization of $\mathcal{H}$ and the energies ε for the DOS-calculation $D(\varepsilon)$. This parallelization would also solve a memory-storage problem of the code, due to the eigenvectors, which occupy a huge amount of memory space. There is already the possibility to write the eigenvectors on the hard-disc, but this will drastically increase the computational time.

5.4.2 Numerical problems of the tight-binding method and the code

Numerical noise in spin-spiral calculations: As is known, one always has to take care of using enough k-points in the calculations. A remarkable "effect", which arises due to not enough k-points, is displayed in figure 5.12. In this figure the magnon dispersion of a spin-spiral for a free standing mono-atomic Fe chain with a cone angle of $\Theta = 0°$ is displayed for different number of k-points. For a spin-spiral with a cone angle of $\Theta = 0°$, we expect no dispersion. But depending on the number of k-points, we obtain an oscillatory behaviour with an amplitude, which is strongly decreasing for increased k-point number. Therefore it is clear, that the oscillations are numerical. Using a large number of k-points guarantees that the amplitude of the oscillations is much smaller than the energy differences between neighbouring q-points in the magnon dispersion. Unfortunately these oscillations obey no simple equation, so that one can not simply subtract the oscillations for $\Theta = 0°$ from the actual spin-spiral calculation to avoid the usage of a dense k-mesh. This problem appears also in the FLAPW-method and is

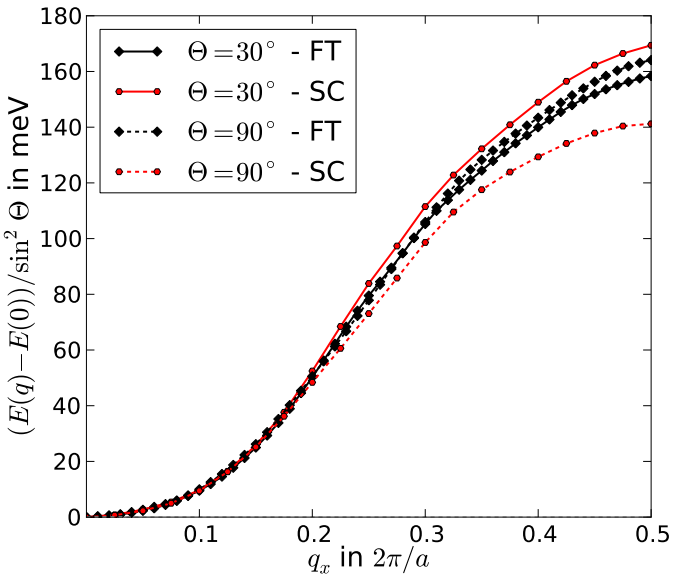

Figure 5.13: Magnon dispersions of an Fe/Pt(001) slab containing of 3 layers Pt. The black curves are calculations performed with the force theorem (FT), whereas the red curves present the results for a self-consistent (SC) calculation. The solid lines are calculations with $\Theta = 30°$, where the constraint becomes necessary for the SC calculation, whereas the dotted lines are calculations with $\Theta = 90°$. All curves are in pretty nice agreement especially for smaller q-values like in the case for bcc-Fe (see figure 3.7). Therefore the constraint is working well, if the system converges.

discussed in [12].

Problem with MKL-library: In this work the following library[5] is used to take advantage of increasing the number of threads to speed up the calculations. Depending on the size of the system, one can face a various amount of problems when using more than one thread with this library. Therefore to be sure a test calculation with OMP_NUM_THREADS = 1 should be performed for each system.

Problems with the constraint for the magnetic moments: The constraint in eq. 2.73 is used to fix the Θ-angle of a magnetic moment $\boldsymbol{m}$, which is the angle between the z-axis and $\boldsymbol{m}$. Fixing magnetic moments becomes necessary for self-consistent calculations, e.g. when the magnetic moments should not point along high-symmetry directions. If the magnetic moments are not too small and the structure is not too complex, the constraint method is working well. For very small magnetic moments ($|\boldsymbol{m}| \leq 0.1\,\mu_B$) however, the constraint is not able to properly fix them. This is no problem, as long as the system converges (cf. in figure 5.13), because the small magnetic moments do not have a large influence on the energy. But sometimes the convergence fails due to

[5] 64-bit version of the Math Kernel Library (Version: 11.1.059)

the small magnetic moments, because they will change their direction in every iteration step. To avoid this, one can set the small magnetic moments rigorously to zero or pin them after each iteration step into the desired direction, but this is not really a satisfying solution.

Another problem appears for calculations of highly complex magnetic structures, in which the constraint should fix all magnetic moments. It should be mentioned, that the constraint of the form 2.73 is not able to pin the magnetic moments exactly, but only for a small region around the desired direction. As a consequence, it is very difficult to obtain convergence, if the system is too complex.

Another constraint in form of a magnetic field along the desired direction of the magnetic moment instead of a perpendicular one (as in eq. 2.73) could perhaps solve these problems.

6 Conclusions

We report the development of a parametrized tight-binding code able to treat complex magnetic structures including the effect of spin-orbit coupling (SOC). The most obvious advantage of this method compared to *ab-initio* techniques is the reduction of the computational time, which allows to perform many calculations with different setups in a short time. In addition, the parametrization within this tight-binding method allows to perform "numerical experiments" in a simple way, in order to gain a deeper understanding of the physics behind the complex magnetic structures. Our parametrized tight-binding method is based on the NRL-TB parametrization scheme [15, 16, 17, 18], but also allows the possibility to use alternative parametrizations, e.g. considering only nearest-neighbour hoppings to simplify the model at the expense of accuracy. The magnetism is described via a Stoner model [19, 20], which allows to control the magnitude of the magnetic moments by tuning the Stoner parameters. Within this Stoner model the code is able to calculate charges self-consistently. In doing so, a constraint assures local charge neutrality, but the constraint can be also used to adjust the charges to desired values. SOC is considered by implementing a SOC matrix in the basis of localized atomic orbitals of each atom, which depends on SOC-parameters allowing to adjust the SOC strength. The treatment of non-collinear magnetism also includes the possibility to use the generalized Bloch theorem [21, 22, 23] for spin-spiral calculations. Using the 1st-order perturbation theoretical approach for SOC [24, 9], we are able to consider the effect of SOC within the generalized Bloch theorem.

The results of the thesis demonstrate that the parametrized tight-binding method can be successfully used to describe the behaviour of various structures at least qualitatively correctly.

In this thesis we have focused on systems consisting of Fe and Pt atoms. First, we have considered pure Fe systems within the tight-binding method and compared the results to *ab-initio* calculations. As long as one does not need an extremely accurate description of the electronic structure, the conventional Fe parameter sets provide good grounds for the description of magnetism in various Fe systems. For example the distance dependence of the Heisenberg exchange-coupling parameters of bcc-Fe is in a nice qualitative agreement with corresponding *ab-initio* results. And although the tight-binding parameters are not fitted for the description of free standing Fe monolayers and free standing Fe chains, the results for these systems also show a reasonable behaviour. The calculation of the magneto-crystalline anisotropy energy (MCA) in Fe monolayers of different crystallographic orientations yielded the same tendencies as the *ab-initio* values. This demonstrates that the tight-binding method is able to successfully describe such delicate properties as the MCA.

To treat Fe/Pt systems, it was necessary to determine the SOC-parameters and the

Stoner parameters of Pt. This was done by fitting to *ab-initio* results. An appropriate SOC-splitting in the band structure of fcc-Pt was used to determine the SOC-parameters. To fix the Stoner parameter the lattice constant dependence of the magnetic moments in fcc-Pt from an FLAPW calculation was compared to corresponding tight-binding results. The method to determine the Pt Stoner parameter exhibits some difficulties (see section 5.3.2 for more details), which should be solved in the future to improve the accuracy of the magnetic description within the tight-binding method.

We have investigated magnetic properties of complex structures consisting of Fe and Pt atoms, starting with the MCA of the $L1_0$-FePt structure and its dependence on the degree of uniaxiality, i. e. the $\frac{c}{a}$-ratio. The MCA is increasing with increasing $\frac{c}{a}$-ratio, which is in a nice qualitative agreement with corresponding *ab-initio* results [62, 65]. However, we have observed that the parametrization of binary systems within eq. 2.24 and 2.25 is not accurate enough to predict quantitatively reliable results for such delicate quantities as the MCA. In fact the on-site element parametrization via eq. 2.24 is only intended for describing systems consisting of one chemical atom type and therefore by changing already the parameter λ the MCA of the $L1_0$ system can change by 100%. Nevertheless the tendencies of the MCA are well reproduced within this parametrization.

The Dzyaloshinskii-Moriya interaction (DMI) has been examined in this thesis for Fe overlayers on Pt and Fe/Pt zigzag chains. Although the Fe/Pt zigzag chain is a strongly idealized model one can learn a lot about the DMI in this system due to its simplicity. In this work the 1st-order perturbation theoretical approximation of SOC in the framework of the generalized Bloch theorem has been compared to a full SOC treatment in a large supercell of an Fe/Pt zigzag chain to evaluate the validity of this approximation. It turns out that the approximation is sufficient to determine the strength of the DMI around a small region of the spin-spiral vector $q = 0$. This small region is the relevant region for computing the DM-constant D and the spin-stiffness constant A of the micro-magnetic model. These constants have been calculated for Fe/Pt(001) layers with varying number of Pt layers. For the spin-stiffness constant a convergence concerning the number of layers could be observed, whereas the convergence was difficult to achieve for D, possibly due to effects of quantum confinement. This fact is also reflected in the layer-decomposed analysis of the DMI in which a large contribution was found to be coming from the farthest-from-Fe layer of Pt. Therefore additional calculations of Fe/Pt layers with a larger number of Pt layers or investigations of symmetric Fe/Pt layers would be desirable.

Technically the calculation of the DMI in Fe/Pt layers presented some difficulties concerning the number of k-points necessary to obtain a smooth DM-contribution as a function of q. These difficulties seem to be based on the relative position of the d-orbitals and the Fermi energy. A k-point parallelization of the code would allow to increase the number of k-points without a drastic increase in the computational time. Additionally, the tetrahedron method [68] could be applied in order to improve the k-point convergence.

The spin-stiffness and the DMI dependence on the Stoner parameter and the electronic occupation number has been also examined in these systems. The possibility to perform calculations of these type is one of the most important advantages of the tight-binding method. The order of magnitude of the spin-stiffness constant with about $100\,\mathrm{meV}\cdot$

nm^2 and the DM-constant with about $10\,meV \cdot nm$ are comparable to the values in 2Fe/W(110) [8, 9] and Cr/W(110) [12] systems. The spin-stiffness constant increases with increasing Stoner parameter and with increasing occupation number, which is an expected behaviour. The strength of the DMI increases monotonously with increasing Stoner parameter as long as the Stoner parameter does not exceed the value for which the Pt atoms become intrinsically magnetic. In the case of a larger Stoner parameter the strength of the DMI drastically decreases. The DMI dependence on the occupation number shows a rather interesting sign change from an Fe/Pt layer to an Fe/Au-like layer. Understanding this behaviour could be a keystone for a better understanding of the DMI in this type of systems.

A Appendix

A.1 Angular moment operator in atomic orbital representation

Calculating the angular moment operator $\boldsymbol{L} = \boldsymbol{r} \times \boldsymbol{p}$ in representation of the atomic orbitals $|\mu\rangle$ is done straight forward by using the following equations for L_z and the ladder operators $L_\pm$:

$$L_z \cdot |l, m\rangle = m \cdot |l, m\rangle \tag{A.1}$$

$$L_\pm \cdot |l, m\rangle = \sqrt{l \cdot (l+1) - m \cdot (m \pm 1)} \cdot |l, m \pm 1\rangle \ , \tag{A.2}$$

where $|l, m\rangle$ are the eigenfunctions of L^2 and L_z, which are the complex spherical harmonics in real space representation.

With $L_x = \frac{1}{2} \cdot (L_+ + L_-)$ and $\mathrm{i} \cdot L_y = \frac{1}{2} \cdot (L_+ - L_-)$ we derive the following expressions for the angular moment in atomic orbital representation $(s, p_x, p_y, p_z, d_{xy}, d_{xz}, d_{yz}, d_{x^2-y^2}, d_{z^2})$:

$$[\underline{\boldsymbol{L_x}}]^\nu_\mu = \begin{pmatrix} 0 & 0 & 0 & 0 & 0 & 0 & 0 & 0 & 0 \\ 0 & 0 & 0 & 0 & 0 & 0 & 0 & 0 & 0 \\ 0 & 0 & 0 & -\mathrm{i} & 0 & 0 & 0 & 0 & 0 \\ 0 & 0 & \mathrm{i} & 0 & 0 & 0 & 0 & 0 & 0 \\ 0 & 0 & 0 & 0 & 0 & -\mathrm{i} & 0 & 0 & 0 \\ 0 & 0 & 0 & 0 & \mathrm{i} & 0 & 0 & 0 & 0 \\ 0 & 0 & 0 & 0 & 0 & 0 & 0 & -\mathrm{i} & -\mathrm{i}\sqrt{3} \\ 0 & 0 & 0 & 0 & 0 & 0 & \mathrm{i} & 0 & 0 \\ 0 & 0 & 0 & 0 & 0 & 0 & \mathrm{i}\sqrt{3} & 0 & 0 \end{pmatrix} \tag{A.3}$$

$$[\underline{\boldsymbol{L_y}}]^\nu_\mu = \begin{pmatrix} 0 & 0 & 0 & 0 & 0 & 0 & 0 & 0 & 0 \\ 0 & 0 & 0 & \mathrm{i} & 0 & 0 & 0 & 0 & 0 \\ 0 & 0 & 0 & 0 & 0 & 0 & 0 & 0 & 0 \\ 0 & -\mathrm{i} & 0 & 0 & 0 & 0 & 0 & 0 & 0 \\ 0 & 0 & 0 & 0 & 0 & 0 & \mathrm{i} & 0 & 0 \\ 0 & 0 & 0 & 0 & 0 & 0 & 0 & -\mathrm{i} & \mathrm{i}\sqrt{3} \\ 0 & 0 & 0 & 0 & -\mathrm{i} & 0 & 0 & 0 & 0 \\ 0 & 0 & 0 & 0 & 0 & \mathrm{i} & 0 & 0 & 0 \\ 0 & 0 & 0 & 0 & 0 & -\mathrm{i}\sqrt{3} & 0 & 0 & 0 \end{pmatrix} \tag{A.4}$$

$$[\underline{\boldsymbol{L_z}}]_\mu^\nu = \begin{pmatrix} 0 & 0 & 0 & 0 & 0 & 0 & 0 & 0 & 0 \\ 0 & 0 & -\mathrm{i} & 0 & 0 & 0 & 0 & 0 & 0 \\ 0 & \mathrm{i} & 0 & 0 & 0 & 0 & 0 & 0 & 0 \\ 0 & 0 & 0 & 0 & 0 & 0 & 0 & 0 & 0 \\ 0 & 0 & 0 & 0 & 0 & 0 & 0 & 2\mathrm{i} & 0 \\ 0 & 0 & 0 & 0 & 0 & 0 & -\mathrm{i} & 0 & 0 \\ 0 & 0 & 0 & 0 & 0 & \mathrm{i} & 0 & 0 & 0 \\ 0 & 0 & 0 & 0 & -2\mathrm{i} & 0 & 0 & 0 & 0 \\ 0 & 0 & 0 & 0 & 0 & 0 & 0 & 0 & 0 \end{pmatrix} \tag{A.5}$$

To obtain the SOC-matrix in atomic orbital representation, one has to use the equation

$$\mathcal{H}_{\mathrm{SOC}} \propto \boldsymbol{L} \cdot \boldsymbol{S} \tag{A.6}$$

with $\boldsymbol{S} = \frac{\hbar}{2} \cdot \boldsymbol{\sigma}$.

A.2 Derivation of the phase factors

The Bloch-waves

$$|\Phi_{i\mu}^{\uparrow}(\boldsymbol{k})\rangle = \frac{1}{\sqrt{N}} \cdot \sum_n \mathrm{e}^{\mathrm{i}\boldsymbol{k}\cdot(\boldsymbol{R}_n+\boldsymbol{\tau}_i)} \cdot |\boldsymbol{n}, i, \mu\rangle \cdot \begin{pmatrix} \mathrm{e}^{-\frac{\mathrm{i}}{2}\boldsymbol{q}\cdot(\boldsymbol{R}_n+\boldsymbol{\tau}_i)} \cdot \cos\frac{\Theta}{2} \\ \mathrm{e}^{\frac{\mathrm{i}}{2}\boldsymbol{q}\cdot(\boldsymbol{R}_n+\boldsymbol{\tau}_i)} \cdot \sin\frac{\Theta}{2} \end{pmatrix} \tag{A.7}$$

$$|\Phi_{i\mu}^{\downarrow}(\boldsymbol{k})\rangle = \frac{1}{\sqrt{N}} \cdot \sum_n \mathrm{e}^{\mathrm{i}\boldsymbol{k}\cdot(\boldsymbol{R}_n+\boldsymbol{\tau}_i)} \cdot |\boldsymbol{n}, i, \mu\rangle \cdot \begin{pmatrix} -\mathrm{e}^{-\frac{\mathrm{i}}{2}\boldsymbol{q}\cdot(\boldsymbol{R}_n+\boldsymbol{\tau}_i)} \cdot \sin\frac{\Theta}{2} \\ \mathrm{e}^{\frac{\mathrm{i}}{2}\boldsymbol{q}\cdot(\boldsymbol{R}_n+\boldsymbol{\tau}_i)} \cdot \cos\frac{\Theta}{2} \end{pmatrix} \tag{A.8}$$

satisfy the generalized Bloch theorem [21, 22, 23] and they form an orthonormalized set of basis functions. The Hamiltonian displays as follows in representation of these Bloch waves:

$$\langle \boldsymbol{\Phi}_{i,\mu}^{\sigma} | \, \mathcal{H} \, | \boldsymbol{\Phi}_{j,\nu}^{\sigma'} \rangle = \frac{1}{N} \sum_{n,n'} \mathrm{e}^{\mathrm{i}\boldsymbol{k}\cdot(\boldsymbol{R}_n+\boldsymbol{\tau}_j-\boldsymbol{R}_{n'}-\boldsymbol{\tau}_i)} \cdot (\tilde{\boldsymbol{\chi}}_{n',i,\mu}^{\sigma})^{\dagger} \cdot (H_{i,\mu}^{j,\nu})^{\sigma\sigma'}(\boldsymbol{R}_{n'} - \boldsymbol{R}_n) \cdot \tilde{\boldsymbol{\chi}}_{n,j,\nu}^{\sigma'}$$

with

$$\begin{aligned} \tilde{\boldsymbol{\chi}}_{n,i,\mu}^{\sigma} &= \mathcal{U} \cdot \boldsymbol{\chi}_{n,i,\mu}^{\sigma} \\ &= \begin{cases} \begin{pmatrix} \mathrm{e}^{(-\mathrm{i}/2\cdot\boldsymbol{q}\cdot(\boldsymbol{R}_n+\boldsymbol{\tau}_i)} \cdot \cos(\Theta/2) \\ \mathrm{e}^{(\mathrm{i}/2\cdot\boldsymbol{q}\cdot(\boldsymbol{R}_n+\boldsymbol{\tau}_i))} \cdot \sin(\Theta/2) \end{pmatrix} & \text{if } \sigma = \uparrow \\ \begin{pmatrix} -\mathrm{e}^{(-i/2\cdot\boldsymbol{q}\cdot(\boldsymbol{R}_n+\boldsymbol{\tau}_i)} \cdot \sin(\Theta/2) \\ \mathrm{e}^{(\mathrm{i}/2\cdot\boldsymbol{q}\cdot(\boldsymbol{R}_n+\boldsymbol{\tau}_i))} \cdot \cos(\Theta/2) \end{pmatrix} & \text{if } \sigma = \downarrow \end{cases}, \end{aligned} \tag{A.9}$$

where $\mathcal{U}$ is the spin transformation matrix from eq. 2.66 with $\phi = \boldsymbol{q} \cdot (\boldsymbol{R}_n + \boldsymbol{\tau}_i)$. The χ^{σ} are the $\uparrow$- and $\downarrow$-spins in the global frame, therefore $(1,0)^{\mathrm{T}}$ and $(0,1)^{\mathrm{T}}$. Therefore it holds:

$$
\begin{aligned}
(H^{j,\nu}_{i,\mu})^{\sigma\sigma'}(\boldsymbol{k},\boldsymbol{q}) &= \frac{1}{N}\cdot\sum_{n,n'} \mathrm{e}^{\mathrm{i}\boldsymbol{k}\cdot(\boldsymbol{R}_n+\boldsymbol{\tau}_j-\boldsymbol{R}_{n'}-\boldsymbol{\tau}_i)}\cdot(\boldsymbol{\chi}^{\sigma}_{n',i,\mu})^{\dagger}\cdot[\mathcal{U}^{\dagger}(\Theta,\boldsymbol{q}\cdot(\boldsymbol{R}_{n'}+\boldsymbol{\tau}_i))\cdot \\
&\quad (H^{j,\nu}_{i,\mu})^{\sigma\sigma'}(\boldsymbol{R}_{n'}-\boldsymbol{R}_n)\cdot\mathcal{U}(\Theta,\boldsymbol{q}\cdot(\boldsymbol{R}_n+\boldsymbol{\tau}_j))]\cdot(\boldsymbol{\chi}^{\sigma'}_{n,j,\nu}). \qquad \text{(A.10)}
\end{aligned}
$$

$\mathcal{H}_0$ and $\mathcal{H}_{\mathrm{LCN}}$ is proportional to the unit matrix in spin-space. With $t_{i,\mu\to j,\nu}(\boldsymbol{R}_{n'}-\boldsymbol{R}_n)$ the hopping element of the Hamiltonian from the state i,μ to the state j,ν, it holds due to the independence of the hopping elements of the spin:

$$
[H_0]^{j\nu}_{i\mu} = \begin{pmatrix} t_{i,\mu\to j,\nu} & 0 \\ 0 & t_{i,\mu\to j,\nu}\end{pmatrix}.
$$

The magnetic part $\mathcal{H}_{\mathrm{mag}}$ in global presentation transforms into the local frame due to the spin transformation 2.69. In this local frame the magnetic part of the Hamiltonian is also diagonal in spin space. Therefore the expression $\mathcal{U}^{\dagger}(\Theta,\boldsymbol{q}\cdot(\boldsymbol{R}_{n'}+\boldsymbol{\tau}_i))\cdot\mathcal{U}(\Theta,\boldsymbol{q}\cdot(\boldsymbol{R}_n+\boldsymbol{\tau}_j))$ yields the specific phase-factors $(s^j_i(\boldsymbol{q}\cdot\boldsymbol{R}_n))^{\sigma\sigma'}$:

$$
\begin{aligned}
(s^j_i(\boldsymbol{q}\cdot\boldsymbol{R}_n))^{\uparrow\uparrow} &= \mathrm{e}^{-\mathrm{i}\frac{\boldsymbol{q}}{2}\cdot(\boldsymbol{R}_n+\boldsymbol{\tau}_j-\boldsymbol{\tau}_i)}\cdot\cos^2\left(\frac{\Theta}{2}\right)+\mathrm{e}^{\mathrm{i}\frac{\boldsymbol{q}}{2}\cdot(\boldsymbol{R}_n+\boldsymbol{\tau}_j-\boldsymbol{\tau}_i)}\cdot\sin^2\left(\frac{\Theta}{2}\right) \\
(s^j_i(\boldsymbol{q}\cdot\boldsymbol{R}_n))^{\downarrow\downarrow} &= \mathrm{e}^{\mathrm{i}\frac{\boldsymbol{q}}{2}\cdot(\boldsymbol{R}_n+\boldsymbol{\tau}_j-\boldsymbol{\tau}_i)}\cdot\cos^2\left(\frac{\Theta}{2}\right)+\mathrm{e}^{-\mathrm{i}\frac{\boldsymbol{q}}{2}\cdot(\boldsymbol{R}_n+\boldsymbol{\tau}_j-\boldsymbol{\tau}_i)}\cdot\sin^2\left(\frac{\Theta}{2}\right) \\
(s^j_i(\boldsymbol{q}\cdot\boldsymbol{R}_n))^{\uparrow\downarrow} &= 2\mathrm{i}\cdot\sin\left(\frac{\boldsymbol{q}}{2}\cdot(\boldsymbol{R}_n+\boldsymbol{\tau}_j-\boldsymbol{\tau}_i)\right)\cdot\sin\left(\frac{\Theta}{2}\right)\cdot\cos\left(\frac{\Theta}{2}\right) \\
(s^j_i(\boldsymbol{q}\cdot\boldsymbol{R}_n))^{\downarrow\uparrow} &= [(s^j_i(\boldsymbol{q}\cdot\boldsymbol{R}_n))^{\uparrow\downarrow}]^* \qquad \text{(A.11)}
\end{aligned}
$$

For a spin-spiral of the type (c) in fig. 2.15, which has to be used to obtain non-vanishing DMI in the systems examined in chapter 5, the phase-factors are a little bit different. In an analogous way one can derive the phase factors for these "flat-spirals" as follows:

$$
\begin{aligned}
(s^j_i(\boldsymbol{q}\cdot\boldsymbol{R}_n))^{\uparrow\uparrow} &= \cos\left(\frac{\boldsymbol{q}}{2}\cdot(\boldsymbol{R}_n+\boldsymbol{\tau}_j-\boldsymbol{\tau}_i)\right) \\
(s^j_i(\boldsymbol{q}\cdot\boldsymbol{R}_n))^{\downarrow\downarrow} &= \cos\left(\frac{\boldsymbol{q}}{2}\cdot(\boldsymbol{R}_n+\boldsymbol{\tau}_j-\boldsymbol{\tau}_i)\right) \\
(s^j_i(\boldsymbol{q}\cdot\boldsymbol{R}_n))^{\uparrow\downarrow} &= -\sin\left(\frac{\boldsymbol{q}}{2}\cdot(\boldsymbol{R}_n+\boldsymbol{\tau}_j-\boldsymbol{\tau}_i)\right) \\
(s^j_i(\boldsymbol{q}\cdot\boldsymbol{R}_n))^{\downarrow\uparrow} &= [(s^j_i(\boldsymbol{q}\cdot\boldsymbol{R}_n))^{\uparrow\downarrow}]^* \qquad \text{(A.12)}
\end{aligned}
$$

H_s^s	$= V_{ss\sigma}$
H_s^x	$= lV_{sp\sigma}$
H_x^x	$= l^2V_{pp\sigma} + (1-l^2)V_{pp\pi}$
H_x^y	$= lmV_{pp\sigma} - lmV_{pp\pi}$
H_x^z	$= lnV_{pp\sigma} - lnV_{pp\pi}$
H_s^{xy}	$= \sqrt{3}lmV_{sd\sigma}$
$H_s^{x^2-y^2}$	$= \frac{1}{2}\sqrt{3}(l^2-m^2)$
$H_s^{z^2}$	$= \left[n^2 - \frac{1}{2}(l^2+m^2)\right] V_{sd\sigma}$
H_x^{xy}	$= \sqrt{3}l^2mV_{pd\sigma} + m(1-2l^2)V_{pd\pi}$
H_x^{yz}	$= \sqrt{3}lmnV_{pd\sigma} - 2lmnV_{pd\pi}$
H_x^{xz}	$= \sqrt{3}l^2nV_{pd\sigma} + n(1-2l^2)V_{pd\pi}$
$H_x^{x^2-y^2}$	$= \frac{1}{2}\sqrt{3}l(l^2-m^2)V_{pd\sigma} + l(1-l^2+m^2)V_{pd\pi}$
$H_y^{x^2-y^2}$	$= \frac{1}{2}\sqrt{3}m(l^2-m^2)V_{pd\sigma} - m(1+l^2-m^2)V_{pd\pi}$
$H_z^{x^2-y^2}$	$= \frac{1}{2}\sqrt{3}n(l^2-m^2)V_{pd\sigma} - n(l^2-m^2)V_{pd\pi}$
$H_x^{z^2}$	$= l\left[n^2 - \frac{1}{2}(l^2+m^2)\right] V_{pd\sigma} - \sqrt{3}ln^2V_{pd\pi}$
$H_y^{z^2}$	$= m\left[n^2 - \frac{1}{2}(l^2+m^2)\right] V_{pd\sigma} - \sqrt{3}mn^2V_{pd\pi}$
$H_z^{z^2}$	$= n\left[n^2 - \frac{1}{2}(l^2+m^2)\right] V_{pd\sigma} + \sqrt{3}n(l^2+m^2)V_{pd\pi}$
H_{xy}^{xy}	$= 3l^2m^2V_{dd\sigma} + (l^2+m^2-4l^2m^2)V_{dd\pi} + (n^2+l^2m^2)V_{dd\delta}$
H_{xy}^{yz}	$= 3lm^2nV_{dd\sigma} + ln(1-4m^2)V_{dd\pi} + ln(m^2-1)V_{dd\delta}$
H_{xy}^{xz}	$= 3l^2mnV_{dd\sigma} + mn(1-4l^2)V_{dd\pi} + mn(l^2-1)V_{dd\delta}$
$H_{xy}^{x^2-y^2}$	$= \frac{3}{2}lm(l^2-m^2)V_{dd\sigma} + 2lm(m^2-l^2)V_{dd\pi} + \frac{1}{2}lm(l^2-m^2)V_{dd\delta}$
$H_{yz}^{x^2-y^2}$	$= \frac{3}{2}mn(l^2-m^2)V_{dd\sigma} - mn\left[1+2(l^2-m^2)\right] V_{dd\pi} + mn\left[1+\frac{1}{2}(l^2-m^2)\right] V_{dd\delta}$
$H_{xz}^{x^2-y^2}$	$= \frac{3}{2}nl(l^2-m^2)V_{dd\sigma} + nl\left[1-2(l^2-m^2)\right] V_{dd\pi} - nl\left[1-\frac{1}{2}(l^2-m^2)\right] V_{dd\delta}$
$H_{xy}^{z^2}$	$= \sqrt{3}lm\left[n^2 - \frac{1}{2}(l^2+m^2)\right] V_{dd\sigma} - 2\sqrt{3}lmn^2V_{dd\pi} + \frac{1}{2}\sqrt{3}lm(1+n^2)V_{dd\delta}$
$H_{yz}^{z^2}$	$= \sqrt{3}mn\left[n^2 - \frac{1}{2}(l^2+m^2)\right] V_{dd\sigma} + \sqrt{3}mn(l^2+m^2-n^2)V_{dd\pi} - \frac{1}{2}\sqrt{3}mn(l^2+m^2)V_{dd\delta}$
$H_{xz}^{z^2}$	$= \sqrt{3}ln\left[n^2 - \frac{1}{2}(l^2+m^2)\right] V_{dd\sigma} + \sqrt{3}ln(l^2+m^2-n^2)V_{dd\pi} - \frac{1}{2}\sqrt{3}ln(l^2+m^2)V_{dd\delta}$
$H_{x^2-y^2}^{x^2-y^2}$	$= \frac{3}{4}(l^2-m^2)^2V_{dd\sigma} + \left[l^2+m^2-(l^2-m^2)^2\right] V_{dd\pi} + \left[n^2+\frac{1}{4}(l^2-m^2)^2\right] V_{dd\delta}$
$H_{x^2-y^2}^{z^2}$	$= \frac{1}{2}\sqrt{3}(l^2-m^2)\left[n^2 - \frac{1}{2}(l^2+m^2)\right] V_{dd\sigma} + \sqrt{3}n^2(m^2-l^2)V_{dd\pi}$
	$+\frac{1}{4}\sqrt{3}(1+n^2)(l^2-m^2)V_{dd\delta}$
$H_{z^2}^{z^2}$	$= \left[n^2 - \frac{1}{2}(l^2+m^2)\right]^2 V_{dd\sigma} + 3n^2(l^2+m^2)V_{dd\pi} + \frac{3}{4}(l^2+m^2)^2V_{dd\delta}$

Table A.1: Slater-Koster transformations for s, p and d-orbitals. The matrix elements $H_\mu^\nu(\boldsymbol{R}_n)$ of the real-space Hamiltonian depend on the direction cosines $l = \frac{(\boldsymbol{R}_n)_x}{|\boldsymbol{R}_n|}$, $m = \frac{(\boldsymbol{R}_n)_y}{|\boldsymbol{R}_n|}$ and $n = \frac{(\boldsymbol{R}_n)_z}{|\boldsymbol{R}_n|}$ of the bonding vector $\boldsymbol{R}_n$. The table is separated in s-s, s-p, p-p, s-d, p-d and d-d matrix elements by horizontal lines.

B Appendix

B.1 Parameter sets for Fe and Pt

The following parameter sets in the tables B.1, B.2 and B.3 are obtained by Mehl *et al.* by fitting the TB-bands to LDA/GGA-*ab-initio* band structures. The results are published in [15, 16, 54]. The parameters are necessary for the description of the Hamiltonian and the overlap matrix via eq. 2.21 and eq. 2.23.
Some informations about the parameters:

- The distance R is in atomic units and the Slater-Koster parameters are in Rydberg in the Mehl *et al.* parametrization. Therefore the parameters are in following units:

$$[a] = \text{Ry}, \quad [b] = \text{Ry} \cdot (\text{a.u.})^{-1}, \quad [c] = \text{Ry} \cdot (\text{a.u.})^{-2}, \quad [d] = (\text{a.u.})^{-0.5}$$

$$[\alpha] = \text{Ry}, \quad [\beta] = \text{Ry}, \quad [\gamma] = \text{Ry}, \quad [\chi] = \text{Ry}, \quad [\lambda] = (\text{a.u.})^{-0.5}\,.$$

- The on-site contributions for the overlap matrix are 1.0.
- The parameters c and χ are zero in some of the presented parameter sets, but in general they are not.
- No difference between the t_{2g}- and e_g-states is introduced in the parameter sets.
- The parametrization of the overlap matrix is via the old parametrization scheme of Mehl *et al.* [17].

$R_c = 16.5\,\text{a.u.} \quad L_c = 0.5\,\text{a.u.} \quad \lambda = 1.61591889336\text{E+}00$

orbital	α	β	γ	χ
s	3.13939258386E−01	-1.50340969449E+02	5.60131523543E+04	0.0
p	7.50228117251E−01	1.32173351946E+02	-4.83053227618E+03	0.0
d	6.79135670479E−02	1.80487939584E+01	-1.71453585941E+03	0.0

$V_{ll'm}$	a	b	c	d
$V_{ss\sigma}$	4.55043825222E−01	-1.21734123013E+00	0.0	9.14314863459E−01
$V_{sp\sigma}$	8.72706208251E−01	-2.65085983323E−03	0.0	6.78102167954E−01
$V_{pp\sigma}$	1.02661455604E+00	4.62878498635E−02	0.0	6.49770224489E−01
$V_{pp\pi}$	-3.61138626592E+01	8.18233539363E+00	0.0	1.17142147452E+00
$V_{sd\sigma}$	5.06145301841E−01	-3.03407375680E−01	0.0	8.23582443933E−01
$V_{pd\sigma}$	3.62443449178E+00	-1.20097178354E+00	0.0	8.70891888071E−01
$V_{pd\pi}$	-1.23170095125E+00	8.46861596670E−01	0.0	9.92415550868E−01
$V_{dd\sigma}$	-1.30200356145E+00	9.13566450579E−02	0.0	7.96761216755E−01
$V_{dd\pi}$	3.03158415211E+00	-2.29519971304E−01	0.0	9.29910152711E−01
$V_{dd\delta}$	-2.42866093686E+00	3.43810222548E−01	0.0	1.01267224138E+00

$V_{ll'm}$	a	b	c	d
$V_{ss\sigma}$	2.08691737655E+00	1.50951711074E+00	0.0	9.38172864034E−01
$V_{sp\sigma}$	6.61324794182E+00	-2.39708289279E+00	0.0	8.42816286968E−01
$V_{pp\sigma}$	7.79047201212E+00	-2.24565537971E+00	0.0	7.63650075929E−01
$V_{pp\pi}$	-5.28178851021E+00	1.65816689927E+00	0.0	8.02822184386E−01
$V_{sd\sigma}$	-6.29773771311E+02	1.71528662797E+02	0.0	1.30437406994E+00
$V_{pd\sigma}$	-3.79544838869E+00	7.64597367732E−01	0.0	8.45424416578E−01
$V_{pd\pi}$	1.21878943829E+02	-4.37849569870E+01	0.0	1.33895185420E+00
$V_{dd\sigma}$	-4.33296538382E+00	4.93979871821E+00	0.0	1.19874436110E+00
$V_{dd\pi}$	-1.03641263737E+00	1.93977003741E−01	0.0	8.98115322198E−01
$V_{dd\delta}$	4.62136029975E+00	-1.26354179980E+00	0.0	1.05391660677E+00

Table B.1: Fe LDA-parameter set: The first table contains the necessary parameters for the on-site energies, the second table contains the parameters for the Hamiltonian matrix elements (hopping elements), whereas the third table contains the parameters for the overlap matrix.

$R_c = 16.5\,\text{a.u.} \quad L_c = 0.5\,\text{a.u.} \quad \lambda = 0.167876018007\text{E+}01$

orbital	α	β	γ	χ
s	.111237776825E+00	.157472037798E+03	.279493598875E+06	-.886322891071E+08
p	.512530808853E+00	.305694624645E+03	-.627918805139E+05	-.526504629561E+07
d	.956141408199E−01	-.229757020621E+02	.131512865599E+05	-.854972223057E+06

$V_{ll'm}$	a	b	c	d
$V_{ss\sigma}$	.428297660344E+00	-.736375016998E+00	.242575588592E−02	.858600612943E+00
$V_{sp\sigma}$	.817564285855E+00	-.114712495851E−02	.571303916419E−02	.713729903579E+00
$V_{pp\sigma}$	-.624426913703E−01	.169380062153E+00	-.133925020299E−01	.531763011628E+00
$V_{pp\pi}$	.457554537257E+03	-.268469067026E+02	-.213983975589E+02	.146261128932E+01
$V_{sd\sigma}$	.490269004091E+00	-.381292939420E+00	-.236890354241E−02	.816265910951E+00
$V_{pd\sigma}$	.380280165519E+01	-.116865592373E+01	.245781494444E−02	.853580010894E+00
$V_{pd\pi}$	-.170292010391E+01	.789563902306E+00	-.347134872764E−01	.955500742639E+00
$V_{dd\sigma}$	-.112692175412E+01	.906852484661E−01	-.110402112411E−01	.811112962492E+00
$V_{dd\pi}$	.628847411766E+01	-.136259655000E+01	.979967718827E−01	.931326036079E+00
$V_{dd\delta}$	-.643123923582E+03	.359148848319E+03	-.546524202557E+02	.147480783649E+01

$V_{ll'm}$	a	b	c	d
$V_{ss\sigma}$	-.130030306848E+02	.373133347375E+01	.641105326253E+00	.102602926730E+01
$V_{sp\sigma}$	.105130415274E+02	-.357406235042E+01	-.229978575757E+00	.966897827380E+00
$V_{pp\sigma}$	.151286790032E+02	-.335893499630E+01	-.246789283219E+00	.849462577539E+00
$V_{pp\pi}$	-.255301615149E+01	.154908422778E+01	-.108991538227E+00	.758944165379E+00
$V_{sd\sigma}$	-.596211016918E+03	.158217370850E+03	-.132981350821E+01	.128158963555E+01
$V_{pd\sigma}$	-.520996890837E+01	.163409810874E+01	-.490336116995E−01	.762616604972E+00
$V_{pd\pi}$	-.449930772185E+02	-.114818134979E+02	-.313846669042E+01	.136886120058E+01
$V_{dd\sigma}$	.267625592154E+02	-.123743969604E+02	.154936323562E+01	.974949432957E+00
$V_{dd\pi}$	-.137179418998E+01	.163248717151E+00	.281060705718E−02	.717618717462E+00
$V_{dd\delta}$	.105113669588E+02	-.450600002662E+00	-.395000205694E+00	.101542781750E+01

Table B.2: Fe GGA-parameter set: The first table contains the necessary parameters for the on-site energies, the second table contains the parameters for the Hamiltonian matrix elements (hopping elements), whereas the third table contains the parameters for the overlap matrix.

$R_c = 16.5\,\text{a.u.} \quad L_c = 0.5\,\text{a.u.} \quad \lambda = 1.48637407133\text{E+}00$

orbital	α	β	γ	χ
s	5.83155590317E−03	2.05115875626E+02	-2.04104996463E+04	0.0
p	8.17822535174E−01	5.89749525600E+01	1.12389938450E+04	0.0
d	4.98287869238E−02	-4.47348238061E+00	6.15745074751E+02	0.0

$V_{ll'm}$	a	b	c	d
$V_{ss\sigma}$	-1.38284631122E+00	-1.20674487008E−01	0.0	8.13944927710E−01
$V_{sp\sigma}$	1.83353981972E+00	5.86126500009E−01	0.0	8.45134159397E−01
$V_{pp\sigma}$	1.26085142803E+00	1.03890170253E+00	0.0	8.31224712555E−01
$V_{pp\pi}$	2.05175594909E+02	-3.96379653812E+01	0.0	1.13164516026E+00
$V_{sd\sigma}$	-2.89294520731E+00	2.44945737996E−01	0.0	7.98201020712E−01
$V_{pd\sigma}$	1.58551087829E+00	-6.94618881904E−01	0.0	8.07843642691E−01
$V_{pd\pi}$	8.60594193094E−01	-3.28209927985E−02	0.0	8.59013576224E−01
$V_{dd\sigma}$	-1.75160317524E+00	-3.17276845523E−01	0.0	8.74768883496E−01
$V_{dd\pi}$	7.04207263761E+00	-3.61062702293E−01	0.0	9.55737743700E−01
$V_{dd\delta}$	-1.19554932632E+00	1.68459650181E−01	0.0	8.73327306708E−01

$V_{ll'm}$	a	b	c	d
$V_{ss\sigma}$	8.48032304726E+00	-1.21344187855E+00	0.0	8.73588630500E−01
$V_{sp\sigma}$	2.07665691775E+03	-4.87117198609E+02	0.0	1.42827779253E+00
$V_{pp\sigma}$	-1.59104408799E+04	3.39006655850E+03	0.0	1.46844841218E+00
$V_{pp\pi}$	-4.68565688171E+02	1.29049135927E+02	0.0	1.24800847008E+00
$V_{sd\sigma}$	-1.88027778797E+00	4.33067941947E−01	0.0	7.48675014457E−01
$V_{pd\sigma}$	1.40632324463E−01	-1.08623564920E−02	0.0	4.30679519174E−01
$V_{pd\pi}$	-2.32135126063E+00	3.29353331687E−01	0.0	7.81550208218E−01
$V_{dd\sigma}$	7.85664648549E−01	-4.01900709200E−02	0.0	7.02103011484E−01
$V_{dd\pi}$	-3.26443115027E+00	5.45024650243E−02	0.0	9.05925825725E−01
$V_{dd\delta}$	1.65626596755E+03	-2.95917301165E+02	0.0	1.32876007979E+00

Table B.3: Pt LDA-parameter set: The first table contains the necessary parameters for the on-site energies, the second table contains the parameters for the Hamiltonian matrix elements (hopping elements), whereas the third table contains the parameters for the overlap matrix.

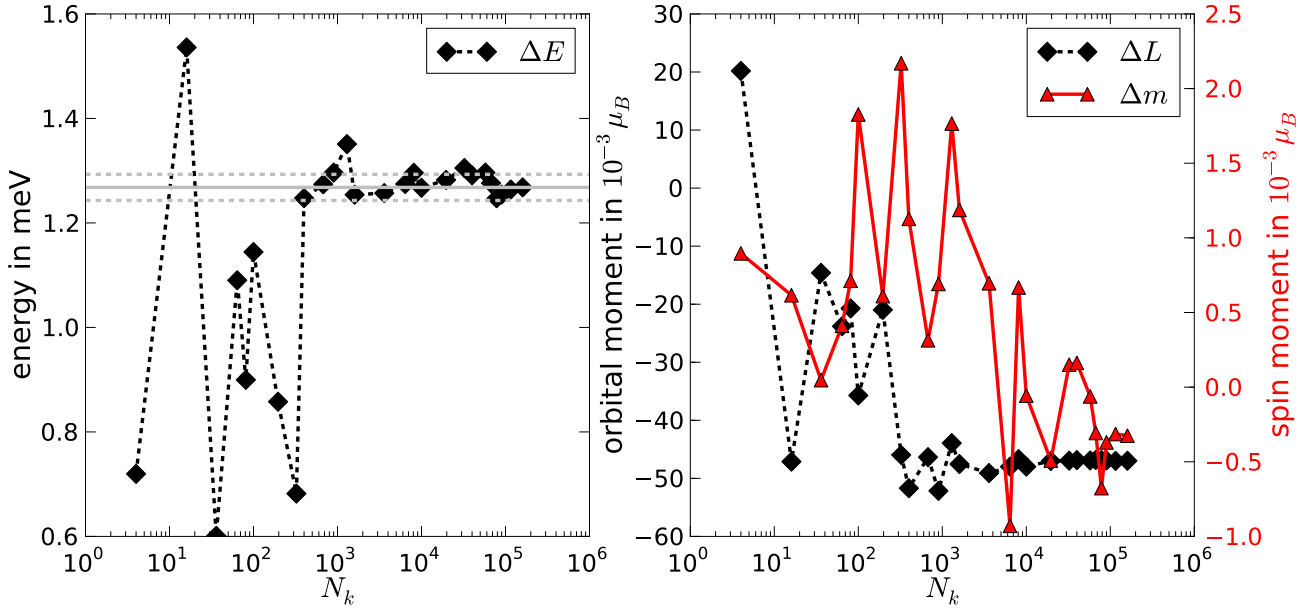

Figure B.1: Left panel: MCA $\Delta E = E_{\rightarrow} - E_{\uparrow}$ of a (001)-Fe monolayer depending on the number of k-points N_k. The Fermi smearing is about 1 meV. Right panel: Difference in the magnetic moments $\Delta m = m_{\rightarrow} - m_{\uparrow}$ (red curve) and orbital moments $\Delta L = L_{\rightarrow} - L_{\uparrow}$ (black curve) depending on the number of k-points. $\uparrow$ stands for out-of-plane magnetization and $\rightarrow$ stands for in-plane magnetization.

B.2 Convergence of the MCA

In this section the convergence of the MCA with the number of k-points is examined using the example of a (001)-Fe monolayer. In the left panel of figure B.1 one can clearly observe that the MCA is converged to regions of about 0.1 meV for more than 1000 k-points. In the right panel of figure B.1 the difference $m_{\rightarrow} - m_{\uparrow}$ between the magnetic moment for out-of-plane magnetization $m_{\uparrow}$ and for in-plane magnetization $m_{\rightarrow}$ and the difference in the orbital moments $L_{\rightarrow} - L_{\uparrow}$ depending on the number of k-points are displayed. The difference in the magnetic moments is very small with an order of about $10^{-4}\,\mu_B$, therefore the convergence with the number of k-points is not as obvious as for the orbital moment. In section 3.4 we have chosen 40000 k-points for the MCA-calculation of the Fe monolayers, therefore the MCA with the corresponding moments is sufficiently converged for our purposes.

Bibliography

[1] P. Grünberg, R. Schreiber, Y. Pang, M. B. Brodsky, and H. Sowers, Layered Magnetic Structures: Evidence for Antiferromagnetic Coupling of Fe Layers across Cr Interlayers, Phys. Rev. Lett. **57**(19), 2442–2445 (Nov 1986).

[2] M. N. Baibich, J. M. Broto, A. Fert, F. N. Van Dau, F. Petroff, P. Etienne, G. Creuzet, A. Friederich, and J. Chazelas, Giant Magnetoresistance of (001)Fe/(001)Cr Magnetic Superlattices, Phys. Rev. Lett. **61**(21), 2472–2475 (Nov 1988).

[3] T. Moriya, Anisotropic Superexchange Interaction and Weak Ferromagnetism, Phys. Rev. **120**(1), 91–98 (1960).

[4] I. E. Dzyaloshinskii, Thermodynamic theory of "weak" ferromagnetism in antiferromagnetic substances, Sov. Phys. JETP **5**(1259) (1957).

[5] S. Blügel, Exchange interactions, in *Lecture Notes of the 41st Springschool 2010: Electronic Oxides - Correlation Phenomena, Exotic Phases and Novel Functionalities*, edited by S. Blügel, T. Brückel, R. Waser, and C. M. Schneider, Schriften des Forschungszentrums Jülich Reihe Schlüsseltechnologien, 2010.

[6] A. Kubetzka, M. Bode, O. Pietzsch, and R. Wiesendanger, Spin-Polarized Scanning Tunneling Microscopy with Antiferromagnetic Probe Tips, Phys. Rev. Lett. **88**(5), 057201 (Jan 2002).

[7] S. Meckler, N. Mikuszeit, A. Preßler, E. Y. Vedmedenko, O. Pietzsch, and R. Wiesendanger, Real-Space Observation of a Right-Rotating Inhomogeneous Cycloidal Spin Spiral by Spin-Polarized Scanning Tunneling Microscopy in a Triple Axes Vector Magnet, Phys. Rev. Lett. **103**, 157201 (2009).

[8] M. Heide, G. Bihlmayer, and S. Blügel, Dzyaloshinskii-Moriya interaction accounting for the orientation of magnetic domains in ultrathin films: Fe/W(110), Phys. Rev. B **78**(14), 140403 (Oct 2008).

[9] M. Heide, *Magnetic domain walls in ultrathin films: Contribution of the Dzyaloshinskii-Moriya interaction*, PhD thesis, RWTH Aachen, 2006.

[10] M. Bode, S. Heinze, A. Kubetzka, O. Pietzsch, M. Hennefarth, M. Getzlaff, R. Wiesendanger, X. Nie, G. Bihlmayer, and S. Blügel, Structural, electronic, and magnetic properties of a Mn monolayer on W(110), Phys. Rev. B **66**(1), 014425 (Jul 2002).

[11] M. Bode, M. Heide, K. von Bergmann, P. Ferriani, S. Heinze, G. Bihlmayer, A. Kubetzka, O. Pietzsch, S. Blügel, and R. Wiesendanger, Chiral magnetic order at surfaces driven by inversion asymmetry, Nature **447**, 190–193 (2007).

[12] B. Zimmermann, Calculation of the Dzyaloshinskii-Moriya Interaction in ultrathin magnetic Films: Cr/W(110), Master's thesis, RWTH Aachen, 2010.

[13] P. Hohenberg and W. Kohn, Inhomogeneous Electron Gas, Phys. Rev. **136**(3B), B864–B871 (Nov 1964).

[14] W. Kohn and L. J. Sham, Self-Consistent Equations Including Exchange and Correlation Effects, Phys. Rev. **140**(4A), A1133–A1138 (Nov 1965).

[15] M. J. Mehl and D. A. Papaconstantopoulos, Applications of a tight-binding total-energy method for transition and noble metals: Elastic constants, vacancies, and surfaces of monatomic metals, Phys. Rev. B **54**(7), 4519–4530 (Aug 1996).

[16] `http://cst-www.nrl.navy.mil/.`

[17] D. A. Papaconstantopoulos and M. J. Mehl, Tight-Binding Method in Electronic Structure, in *Encyclopedia of Condensed Matter Physics*, edited by G. Bassani, G. Liedl, and P. Wyder, volume 1, pages 194–206, Academic Press, 2005.

[18] D. A. Papaconstantopoulos and M. J. Mehl, The Slater–Koster tight-binding method: a computationally efficient and accurate approach, Journal of Physics: Condensed Matter **15**(10), R413 (2003).

[19] E. C. Stoner, Collective Electron Specific Heat and Spin Paramagnetism in Metals, Proc. R. Soc. London Series A **154**(656) (1936).

[20] E. C. Stoner, Collective Electron Ferromagnetism, Proc. R. Soc. London Series A **165**, 372–414 (1938).

[21] C. Herring, Exchange interactions among itinerant electrons, Academic Press, 1966.

[22] L. M. Sandratskii, Energy Band Structure Calculations for Crystals with Spiral Magnetic Structure, phys. stat. sol. (b) **136**(167) (1986).

[23] L. M. Sandratskii, Symmetry analysis of electronic states for crystals with spiral magnetic order. I. General properties, Journal of Physics: Condensed Matter **3**(44), 8565 (1991).

[24] M. Heide, G. Bihlmayer, and S. Blügel, Describing Dzyaloshinskii-Moriya spirals from first principles, Physica B: Condensed Matter **404**(18), 2678 – 2683 (2009), Proceedings of the Workshop.

[25] G. Autès, C. Barreteau, D. Spanjaard, and M.-C. Desjonquères, Magnetism of iron: from the bulk to the monatomic wire, Journal of Physics: Condensed Matter **18**(29), 6785 (2006).

[26] G. Autès, *Transport électronique polarisé en spin dans les contacts atomiques de fer*, PhD thesis, Universite Pierre et Marie Curie - Paris VI, 2008.

[27] S. Baud, C. Ramseyer, G. Bihlmayer, S. Blügel, C. Barreteau, M. C. Desjonquères, D. Spanjaard, and N. Bernstein, Comparative study of ab initio and tight-binding electronic structure calculations applied to platinum surfaces, Phys. Rev. B **70**(23), 235423 (Dec 2004).

[28] J. C. Slater and G. F. Koster, Simplified LCAO Method for the Periodic Potential Problem, Phys. Rev. **94**(6), 1498–1524 (Jun 1954).

[29] W. A. Harrison, *Electronic Structure and the Properties of Solids*, Dover, 1989.

[30] P. B. Allen, J. Q. Broughton, and A. K. McMahan, Transferable nonorthogonal tight-binding parameters for silicon, Phys. Rev. B **34**(2), 859–862 (Jul 1986).

[31] F. Liu, M. R. Press, S. N. Khanna, and P. Jena, Magnetism and local order: Ab initio tight-binding theory, Phys. Rev. B **39**(10), 6914–6924 (Apr 1989).

[32] C. Barreteau, D. Spanjaard, and M. C. Desjonquères, Electronic structure and total energy of transition metals from an *spd* tight-binding method: Application to surfaces and clusters of Rh, Phys. Rev. B **58**(15), 9721–9731 (Oct 1998).

[33] W. A. Harrison, *Elementary Electronic Structure*, World Scientific, 1999.

[34] C. Barreteau, private communication, 2009.

[35] F. Ercolessi, Lecture notes on Tight-Binding Molecular Dynamics, and Tight-Binding justification of classical potentials, (2005).

[36] C. G. Broyden, A Class of Methods for Solving Nonlinear Simultaneous Equations, Mathematics of Computation **19**(92), 577–593 (1965).

[37] S. Shallcross, L. Nordström, and S. Sharma, Magnetic phase diagrams from non-collinear canonical band theory, Phys. Rev. B **76**(5), 054444 (Aug 2007).

[38] E. I. Rashba, Properties of semiconductors with an extremum loop, Sov. Phys. Solid State **2**(1109) (1960).

[39] W. Nolting, *Grundkurs Theoretische Physik 5/2: Quantenmechanik - Methoden und Anwendungen*, Springer-Verlag Berlin, 2004.

[40] B. Hardrat, A. Al-Zubi, P. Ferriani, S. Blügel, G. Bihlmayer, and S. Heinze, Complex magnetism of iron monolayers on hexagonal transition metal surfaces from first principles, Phys. Rev. B **79**(9), 094411 (Mar 2009).

[41] K. Nakamura, T. Akiyama, I. Tomonori, and A. J. Freeman, Spin-spiral structures in free-standing Fe(110) monolayers, Journal of Applied Physics **99**(08N501) (2006).

[42] L. D. Landau and E. M. Lifschitz, *Lehrbuch der theoretischen Physik Band III - Quantenmechanik*, Akademie Verlag Berlin, 1979.

[43] R. Gebauer, *Nouvelles méthodes pour le calcul ab-initio des propriétés statiques et dynamiques des matériaux magnétiques*, PhD thesis, ENS Lyon, 1999.

[44] A. R. Mackintosh and O. K. Andersen, The electronic structure of transition metals, Cambridge Univ. Press, 1980.

[45] A. Oswald, R. Zeller, P. J. Braspenning, and P. H. Dederichs, Interaction of magnetic impurities in Cu and Ag, J. Phys. F.: Met. Phys. **15**(193) (1985).

[46] A. I. Liechtenstein, M. I. Katsnelson, V. P. Antropov, and V. A. Gubanov, Local spin density functional approach to the theory of exchange interactions in ferromagnetic metals and alloys, Journal of Magnetism and Magnetic Materials **67**(1), 65 – 74 (1987).

[47] A. Crépieux and C. Lacroix, Dzyaloshinsky-Moriya interactions induced by symmetry breaking at a surface, Journal of Magnetism and Magnetic Materials **182**(3), 341 – 349 (1998).

[48] I. E. Dzyaloshinskii, Theory of helicoidal structures in antiferromagnets. III., Sov. Phys. JETP **20**(665) (1965).

[49] Y. A. Izyumov, Modulated, or long-periodic, magnetic structures of crystals, Sov. Phys. Usp. **27**(845) (1984).

[50] A. Sommerfeld and H. Bethe, *Handbuch der Physik*, Springer, 1933.

[51] J. C. Slater, Atomic Shielding Constants, Phys. Rev. **36**(1), 57–64 (Jul 1930).

[52] R. Bozarth, *Ferromagnetism*, Van Nostrand, 1951.

[53] Y. Mokrousov, G. Bihlmayer, S. Blügel, and S. Heinze, Magnetic order and exchange interactions in monoatomic 3*d* transition-metal chains, Phys. Rev. B **75**(10), 104413 (Mar 2007).

[54] N. C. Bacalis, D. A. Papaconstantopoulos, M. J. Mehl, and M. Lach-hab, Transferable tight-binding parameters for ferromagnetic and paramagnetic iron, Physica B: Condensed Matter **296**(1-3), 125 – 128 (2001).

[55] `http://www.fplo.de`.

[56] `http://www.flapw.de`.

[57] F. Schubert, First Principle study of non-collinear magnetism in monatomic transition metal-chains, Master's thesis, Universität Hamburg, 2009.

[58] O. Gunnarsson, Band model for magnetism of transition metals in the spin-density-functional formalism, Journal of Physics F: Metal Physics **6**(4), 587 (1976).

[59] J. F. Janak, Uniform susceptibilities of metallic elements, Phys. Rev. B **16**(1), 255–262 (Jul 1977).

[60] T. Oda and A. Hosokawa, Fully relativistic two-component-spinor approach in the ultrasoft-pseudopotential plane-wave method, Phys. Rev. B **72**, 224428 (2005).

[61] P. Ravindran, A. Kjekshus, H. Fjellvåg, P. James, L. Nordström, B. Johansson, and O. Eriksson, Large magnetocrystalline anisotropy in bilayer transition metal phases from first-principles full-potential calculations, Phys. Rev. B **63**, 144409 (2001).

[62] T. Burkert, O. Eriksson, S. I. Simak, A. V. Ruban, B. Sanyal, L. Nordström, and J. M. Wills, Magnetic anisotropy of $L1_0$ FePt and $Fe_{1-x}Mn_xPt$, Phys. Rev. B **71**, 134411 (2005).

[63] M. Tsujikawa, A. Hosokawa, and T. Oda, Magnetic anisotropy of Fe/Pt(001) and Pt/Fe/Pt(001) using a first-principles approach, Phys. Rev. B **77**, 054413 (2008).

[64] A. Menshikov, V. Antropov, G. Gasnikova, Y. Dorofeyev, and V. Kazantsev, Magnetic phase diagram of ordered $(Fe_{1-x}Mn_x)Pt$ alloys, Journal of Magnetism and Magnetic Materials **65**(1), 159 – 166 (1987).

[65] J. Lyubina, I. Opahle, K.-H. Müller, O. Gutfleisch, M. Richter, M. Wolf, and L. Schultz, Magnetocrystalline anisotropy in $L1_0$ FePt and exchange coupling in FePt/Fe 3 Pt nanocomposites, Journal of Physics: Condensed Matter **17**(26), 4157 (2005).

[66] S. Blügel, Magnetische Anisotropie und Magnetostriktion, in *Vorlesungsmanuskript zur 30sten Ferienschule 1999: Magnetische Schichtsysteme*, Schriften des Forschungszentrums Jülich Reihe Schlüsseltechnologien, 1999.

[67] T. Moriya, Ferro- and antiferromagnetism of transition metals and alloys, Solid State Communications **2**(8), 239 – 243 (1964).

[68] G. Lehmann and M. Taut, On the Numerical Calculation of the Density of States and Related Properties, Physica Status Solidi (b) **54**(2), 469 – 477 (1972).

List of Figures

Danksagung

Ich bin einigen Personen zu Dank verpflichtet, die ihren Teil zu dieser Arbeit beigetragen haben.

Zuerst einmal möchte ich mich bei Prof. Stefan Blügel bedanken, der es mir ermöglicht hat an seinem Institut diese Arbeit anzufertigen. Die ausführlichen Gespräche mit ihm waren sehr interessant und gaben Raum für neue Ideen. Besonders danke ich ihm auch dafür, dass er mir zu den Auslandsaufenthalten in Paris verholfen hat.

Ich danke ebenfalls Prof. Riccardo Mazzarello der freundlicherweise das Zweitgutachten der Arbeit übernehmen wird.

Zu grossem Dank bin ich Prof. Cyrille Barreteau verpflichtet, der mich während meiner Zeit im CEA Saclay hervorragend betreut hat. Die ausführlichen Diskussionen mit ihm haben mir sehr geholfen und der ein oder andere Fehler im Code wäre wohl ohne seine Vergleichsrechnungen unentdeckt geblieben.

Ganz besonders möchte ich mich bei Dr. Phivos Mavropoulos und Dr. Yuriy Mokrousov bedanken, die mir bei Fragen immer mit Rat und Tat zur Seite standen. Die unzähligen Diskussionen mit ihnen haben die Richtung meiner Arbeit maßgeblich geprägt.

Insbesondere bedanke ich mich bei David Bauer, Benedikt Schweflinghaus, Bernd Zimmermann und Alexander Thiess für ihren fachlichen Rat und ihre Hilfe, aber auch für die lustigen und interessanten Gespräche abseits der Physik. Bedanken möchte ich mich ebenfalls bei Dr. Hongbin Zhang, der mir freundlicherweise einige *ab-initio* Resultate zur Verfügung gestellt hat. Vielen Dank auch an Dr. Tobias Burnus, der mir immer unmittelbar bei Problemen mit UNIX zur Seite stand. Ich danke ebenfalls allen anderen Mitgliedern des IFF1, die zu einer angenehmen Atmosphäre beigetragen haben.

Von ganzem Herzen bedanke ich mich bei meinen Eltern und meiner Freundin Christa. Sie waren mir in der gesamten Zeit die grösste seelische Unterstützung die man sich vorstellen kann.

Selbständigkeitserklärung

Hiermit versichere ich, die vorliegende Arbeit selbständig und nur unter Zuhilfenahme der angegebenen Quellen und Hilfsmittel angefertigt zu haben.

Timo Schena
Jülich, den 20. Dezember 2010